First-principles investigations of structure–function relationships in bismuth ferrite

John Kane Shenton

A dissertation submitted for the degree of

Doctor of Philosophy

Physics & Astronomy
University College London.

July 2018

Declaration

I, John Kane Shenton, confirm that the work presented in this thesis is my own. Where information has been derived from other sources, I confirm that this has been indicated in the thesis.

Abstract

The simplicity of the basic perovskite structure belies a seemingly boundless potential for novel phenomena and technological applications. The ferroelectric perovskites, in particular, can have complex and subtle relationships between their crystal structures and functional properties. In this work, advanced computational approaches are used to gain insight into key structure–function relationships in the multiferroic perovskite, bismuth ferrite (BFO).

Density functional theory (DFT) has proven to be an immensely valuable tool in the study of condensed matter. However, techniques beyond standard DFT are often required to deal with the strongly localised electronic states in materials like BFO. In the first part of this thesis, we conduct a systematic study of a commonly used correction to DFT: DFT+U. We focus on the effect of the U parameter on the conduction band minimum (CBM) and valence band maximum (VBM). We find drastic changes to the location and curvature of the CBM in particular. Specifically, we find a surprising inversion in the ordering of the Fe t_{2g} and e_g manifolds at the CBM when U exceeds 4 eV. We therefore suggest caution when employing large values of U to calculate optoelectronic properties.

In the second part of this work, motivated by the prospects of BFO-based photovoltaics, we investigate the influence of crystal structure on charge carrier effective masses. We begin by comparing the effective masses of several known phases of BFO, finding orders of magnitude differences between them. The strain-induced tetragonal phase emerged from this comparison as having the promising combination of a large spontaneous polarisation and relatively light charge carriers. Through a systematic decomposition of geometric relationships between different phases of BFO, we identify key physical influences on effective masses. We suggest that these insights could be exploited to improve photovoltaic efficiency.

In the final part of this thesis, we enter the realm of designer materials. The creation and characterisation of atomically sharp interfaces between different complex oxides has proven to be an exciting and fruitful area of research in recent years. We investigate superlattices made up of repeating lanthanum aluminate (LAO) and BFO layers. By simply varying the thickness of the BFO layer, we found that one could tune the tetragonality, spontaneous polarisation and band gap of the superlattices. We also predict the formation of two-dimensional (2D) electron and hole gases at opposing interfaces above a critical thickness of BFO. The ferroelectric origin of the 2D gases, together with an emergent magnetism, suggests that this system may be a promising source of novel multiferroic functionality. In particular, we suggest the possibility of switching the 2D electron and hole gases via an external electric field.

Impact statement

The work presented in this thesis is an attempt to gain an understanding of the fundamental mechanisms by which certain materials acquire their unique properties. In particular, we have focussed on a class of materials, the ferroelectric perovskites, that has had a large impact on a number of technologies from sonar to information storage. Novel applications of these fascinating materials are continually being developed. One particularly promising application is in the area of renewable energy.

In part of this thesis, we investigated the nature of a particular perovskite, bismuth ferrite, using atomistic simulations. We discovered a set of atomistic design principles that might be used to improve the efficiency of photovoltaic devices. We also conducted a careful characterisation of a commonly used method for simulating perovskites. The findings from that study will hopefully inform future theoretical work, ensuring more accurate predictions based on such simulations.

Finally, we modelled a new type of hybrid crystal that is composed of two different perovskites. We discovered that one could, in principle, tune various important properties of this material by simply varying the relative thickness of the components. Above some critical thickness, a new state emerges that could have exciting technological applications in, for example, information storage.

While we are motivated and excited by the technological promise of some of these materials and discoveries, we note that at this early stage of research, the scope for direct impact is limited. A great deal of further work will be needed in order to realise this promise.

Acknowledgements

From lively London to sunny Singapore and back again, this PhD has been quite the journey. Along the way, I've been lucky enough to meet and work with some wonderful people. First and foremost among these, are my supervisors, David Bowler and Wei Li Cheah. Dave's wise guidance, knowledge of all things atomistic, and unrivalled patience have been truly invaluable. During my two years in Singapore, I gained so much from Wei Li's insightful questions and benefitted greatly from her expertise in the field of ferroelectric perovskites.

Throughout my time at UCL, I have been extremely fortunate to have had some outstanding office mates and made some fantastic friends. Georg, Kostas, Martin, Callum, Jack B, Jack P, Shereif and Surani – thank you all for the endless laughter and interesting (sometimes scientific) discussions.

A very special thanks is owed to my family for their love and support, and for their consistent confidence in me. And especially to Yasmine, with whom I've shared long and wonderful hours (often via shaky internet connections) laughing, and without whom I would not have finished this thesis.

Finally, I would like to thank the EPSRC and A*STAR for funding this PhD, and would also like to thank the London Centre for Nanotechnology and UCL for providing access to their high-performance computing resources, without which much of this work would not have been possible.

To Yasmine

Contents

List of Figures

List of Tables

1 Introduction

One of the most pressing challenges we face as a society is that of generating sufficient clean energy to meet our ever-growing demands. While it is likely that no single approach will meet all of our needs, the conversion of sunlight directly into electrical energy, as in a photovoltaic (PV) device, is particularly appealing. These work by separating electron–hole pairs that are generated upon the absorption of incoming photons. The separation of charges generates a potential difference that can then be used to do work in a circuit. They, therefore, typically have just one inefficient step between the desired electrical energy and the incoming sunlight, in contrast to other sources of energy such as wind, hydroelectric, gas etc.

The global PV capacity has been increasing rapidly in recent years. In 2017, for example, almost 100 GW of additional capacity was installed globally, bringing total cumulative capacity to about 400 GW [1]. While the rate of increase of capacity is certainly impressive, this still represents just 2% of global electricity generation capacity. In order to replace fossil fuels and meet future energy demands, we need to overcome a number of challenges, some of which are social in nature and some of which are purely technological. Social challenges include implementing suitable financing schemes for home installations and removing existing subsidies for fossil fuels. Some of our major technological challenges include: (i) adapting our electrical grids to suit the more distributed nature of PV power, (ii) developing better batteries to store the energy for use at night or on cloudy days and, of course, (iii) developing better PV devices. We can take "better PV devices" to mean: cheaper to manufacture, more durable, more efficient, or (preferably) all of the above. It is the challenge of developing more efficient PV devices that motivates much of my work.

Designing or discovering better materials is a very broad problem and is certainly not limited to the case of PV devices. Many of the world's grand challenges require materials whose capabilities far exceed those of which we have today. From combating climate change to fighting diseases, we need new and improved materials. Even though our desire for better materials is itself nothing new, modern approaches to materials discovery can appear very different from those of the past. There are, however, some common basic strategies.

We begin by briefly noting that, occasionally, important materials are discovered entirely serendipitously. Fleming's discovery of penicillin is a famous case of a material being discovered almost completely by accident. The structure of the benzene molecule

supposedly came to August Kekulé in a daydream about an ouroboros[1] [2]. While this approach makes for good anecdotes, it is extremely difficult to engineer from the outset.

Perhaps the most straightforward approach that one could pursue is simply: trial and error. This approach has been extremely successful in the past, though it can be costly and time-consuming. Trial and error is often made much more efficient if it is conducted by someone with a well-developed chemical or physical intuition. The tacit knowledge gained through extensive experience with a variety of materials is almost always of enormous benefit to the discovery process. However, since intuition is acquired through experiencing *existing* materials, truly novel materials necessarily involve at least some counterintuitive aspects. For example, in a recent study, Zubko *et al.* demonstrate that certain ferroelectric-dielectric superlattices can exhibit negative capacitance [3]. A balance must therefore be struck between the benefits of fitting a mental model to existing materials and the potential limitations associated with only taking these into account. An analogous balance exists in efforts to use machine learning for materials discovery. Here the balance between over- and under-fitting the model is key [4].

Recent theoretical developments and advances in computing power have allowed us to perform much of the trial and error through virtual, rather than actual, experiments. High-throughput computational screening (see e.g. Ref.5 for a review of these methods) and crystal structure prediction [6], for example, have proven extremely valuable this regard. One striking example is the discovery that, as a catalyst in the hydrogen evolution reaction, a certain BiPt alloy has even better activity than that of pure Pt [7]. This discovery was based on virtual experiments involving over 700 binary surface alloys—something that would be unfeasible in real experiments. In addition to suggesting specific materials, high-throughput computational approaches can be used to identify general heuristics for designing new materials. For example, such approaches have been helpful in elucidating the influence of chemistry on electron and hole effective masses in a broad range of oxides [8, 9].

The most satisfying approach to materials discovery, from my point of view, is to develop a complete understanding of the origins of various properties in a given material, and to thereby be able to design a new one from 'the ground up'. In this thesis, we attempt to gain such an understanding of the fundamental mechanisms that govern important functional properties of some fascinating materials. This we do with the ultimate aim of being able to suggest mechanisms by which we can improve the PV prospects of these materials.

Let us begin with what sort of characteristics one should expect in a good PV material. The first step in a PV process is the absorption an incident photon. For this to occur efficiently, we require that the material have a band gap in a certain energy range (usually around 1.4 eV) and that the absorbing layer be thick enough to actually interact with the incident photons. The absorption of a photon excites an electron–hole pair that need to then be separated. For this charge separation to occur, some source of

[1] An ancient Egyptian symbol of a snake eating its own tail.

asymmetry in the material is required. Finally, the separated electrons and holes need to be transported to their respective electrodes. This necessitates good electron and hole transport characteristics in the PV material. Finally, some of the characteristics that make for a good PV material are independent from considerations of the efficiency of the material. These include the: easy-of-manufacture, cost, earth-abundance, stability and toxicity of the component materials.

Returning to the question of efficient charge separation, in traditional PVs, the required asymmetry is provided by the potential due to a p–n junction. Some materials, however, have an *intrinsic* asymmetry in their crystal structure[2] that allows for the development of a switchable spontaneous electric polarisation[3]; these are known as ferroelectrics. We shall introduce ferroelectrics and the physics that govern them in more detail in Chapter 2, but for now we simply note that their spontaneous polarisation is thought to facilitate charge separation [10], making them promising PV candidates. In addition, these materials typically form ferroelectric domain structures that further aid in charge separation and transport [11, 12]. Despite their excellent charge separation capacity however, ferroelectrics often suffer from relatively low charge carrier mobilities. This limits the efficiency of a ferroelectric PV device since slower charge carriers are less likely to reach their respective electrodes (where they can be made to do work) before recombining. A central theme of this work will therefore be to discover ways of increasing charge carrier mobility without diminishing the bulk polarisation that is so key to enhancing charge separation.

Of all the known ferroelectric materials, the group that has been studied the most is almost certainly the ferroelectric perovskites. Perovskites (chemical formula: ABX_3) have a very simple crystal structure that belies a surprising degree of structural flexibility[4] and subtlety. This simple yet flexible structure lends itself to both fundamental research and a wide range of technological applications.

In this thesis, we focus on a particular perovskite that combines ferroelectricity with magnetism: bismuth ferrite ($BiFeO_3$; BFO). BFO has been widely studied as perhaps the only single phase room-temperature magnetoelectric multiferroic material. The magnetic control of spontaneous polarisation and its converse—the electric field control of magnetism—present the possibility of novel applications, from sensors to information storage [13].

BFO was also the centre of a renaissance[5] in the field of ferroelectric PVs, beginning with the discovery of the switchable diode and bulk photovoltaic effects in 2009 [16]. Subsequent studies revealed the importance of ferroelectric domains in the context of BFO-based PV devices. For example, above band gap photovoltages[6] *across* [11] and

[2] i.e. their crystal structure is non-centrosymmetric.

[3] Note that not all non-centrosymmetric crystals develop a switchable spontaneous polarisation.

[4] In this context I take 'structural flexibility' to indicate a large number of quasi-stable polymorphs, rather than a small elastic constant.

[5] The seminal work of Fridkin [14] suggested the possibility of photoferroics in 1979, though the earliest reported photocurrent in a ferroelectric perovskite ($BaTiO_3$) goes back to 1956 [15].

[6] Above band-gap photovoltages are forbidden in traditional single p-n junction PVs according to Shockley and Queisser. [17]

conduction *along* [12] the domain boundaries have been found experimentally. Efficient charge separation and earth-abundant, non-toxic components are factors that make BFO an appealing candidate PV material. However, BFO scores slightly lower in terms of the other factors in our 'PV wishlist'. While BFO has a relatively low band gap compared to other ferroelectric perovskites (around 2.5 eV), it is significantly larger than the ideal band gap for a PV material (around 1.4 eV). Reducing the band gap, together with understanding and improving the transport characteristics of BFO will therefore be important in order to realise an efficient BFO-based PV device.

While BFO has been widely studied in the context of ferroelectric PVs, as well as for a myriad of other applications, open questions remain as to the fundamental mechanisms behind some of its intriguing functional properties. We know that natures of the conduction band minimum (CBM) and valence band maximum (VBM) typically play important roles in determining the optoelectronic properties of a semiconductor. In particular, the curvature and character at the CBM and VBM are related to the mobilities of the electron and hole, respectively. The relative location of these points in reciprocal space affects the absorption probability of an incident photon. One of the questions that naturally arises is, therefore: in the case of BFO, which factors play an important role in determining the natures of the CBM and VBM? Further, can we employ this understanding to optimise the optoelectronic properties of BFO?

So how does one go about a) determining the natures of the CBM and VBM and b) discovering the mechanism that governs these? Direct information about the location and curvature of the VBM can be obtained via state-of-the-art soft x-ray angle-resolved photoemission spectroscopy (SX-ARPES) experiments. Even with SX-ARPES, however, gaining an understanding of the underlying mechanisms that determine such properties would be extremely challenging. For example, surface reconstructions and defects would strongly affect the obtained spectra due to the inherently complex coupling between crystal and electronic structures that occurs in all ferroelectric materials. That is, it is difficult to disentangle the various structural factors that influence the character, curvature and locations of the CBM and VBM in such materials. Difficulties in growing defect-free, single-phase BFO films can further hinder progress towards an understanding of the fundamental mechanisms [18]. Furthermore, it can be challenging to isolate the effects of interfaces between BFO films and the materials on which those films are grown. Indeed, so strong are interface effects in such complex oxides, that they are studied in their own right, with a wide range of applications in mind; see for example the review by Zubko *et al.* [19].

The fundamental and strong coupling between crystal and electronic structures that underpins many of the experimental challenges also exacerbates important difficulties facing a *theoretical* investigation of BFO. Below, we shall discuss in what manner these theoretical challenges manifest themselves, and the approaches that have been developed to overcome them. Before that, we introduce theoretical approaches to condensed matter more generally.

Theoretical approaches to condensed matter can roughly be said to lie on a spectrum

between empirical and fully *ab initio* methods. At the former extreme, one attempts to construct a model of a given phenomenon by using, for example, symmetry arguments, or by borrowing the mathematical framework that has been successful in describing similar phenomena. One then fits the parameters of the constructed model to known experimental results. Because they can be constructed with terms that relate directly to specific observable properties or symmetries, empirical approaches can often offer a certain 'transparency'. That is, such approaches often have terms that correspond directly to observables and so physical insight is readily available. In addition, they can often allow us to rapidly predict the properties of large systems; i.e. they usually have a relatively low computational cost. Despite the transparency and speed of many empirical models, these often suffer from limited accuracy. Furthermore, because they are finely tuned to a specific type of interaction in a given system, they often lack transferability and predictive power. The lack of transferability becomes particularly problematic when we wish to make predictions about materials whose underlying physics/chemistry lie beyond our current understanding.

In the first-principles approach, by contrast, we make predictions of a phenomenon by building up a system from the ground up, without using any experimental input.[7] Typically we build a system up, starting with a certain configuration of atoms, and employ the basic laws of quantum mechanics (QM) to make predictions about their properties. First-principles methods, and in particular *Density Functional Theory* (DFT), have been very successful at explaining the origin of a number of properties of BFO. In addition to explaining the origin of known properties, DFT has also been used to successfully resolve disagreements in existing experimental literature. For example, it was used in conjunction with the modern theory of polarisation (MTP) to calculate the spontaneous polarisation of BFO. This resolved experimental disagreements as well as suggesting reasons for why they arose in the first place [20].

Despite these theoretical successes, the subtle interplay between structural and electronic degrees of freedom that underlies the tunability of the BFO system make this material particularly challenging to model. For example, the observed weak (Dzyaloshinskii-Moriya) ferromagnetism—due to a slight canting of the otherwise antiferromagnetically ordered spins—cannot be captured without including the effects of spin-orbit coupling (SOC) [21].

More generally, standard DFT methods are known to have systematic failures in describing the electronic structure of materials with strongly correlated d states, such as those of Fe in BFO. In particular, standard local density and generalised gradient approximations of the exchange-correlation (xc) functional incorrectly describe the on-site Coulomb interactions of highly localised electrons, due to erroneous electron self-interaction. This failure to describe strongly localised states exacerbates the infamous band gap problem in DFT.

In Chapter 4, we carefully assess a correction to DFT (DFT+U) that is commonly

[7] In principle even the crystal structure can be predicted from first-principles (e.g. using the approaches reviewed in Ref.6), though in practice this is very often informed by experiments.

used for studying complex oxides such as BFO. We find a surprising inversion of the expected t_{2g}/e_g ordering of the Fe d orbitals at the CBM of BFO when the magnitude of the correction exceeds a certain threshold. This inversion has a large impact on the predicted optoelectronic properties of the material. We thus suggest caution when employing large values of the '+U' correction. More generally, we emphasise the need for careful testing of the effects of U on the electronic structure as a whole, and not simply its effects on band gaps.

In Chapter 5, having characterised our method of interest, we then develop an understanding of the structural factors that determine the charge carrier effective masses in BFO. The approach we take is to first calculate the effective masses of some known BFO phases. We then decompose the various transformations that map the phase with the lightest charge carriers to that with the heaviest. By systematically evaluating the effective masses along these transformation maps, we gain insight into the structural factors that play a key role in determining band curvature and character. We suggest that the physical insight gained in these systematic studies could be harnessed to improve the photovoltaic prospects of BFO. In particular, we suggest that a tetragonal (T) phase of BFO would have the appealing combination of large spontaneous polarisation and light charge carriers.

One way to obtain the T or a T-like phase in BFO is by growing it under compressive epitaxial strain. Lanthanum aluminate ($LaAlO_3$; LAO) was identified as a particularly good substrate for this purpose, as found in a number of experimental studies, reviewed in Ref.22. Bulk LAO has a very similar rhombohedral crystal structure to that of bulk BFO, though it lacks the A-site translation along the pseudo-cubic [111] direction that breaks inversion symmetry in the latter.

In such complex oxide heterostructures, in addition to changing the relative stability of competing phases, the interfaces themselves can have emergent functional properties that go beyond those of either component oxide. Perhaps the most well-known example of an emergent phenomenon is the formation of a two-dimensional electron gas (2DEG) at certain LAO/STO[8] interfaces [23]. This 2DEG has been extensively investigated in subsequent years, with many interesting properties emerging. Superconductivity (even though both component materials have a non-zero band gap [24]) and magnetism (even though both components are non-magnetic) [25], for example, have both been observed at this interface.

In Chapter 6, we model LAO/BFO heterostructures with a focus on a) stabilising a T' phase of BFO and b) looking for emergent interfacial properties. The approach we take is to build superlattices made up of alternating LAO and BFO repeating units. We find that, by manipulating the relative thicknesses of the two component materials, we can (i) tune the spontaneous polarisation, (ii) tune the electronic band gap and (iii) develop potentially switchable 2D free carrier gases at the interfaces between LAO and BFO. The experimental realisation of such 2D gases would likely have a range of useful

[8]Strontium titanate ($SrTiO_3$; STO) is a quantum paraelectric perovskite with the space group: $Pm\bar{3}m$ at room temperature and space group $I4/mcm$ at low temperature.

technological applications.

Having introduced the context and central aims of this thesis, let us further develop the theoretical framework that underpins the work. In the following chapter we briefly introduce the physics of ferroelectrics and then in Chapter 3 we outline the computational methodology, with a focus on those aspects of particular relevance to this thesis.

2 | A brief overview of the physics of ferroelectrics

Ferroelectric materials, and the physics and chemistry that govern them, are extremely subtle and complex. One cannot hope to do justice to the subject in a single chapter. Instead, the aim of this chapter is merely to provide a little context for the later results chapters by way of a short introduction to the main relevant concepts. We begin with a brief overview of historical developments in the field. We then define ferroelectrics formally and outline a key mechanism underlying ferroelectricity in the class of materials of interest to us. We end this chapter with a summary of the modern theory of polarisation, which we employ throughout the thesis to calculate bulk polarisation.

2.1 A brief history of ferroelectricity

The history of our understanding of ferroelectrics is a rich and complex one, spanning decades and involving several dead-ends and false starts. We summarise it here in order to provide some context for our current understanding of the physics of ferroelectrics. For more on the history of ferroelectricity, and indeed a far more in-depth discussion of the actual physics involved, we refer the reader to the 1977 classic text by Lines and Glass [26] as well as the more recent book edited by Rabe, Ahn and Triscone [27]. Many of the seminal texts in this field are gathered in *Ferroelectricity: The Fundamentals Collection,* edited by Gonzalo and Jiménez [28].

First discovered in Rochelle salt (sodium potassium tartrate tetrahydrate) in 1920 by Valasek [29, 30], ferroelectricity was thought for decades to be exceedingly rare: "one of nature's great accidents" [p.2 26]. The later discovery of ferroelectricity in potassium dihydrogen phosphate (KDP) confirmed to many researchers at the time that the presence of hydrogen bonding was a necessary condition for a material to be ferroelectric. Indeed, one of the early attempts to develop a microscopic model of ferroelectricity was based on possible orientations of the hydrogens in KDP [31].

The view that hydrogen bonding is fundamental to ferroelectricity persisted until 1946 when, in an effort to find a replacement for the widely-used dielectric material, mica, the signature of ferroelectricity was discovered in the perovskite ceramic: barium titanate ($BaTiO_3$; BTO) [32–34]. The simplicity of the perovskite structure (and its conspicuous lack of hydrogen bonding) allowed for large leaps forward in our understanding of ferro-

electricity's microscopic origin. It also allowed for the development of phenomenological models to explain and predict the macroscopic behaviour of ferroelectrics.

In 1960, Cochran made a great leap forward in our understanding of the microscopic origin of ferroelectricity by re-casting the problem in terms of lattice dynamics and introducing the soft mode concept [35].[1] Upon cooling below a critical temperature (referred to as the ferroelectric Curie temperature, T_C), some ferroelectrics are observed to go through a second-order phase transition from a paraelectric (high-symmetry) to a ferroelectric (low-symmetry) state. This can be understood, according to soft mode theory, in terms of the freezing in of a transverse optic phonon mode. That is, there is some unstable phonon mode at high temperature which, upon cooling, becomes softer; i.e. its frequency at a particular point in the Brillouin zone approaches zero. At T_C, the frequency at this point (usually the Γ-point) reaches zero and the distortion is said to be frozen in.

A phenomenological account of ferroelectricity was developed by Devonshire [36–38] soon after the discovery of BTO, based on the earlier work of Landau and Ginzburg; see the chapter by Chandra and Littlewood in Ref.27 for a summary of these. The Landau-Ginzburg-Devonshire approach proved to be extremely successful in describing the behaviour of ferroelectrics around phase transitions. In such models, the free energy of a system is expanded in terms of its macroscopic quantities (polarisation, strain etc.). The terms of this expansion can be obtained through careful consideration of the symmetries of the system. The expansion coefficients can then either be fitted to experimental data or to results from the kinds of first principles simulations we discuss in Chapter 3. The latter approach effectively bridges the microscopic and macroscopic, greatly enhancing the usefulness of such simulations.

Fundamental to any description of ferroelectrics (or indeed any dielectric material) is the concept of macroscopic polarisation. The traditional approach to thinking about and calculating macroscopic polarisation begins with Clausius and Mossotti (CM) in the mid-to-late 1800's [39, 40]. In this picture, one imagines a dielectric to be composed of identifiable polarisable units whose polarisation contribution may be summed over to get that of the bulk. It was not until the early 1990's that an alternative theory was developed. The *Modern Theory of Polarisation* (MTP), discussed at some length in Section 2.4, more closely parallels the pragmatic definition of macroscopic polarisation used by experimentalists. That is, the MTP emphasises *differences* in polarisation as fundamental. In addition to more accurately describing reality, the MTP has proven to be extremely useful for computing bulk polarisation (and related properties) using modern first-principles simulations. In particular, the MTP can be cast in terms of Berry phases and Wannier functions—quantities that can arise naturally in most modern first-principles simulations.

[1] We should note that Ginzburg, in Chapter 4 of Ref.28, disputes that idea that Cochran introduced the soft mode concept, claiming instead that the basic concepts were actually introduced 10 years prior (by Ginzburg).

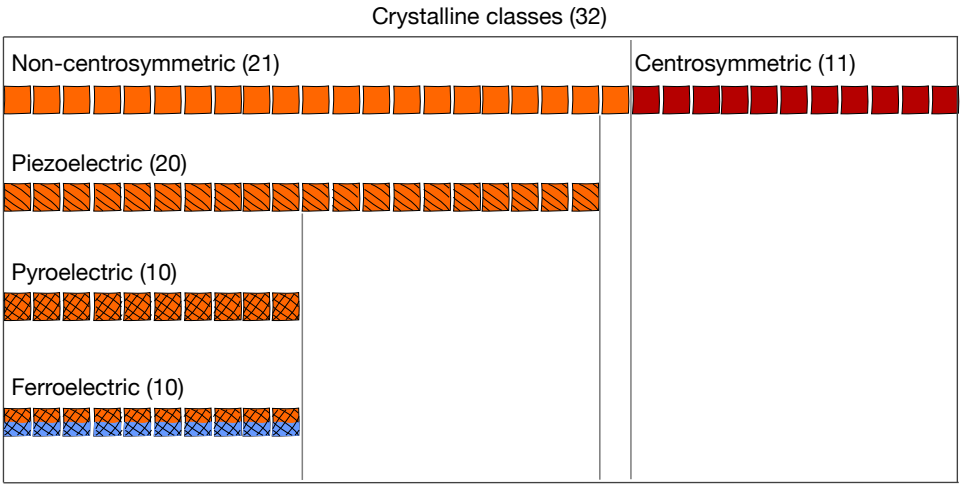

Figure 2.1: Symmetry categorisation of the 32 crystalline classes. The numbers on parentheses refer to the number of crystalline classes in each sub-group. Note that some subset of pyroelectric materials are also ferroelectric, though this is not determined by the crystalline group.

2.2 What exactly are ferroelectrics?

Ferroelectrics are those insulating materials that: (i) have at least two states of spontaneous electric polarisation[2] and (ii) can be switched from one state to another using an applied electric field. From the crystallographic perspective, all ferroelectrics lack a centre of inversion symmetry, i.e. ferroelectrics belong to a subset of the non-centrosymmetric crystalline classes. In fact, ferroelectrics are a subset of pyroelectrics which themselves are a subset of piezoelectrics (which make up the majority of the non-centrosymmetric classes). This relationship is indicated in Fig. 2.1. Note that we cannot say *a priori* if a given pyroelectric material will be ferroelectric solely based on its crystalline class; this is determined by other factors such as local chemistry [41]. In the following section, we present a useful framework for thinking about the origin of ferroelectricity in many materials.

The experimental signature of ferroelectricity is the observation of a polarisation–electric field hysteresis loop such as the one in Fig. 2.2(c). Note that while a perfect dielectric has no hysteresis (Fig.2.2(a)), a lossy dielectric (an infamous example being the skin of a banana [42]) displays some hysteresis that may be mistaken for that of a ferroelectric. Such curves can be measured using a Sawyer-Tower circuit in which the ferroelectric material is connected in series with a reference capacitor. To get the value of the spontaneous polarisation (i.e. the polarisation when no external electric field is applied), you apply a variable voltage across the capacitor and sample and measure the voltage drop across the capacitor. Since they are in series, the charge on the reference capacitor and the ferroelectric sample must be equal. This charge can be calculated using: $Q = CV$, where Q is the charge on the capacitor, V is voltage drop across the

[2] A 'spontaneous electric polarisation' is a non-zero electric polarisation in zero applied field.

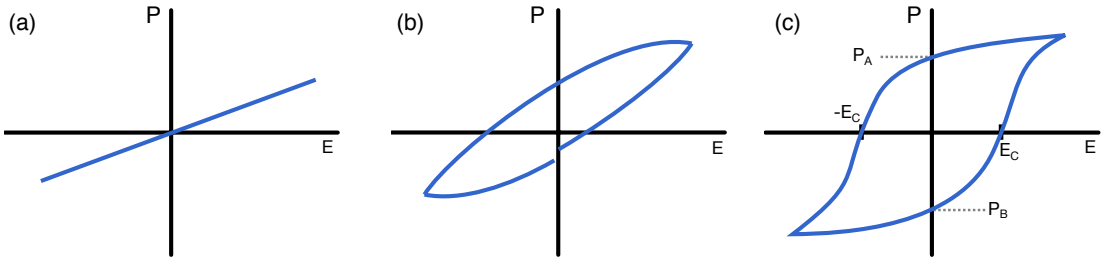

Figure 2.2: Typical polarisation–electric field (P–E) hysteresis loops for (a) perfect dielectric, (b) lossy dielectric and (c) ferroelectric materials. E_c is the coercive field and the spontaneous polarisation in (c) is given by $(P_A - P_B)/2$.

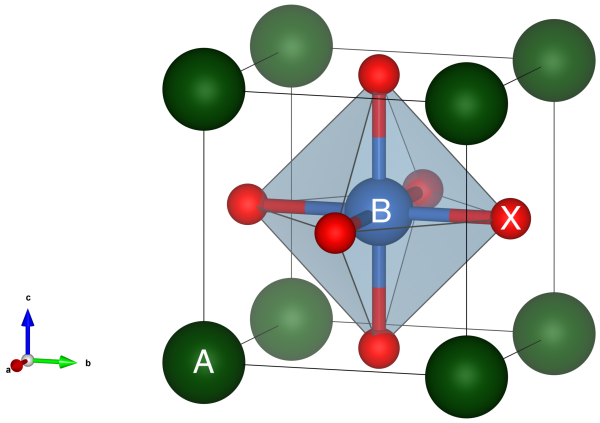

Figure 2.3: Ideal cubic perovskite crystal structure, ABX_3. Notice that the X anions form an octahedral cage around the B-site cation.

capacitor and C is its known capacitance. The polarisation of the sample can then be computed as simply $P = Q/A$, where A its surface area perpendicular to the field. With a sufficiently large applied field (known as the coercive field, E_c), the polarisation of the ferroelectric sample can be switched between its two possible states, P_A and P_B. The *spontaneous* polarisation (P_s) is then taken to be half of the difference between the two polarisation values found at zero applied voltage (i.e. $P_s = (P_A - P_B)/2$).

2.3 The origin of ferroelectricity

The question of what causes ferroelectricity is a complex and subtle one, reflecting the variety of ways in which long- and short-range interactions balance out in any given material. For detailed discussions of the various mechanisms at play, see Refs. [26–28, 43]. In this section we outline a framework for thinking about spontaneous polarisation that is helpful for understanding many known ferroelectric materials. More precisely, we focus on so-called 'proper' ferroelectrics in which the ferroelectric polarisation arises through a lattice instability at the Γ-point.

We begin by observing that is often convenient to think of a ferroelectric phase in terms of a symmetry-lowering distortion from a non-polar phase. Many ferroelectric

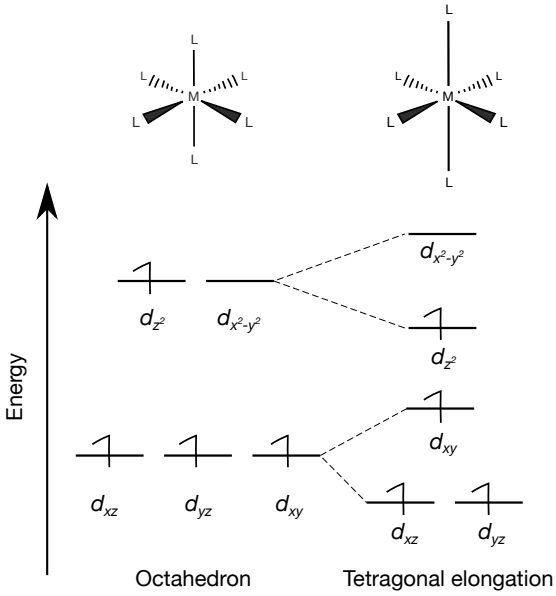

Figure 2.4: Schematic energy levels of an octahedral high-spin d^4 complex showing how a Jahn–Teller distortion would lower the system's total energy.

materials undergo such a symmetry-breaking phase transition as they are cooled below their ferroelectric Curie temperature. The question then arises of why some materials undergo such a transition whilst others do not. We shall focus on the most widely studied, and most relevant to the present work, class of ferroelectrics: the ferroelectric perovskites.

The prototypical centrosymmetric perovskite structure, shown in Fig. 2.3, has the chemical formula: ABX_3 and belongs to the space group: $Pm\bar{3}m$. A shift in the positions of either the A-site or B-site cations relative to the X-site anions results in a non-centrosymmetric structure and a resulting polarisation. In order to understand why symmetry-breaking distortions may happen at all, it is helpful to invoke the ideas of Hermann A. Jahn and Edward Teller , well known to the chemistry community.

Jahn and Teller (JT) explain that, under certain conditions, a molecule or molecular complex may lower its total energy via a geometric distortion if that distortion breaks a degeneracy in the electronic configuration. Such a mechanism is shown schematically in Fig. 2.4 for the case of an octahedral high-spin d^4 complex. In this case we see that the overall system energy may be reduced through the elongation of one octahedral axis.

An analogous mechanism, referred to either as the *pseudo-* or *second-order Jahn–Teller* effect (SOJT), is responsible for symmetry breaking in the case of ferroelectric perovskites. In the second-order Jahn–Teller effect, the total energy of the system is reduced by accessing low-lying *excited* states, rather than by breaking a ground-state electronic degeneracy. To see what we meant by this, we can expand the electronic ground-state energy, E, in terms of a structural perturbation, Q [p.179 27]:

$$E(Q) = E(0) + AQ + BQ^2 + \cdots . \tag{2.1}$$

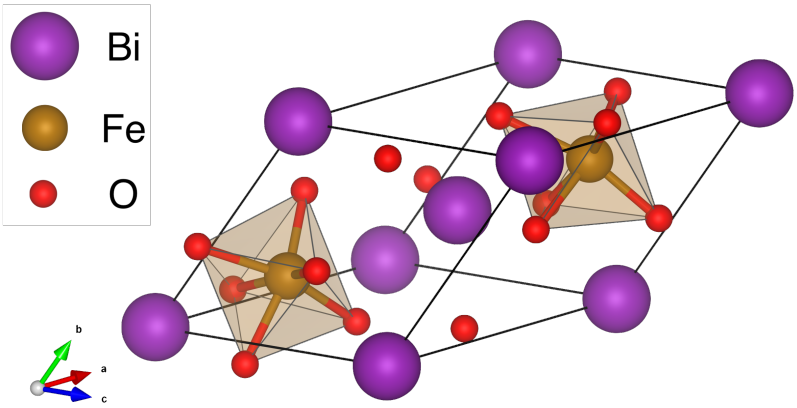

Figure 2.5: Crystal structure of $R3c$ BFO.

Here, $E(0)$ is the energy of the undistorted ground state and AQ and BQ^2 represent the first- and second-order Jahn–Teller effects respectively. The energy associated with the aforementioned first-order JT effect is given by: $AQ = \langle 0|(\delta H/\delta Q)_0|0\rangle\, Q$; notice that this term is only non-zero in the case of degenerate states, as discussed above.

The second-order term can be broken down into two competing contributions:

$$BQ^2 = \frac{1}{2}\left(\langle 0|(\delta^2 H/\delta Q^2)_0|0\rangle - 2\sum_n \frac{|\langle 0|(\delta H/\delta Q)_0|n\rangle|^2}{E_n - E(0)}\right) Q^2, \tag{2.2}$$

where the first of these terms represents the energy associated with distorting the structure without electronic reconstruction. Because there is no electronic reconstruction in this term, neighbouring electron clouds experience a strong Coulomb repulsion as the distortion forces them to overlap. This term is therefore always positive—smaller in the case of closed-shell ions and larger for open-shell ions since the former are less spread out than the latter. The second term represents the mixing of ground and excited states; i.e. new bond formation/hybridisation. The second term has a large magnitude when low-lying states are available such that the denominator, $E_n - E(0)$, is small. The numerator depends on the symmetry representations of the distortion as well as the those of the ground and excited states. Specifically, the matrix element, $\langle 0|(\delta H/\delta Q)_0|n\rangle$, is non-zero if and only if the product of the symmetry representations is itself symmetric. In the case we are discussing here—a non-centrosymmetric distortion from a centrosymmetric ground-state—the matrix element is non-zero if and only if the excited state is non-centrosymmetric.

To make the above discussion a little more concrete, let us consider a specific example (one that is also relevant to later chapters): bismuth ferrite ($BiFeO_3$; BFO). BFO will be introduced in more detail in Chapters 4 and 5, but here we discuss the origin of its spontaneous polarisation. BFO has a rhombohedral, $R3c$, structure as shown in Fig. 2.5. The spontaneous polarisation in BFO arises due to the displacement of the Bi ions along the pseudo-cubic [111] direction. This is driven by the stereochemical activity

of the Bi 6*s* lone pair [20]. In terms of the SOJT effect, a displacement of the Bi ion allows the hybridisation of the lone pair with low-lying p states, thus lowering the total electronic energy of the system [44]. Returning to eqn.2.1, the first term in BQ^2 is small in this case due to the closed-shell nature of the Bi^{3+} ion. The second term meets the symmetry requirements (since the hybridised state is non-centrosymmetric) and is thus non-zero.

It is important to stress that, even when the above conditions are met and a SOJT distortion occurs, this does not guarantee that the material as a whole will exhibit a spontaneous polarisation. Other geometric factors, such as the rotations of the BX_6 octahedra in certain perovskites, may[3] cause the local polarisations to be arranged in an antipolar manner such that they exactly cancel out.

2.4 Calculating bulk polarisation

Having discussed what ferroelectrics are, and why some materials become spontaneously polarised whilst others do not, let us now discuss how one would go about calculating a material's polarisation. We shall see why the traditional view of bulk polarisation as 'the dipole moment per unit volume' is inadequate and what to replace it with.

2.4.1 The Clausius-Mossotti picture

As mentioned above, the first theory of polarisation in condensed matter is due to Clausius and Mossotti (CM) [39, 40]. According to the CM picture, macroscopic polarisation can be viewed as the sum of individual, localised, dipole moments divided by the volume. For a crystal, the dipole moment contributions within a chosen unit cell are summed and then divided by the cell volume.

A necessary condition for this approach to be viable both in principle, and as a practical means to calculate macroscopic polarisation, is that it must be possible to unambiguously partition the electronic charge density into localised contributions. If that were not the case, then the polarisation of the material would be contingent on our choice of 'polarisation unit' and our choice of crystallographic unit cell.

Identifying the polarisation units is possible for an idealised ionic material, however, most real materials have a mixture of various types of bonding. That is to say, the electron density forms a continuous distribution which cannot be unambiguously partitioned. It is important to note the subtlety here: there are, in fact, two separate criticisms of the traditional approaches to polarisation. The first is that, contrary to the CM picture, the distribution of charges is in fact continuous. The second is that, even if we know the charge distribution exactly, we would still not be able to define polarisation because there is no unique way to partition this distribution into polarisation units. To see why this is the case, let us consider possible approaches to such a partitioning.

[3] Even though the rotation and polar modes generally compete with each other, recent work demonstrates that there can be a cooperative coupling between these modes in some cases. [45]

Typically we begin by thinking about crystals, and so an obvious candidate polarisation unit would be the crystal unit cell. In this case the macroscopic polarisation would be given by $\mathbf{P}_{cell}$:

$$\mathbf{P}_{cell} = \frac{1}{V_{cell}} \int_{cell} d\mathbf{r}\, \mathbf{r}\, \rho(\mathbf{r}), \tag{2.3}$$

where V_{cell} is the volume of the unit cell and $\rho(\mathbf{r})$ is the charge density (including both nuclei and electrons). However there is no such thing as *the* unit cell; for a given Bravais lattice, we can define the unit cell in an infinite number of different ways. Since we require the definition of polarisation to be independent of our choice, we may try to average over all possible (translational shifts in) unit cells. Unfortunately such an average will, by symmetry, always return a polarisation value of zero.[4]

An alternative to using the crystal unit cell, is to define the polarisation unit as the entire sample (assuming then of course that the sample is finite) (as in eqn. (2.4)).

$$\mathbf{P}_{samp} = \frac{1}{V_{samp}} \int_{samp} d\mathbf{r}\, \mathbf{r}\, \rho(\mathbf{r}), \tag{2.4}$$

where $\mathbf{P}_{samp}$ is the macroscopic polarisation, V_{samp} is the volume of the sample and $\rho(\mathbf{r})$ is the charge density. While this removes the need for an arbitrary choice of unit cell, in this view the macroscopic polarisation ceases to be a purely bulk property. $\mathbf{P}_{samp}$ will change according to the surface preparation of the sample. Furthermore it is unclear how $\mathbf{P}_{samp}$ relates to changes in the internal charge distribution due to an electric field—the very thing we are trying to describe!

The lesson to be taken away from the above discussion is that knowledge of the periodic electronic charge distribution is, even in principle, not sufficient to define bulk polarisation. Another approach is clearly needed, and for this we turn to the modern theory of polarisation.

2.4.2 The modern theory of polarisation (MTP)

In the early 1990's, faced with the challenges in the CM theory, Resta [46, 47], King-Smith and Vanderbilt [48], developed a modern theory of polarisation. They begin by recognising the pragmatic approach taken by experimentalists—namely, to measure the *change* in polarisation during some process (as in the Sawyer–Tower setup described above).

The modern theory closely parallels this pragmatic approach in that we begin its derivation by considering the change in $\mathbf{P}$ due to an adiabatic change in, for example, an external electric field. We can define $\Delta\mathbf{P}$ as the change in polarisation with respect to some dimensionless parameter representing adiabatic time, λ:

$$\Delta\mathbf{P} = \int_0^1 d\lambda \frac{d\mathbf{P}}{d\lambda}, \tag{2.5}$$

[4] Provided the unit cells are neutral overall.

between an initial ($\lambda = 0$) and a final state ($\lambda = 1$). In the case of spontaneous polarisation, this could be the transition from the centrosymmetric phase to one of the ferroelectric, non-centrosymmetric phases. It should be stressed however that this is a general definition, applying to both spontaneous and induced polarisation.

Now, according to Bloch's theorem, crystalline systems have eigenfunctions of the form $\psi_{n\mathbf{k}}(\mathbf{r}) = e^{i\mathbf{k}\cdot\mathbf{r}}u_{n\mathbf{k}}(\mathbf{r})$, where u are cell-periodic functions.[5] Assuming such eigenfunctions, we can use first order perturbation theory to write the contribution from valence[6] band n as:

$$\frac{d\mathbf{P}_n}{d\lambda} = \frac{ief_n}{(2\pi)^3}\int_{BZ} d\mathbf{k}\,\langle\nabla_{\mathbf{k}}u_{n\mathbf{k}}|\partial_\lambda u_{n\mathbf{k}}\rangle + c.c., \tag{2.6}$$

where f_n is the occupancy of band n ($f = 2$ for spin-degenerate systems) and *c.c.* represents the complex conjugate. The integral is taken over the Brillouin zone (BZ). To arrive at this result we employ an argument made by Thouless *et al.* [49] in order to remove the explicit dependence on the conduction bands (following Ref.48).

Of course, the effective total polarisation has both electronic and ionic contributions:

$$\mathbf{P}_{\text{eff}} = \Delta\mathbf{P}_{\text{ion}} + [\mathbf{P}_{\text{el}}(\lambda = 1) - \mathbf{P}_{\text{el}}(\lambda = 0)], \tag{2.7}$$

where the implicit assumption of path independence holds, provided the system remains insulating at each point along the path ($\lambda = 0 \rightarrow \lambda = 1$). The electronic contribution due to all occupied bands is given by:

$$\mathbf{P}_{\text{el}}(\lambda) = \frac{ef}{(2\pi)^3}\,\text{Im}\sum_n \int_{BZ} d\mathbf{k}\;\langle u_{n\mathbf{k}}|\,\nabla_{\mathbf{k}}\,|u_{n\mathbf{k}}\rangle, \tag{2.8}$$

where $\text{Im}(Z)$ is to take only imaginary part of Z, and we have again assumed that the system is spin degenerate by taking the occupancy, f, outside the sum. The ionic contribution is more straightforward:

$$\Delta\mathbf{P}_{\text{ion}} = \frac{e}{V_{\text{cell}}}\sum_I Z_I^{\text{ion}}(\mathbf{R}_I^{\lambda=1} - \mathbf{R}_I^{\lambda=0}), \tag{2.9}$$

where the sum goes over all of the ions in the unit cell.[7] Note that the charge Z^{ion} represents the *screened* charge (i.e. the nuclear charge minus the charge due to the core states) as we are typically working within the pseudopotential approximation.

Now, for a given state of the system, we can define the formal polarisation to be:

[5] i.e. functions that have exactly the same periodicity as the crystal itself.

[6] In fact this applies to all of the occupied bands, including the core states. Here, however, we shall work in the pseudopotential approximation, considering only the valence band contribution. The contribution to macroscopic polarisation due to the core states will be built into $\mathbf{P}_{\text{ion}}$ as explained in eqn. 2.9.

[7] One may wonder why it is legitimate to take such a sum in the case of ions, when we argued against it in the case of electrons. The reason is simply that we treat the ions as unambiguously identifiable, localised units, unlike the electrons.

$$\mathbf{P}_{\text{formal}}(\lambda) = \frac{ef}{(2\pi)^3}\,\text{Im}\sum_n \int_{BZ} d\mathbf{k}\,\langle u_{n\mathbf{k}}|\,\nabla_{\mathbf{k}}\,|u_{n\mathbf{k}}\rangle + \frac{e}{V_{\text{cell}}}\sum_I Z_I^{\text{ion}}\mathbf{R}_I^{\lambda}, \tag{2.10}$$

where $\mathbf{P}_{\text{formal}}$ equals the spontaneous polarisation, $\mathbf{P}_s$ if and only if the initial configuration is centrosymmetric with zero polarisation.[8] Having arrived at a formal definition of polarisation in eqn. 2.10, let us now examine the physical interpretation behind the integrand in eqn. 2.8.

Central to this discussion is the work of Michael Berry in his seminal 1984 paper [50]. Here, Berry shows that a quantum system taken adiabatically in a loop, L, with respect to some parameters of its Hamiltonian will acquire a global geometric phase, $e^{i\gamma(L)}$, due to a gauge potential. This gauge potential, or "Berry connection", takes the following form: $\mathbf{A}(\mathbf{k}) = i\,\langle u_{n\mathbf{k}}|\,\nabla_{\mathbf{k}}\,|u_{n\mathbf{k}}\rangle$. Many phenomena [51], most famously perhaps the Aharonov-Bohm (AB) effect, can be thought of in terms of a geometric phase. More recently, there has been a flurry of interest in the use of Berry phase concepts to explain and predict the properties of topological insulators [52]. In the case of macroscopic polarisation, we integrate $\mathbf{A}$ over the BZ (which can be seen as a closed surface), such that $\mathbf{P}_{\text{el}}$ can be thought of as a sum of Berry phases (scaled by some factors).

As a phase however, it is important to note that $e^{i\gamma(L)}$ is only defined modulo 2π; i.e. $e^{i\gamma(L)} = e^{i(\gamma(L)+2m\pi)}$, with m being some integer. This ambiguity in phase gives rise to the understanding of bulk polarisation as only being defined modulo some 'quantum of polarisation'. That is, polarisation is a multivalued vector quantity. Care must therefore be taken to ensure that, when performing calculations of bulk polarisation, one is consistent about the *branch* of polarisation that one is on.

Finally, we note that the Berry phase formalism can be made more intuitive by mapping the problem back into real space via a Fourier-like transformation. Doing so allows us to recover an intuitive, CM-like picture. This transformation is achieved via Wannier functions:

$$|w_{n,\mathbf{R}}\rangle = \frac{\Omega}{(2\pi)^3}\int_{BZ} d\mathbf{k}\,e^{i\mathbf{k}\cdot\mathbf{R}}\,|\psi_{n\mathbf{k}}\rangle, \tag{2.11}$$

where $|w_{n,\mathbf{R}}\rangle$ is the Wannier function associated with band n in unit cell $\mathbf{R}$ with a unit cell volume of Ω. Considering now the 'centres' of these Wannier functions, $\mathbf{r}_{n,\mathbf{R}} = \langle w_{n,\mathbf{R}}|\,\hat{\mathbf{r}}\,|w_{n,\mathbf{R}}\rangle$, we can write the electronic contribution to the formal polarisation from band n as:

$$\mathbf{P}_n = \frac{e}{\Omega}(\mathbf{r}_{n,\mathbf{R}} - \mathbf{R}). \tag{2.12}$$

This corresponds to assigning a unit point charge, $-e$, to each Wannier function centre. Together with the ionic charge assigned to the positions of the nuclei, we thus recover the easily identifiable units of polarisation that required in order for the CM picture

[8] Note that a centrosymmetric symmetric structure may have a non-zero formal polarisation if that polarisation is consistent with symmetry. For example, the ideal cubic perovskite structure may have a polarisation of mQ or of $\frac{mQ}{2}$, where m is some integer and Q is the so-called 'quantum of polarisation'.

to apply. Note that the aforementioned ambiguity in the branch of the Berry phase manifests itself here in terms of an ambiguity in the identification of the 'home unit cell' of the Wannier functions. That is, the Wannier function centres are only defined modulo a lattice vector, $\mathbf{R}$.

In the following chapter, having now seen how macroscopic polarisation can be thought of in terms of the acquisition of a Berry phase, we shall look into how to go about computing such a quantity from first principles.

3 | Theoretical background

In this chapter we introduce a mainstay of modern condensed matter theory: density functional theory (DFT). DFT is a powerful approach for predicting the properties of matter based on the laws of quantum mechanics. The key insight of DFT is that the Hamiltonian of a many-body system—and hence all of the system's ground state properties—is uniquely determined by the system's particle density [53].

At the time of writing this, DFT has become so ubiquitous within the condensed matter community that it can safely be regarded as textbook material. A chapter devoted to introducing its central concepts and theorems therefore may appear somewhat superfluous. The reasons for including a brief summary of DFT are threefold. Firstly as a matter of convenience to the reader; the concepts of DFT will appear throughout this work, and this chapter will hopefully serve as a simple reference for those relevant concepts, should it be needed. Secondly, although DFT is well established, it is useful to make explicit the language we shall be using in order to remove any ambiguity of convention or notation. Finally, in this work we employ several extensions and corrections to standard DFT that are necessary for accurately dealing with materials such as ferroelectrics. By discussing the fundamental and practical limitations of standard DFT, we motivate our use of such corrections, as well as providing some of the relevant theoretical background for understanding them.

The chapter is organised as follows: we start by laying out the motivation behind DFT and then introducing its central concepts. We go on to discuss the key approximations used in this work, with an emphasis on those that are of specific importance to the study of ferroelectric materials.

3.1 Dirac's challenge

In 1929 Paul Dirac famously wrote: "The underlying physical laws necessary for the mathematical theory of a large part of physics and the whole of chemistry are thus completely known, and the difficulty is only that the exact application of these laws leads to equations much too complicated to be soluble. It there fore becomes desirable that approximate practical methods of applying quantum mechanics should be developed, which can lead to an explanation of the main features of complex atomic systems without too much computation." [54] One way to paraphrase Dirac would be to say: 'chemistry would be easy, if it weren't so hard.' Before describing those practical approximate

methods used in this work, let us briefly comment on the reasons why Dirac a) thought it would be easy in principle and b) understood that it is hard in practice.

In almost any undergraduate quantum mechanics (QM) course, the lecturer gets her students to solve the Schrödinger equation for an isolated hydrogen atom. Reference is then often made to how the quantum numbers associated with the solutions of this equation (n, l, m) rationalise the structure of the periodic table of elements and that, in principle, similar equations govern all of chemistry.[1] Keen students may enquire after actual solutions to such equations for the other 117 (or so) known elements, perhaps for a molecule, or even a crystal. It becomes readily apparent, however, that most of these problems are intractable using similar analytic approaches. The heart of the difficulty lies in the many-body nature of the problem.

Consider the (non-relativistic) Hamiltonian describing the interactions of a system of N_{ion} nuclei and N_e electrons:

$$\begin{aligned}\hat{H} &= -\frac{1}{2}\sum_i \nabla_i^2 - \frac{1}{2}\sum_I \frac{1}{M_I}\nabla_I^2 \\ &\quad + \sum_{I,i}\frac{Z_I}{|\mathbf{r}_i - \mathbf{R}_I|} + \frac{1}{2}\sum_{I\neq J}\frac{Z_I Z_J}{|\mathbf{R}_I - \mathbf{R}_J|} + \frac{1}{2}\sum_{i\neq j}\frac{1}{|\mathbf{r}_i - \mathbf{r}_j|},\end{aligned} \tag{3.1}$$

where the lowercase subscripts index electrons and the uppercase subscripts index the nuclei. The mass, position and charges of each nucleus are given by: M_I, $\mathbf{R}_I$ and Z_I respectively. The position of electron, i, is given by: $\mathbf{r}_i$. Notice that we are working with atomic units and so $\hbar = e = m_e = 1/(4\pi\epsilon_0) = 1$. The first two terms of the Hamiltonian capture the kinetic energy of the electrons and nuclei. The final three terms correspond to the nucleus–electron, nucleus–nucleus and electron–electron interactions, respectively.

We can now write down the time-independent Schrödinger equation that is to be solved:

$$\hat{H}\Psi(\{\mathbf{r}_i\},\{\mathbf{R}_I\}) = E\Psi(\{\mathbf{r}_i\},\{\mathbf{R}_I\}), \tag{3.2}$$

where $\Psi(\{\mathbf{r}_i\},\{\mathbf{R}_I\})$ is the total many-body wavefunction for the system. In principle, Ψ contains all of the information there is to know about a system—all of its properties. However, Ψ has $3N_{ion}+3N_e$ spatial degrees of freedom and no general way of solving this exactly exists. One way to simplify the problem is via the so-called Born–Oppenheimer (BO) approximation in which the nuclear and electronic degrees of freedom are separated. This adiabatic approximation can be understood as assuming that, on the timescales of nuclear motion, the electrons are in a well-defined ground state.[2] The approximation corresponds to treating the nuclei as fixed and forming a fixed external potential in

[1] At least the mathematics of QM is meant to describe the most fundamental interactions of chemistry. This reductionist view, of course, neglects any emergent phenomena and higher-level concepts such as the notion of different types of bonding; an approach that irks many chemists.

[2] The justification for this is that the nuclei have a much greater mass than do the electrons.

which the electrons move.[3]

With the BO approximation, the problem now becomes one of solving for the electronic ground state wavefunction, Ψ_{el}. While this simplifies the challenge substantially, the many-body nature of the electron–electron interaction means that an exact solution to even this simpler problem is still beyond our reach. Hence Dirac's challenge to find practical approximate solutions.

While one may take issue with his extreme reductionism, the pursuit of Dirac's suggested research programme has certainly yielded enormous breakthroughs in physics and chemistry in the decades since 1929. The various approximate practical methods developed, too numerous to catalogue here, have each been optimised for certain classes of material and choices of speed versus accuracy. Broadly-speaking, the chemistry community has focussed on highly accurate, many-body methods targeted at small systems, and the physics community has focussed on more approximate, mean-field methods aimed at simulations of condensed matter.

The class of materials we wish to study in this work, namely ferroelectric and multiferroic materials, are typically large systems that nevertheless require full quantum mechanical treatment (as we have seen in section 2.4.2, for example). The method of choice, DFT, offers a reasonable compromise between speed and accuracy and is particularly well-suited to studying crystalline materials. In the following sections we shall see how DFT is, in principle, an exact reformulation of the Schrödinger equation, and examine the various fundamental and practical approximations that are typically made in order to use this method in practice.

3.2 Making the problem tractable: the Hohenberg-Kohn theorems

Formally, DFT begins with the two Hohenberg-Kohn (HK) theorems [53]:

Theorem 3.1. *Two fundamentally*[4] *different potentials cannot give rise to the same ground state charge density. In other words, the charge density uniquely, up to an arbitrary additive constant, determines the potential.*

Theorem 3.2. *For any given external potential* $V_{\text{ext}}(\mathbf{r})$*, the true ground state charge density,* $\rho(\mathbf{r})$*, is obtained by minimising the total system energy:*

$$E_{\text{tot}}[\rho(\mathbf{r})] = \int d^3r \; V_{\text{ext}}(\mathbf{r})\rho(\mathbf{r}) + F[\rho(\mathbf{r})], \tag{3.3}$$

where $F[\rho(\mathbf{r})]$ *is a universal (system independent) functional, of which we do not yet know the exact form.*

[3] A further approximation is almost always employed in which the nuclei are treated classically. For some light elements, however, a quantum mechanical treatment of the nuclei is required.

[4] By this we mean differing by more than merely an additive constant.

The Holy Grail of DFT is $F[p(\mathbf{r})]$ since to find this would be to reduce, *exactly*, all ground-state problems to minimisations over the charge density; i.e. reducing the spatial dimensionality from $3N_e$ (for the many-body wavefunction of an N_e electron system) to just 3 (for the charge density). While a great deal of effort has gone into finding the exact form of this universal functional, it remains as yet undiscovered. A key difficulty in discovering the exact form of $F[\rho(\mathbf{r})]$, or even good approximations to it, lies in the kinetic energy contribution. This contribution to the total energy is large (on the order of 50% for many systems) and so good estimates of this are of vital importance. However, accurately approximating the kinetic energy as a functional of electron density is extremely difficult.

Given the difficulties in finding the exact universal functional, most modern DFT employs a remapping of the problem to that of a system of non-interacting particles. This approach was developed by Kohn and Sham less than a year after the HK theorems were introduced.

3.3 A practical remapping: the Kohn Sham *ansatz*

In 1965, Kohn and Sham (KS) demonstrated [55] that we can construct an auxiliary system of non-interacting particles with the same density as the physical, interacting system of interest. The density of the KS system can be expressed in terms of single-particle orbitals, $\psi_n(\mathbf{r})$:

$$\rho(\mathbf{r}) = 2 \sum_{n}^{\text{occupied}} |\psi_n(\mathbf{r})|^2, \tag{3.4}$$

where the sum is over the occupied orbitals, and the factor of two arises from the assumption of spin degeneracy. The reintroduction of orbitals allows us to calculate the kinetic energy of the KS system exactly:

$$E_{\text{kin}}^{\text{KS}}[\rho(\mathbf{r})] = \frac{1}{2} \sum_{n}^{\text{occupied}} \int d^3r \psi_n^*(\mathbf{r}) \nabla^2 \psi_n(\mathbf{r}). \tag{3.5}$$

The Hartree energy (classical Coulomb interaction) can then be written as:

$$E_{\text{Har}}[\rho(\mathbf{r})] = \frac{1}{2} \int d^3r d^3r' \frac{\rho(\mathbf{r})\rho(\mathbf{r}')}{|\mathbf{r} - \mathbf{r}'|}. \tag{3.6}$$

Thus we can rewrite the universal functional, $F[\rho(\mathbf{r})]$ as:

$$F[\rho(\mathbf{r})] = E_{\text{kin}}^{\text{KS}}[\rho(\mathbf{r})] + E_{\text{Har}}[\rho(\mathbf{r})] + E_{\text{xc}}[\rho(\mathbf{r})], \tag{3.7}$$

where $E_{\text{xc}}[\rho(\mathbf{r})]$ is the so-called exchange-correlation (xc) energy, which captures the difference in energy between the fully interacting system of electrons and the KS system. Thus the xc functional is *defined* to be:

$$E_{xc}[\rho(\mathbf{r})] = E_{\text{kin}}[\rho(\mathbf{r})] - E_{\text{kin}}^{\text{KS}}[\rho(\mathbf{r})] + E_{ee}[\rho(\mathbf{r})] - E_{\text{Har}}[\rho(\mathbf{r})], \tag{3.8}$$

where $E_{\text{kin}}[\rho(\mathbf{r})]$ and $E_{ee}[\rho(\mathbf{r})]$ are kinetic and potential energy functionals of the interacting system (i.e. the true functionals of which we do not know the exact form).

We shall return to this *xc* functional below, but first let us note that this reformulation of the problem by Kohn and Sham is *exact* by construction;[5] that is to say there have been no further approximations made thus far.[6] In fact, given the definition of E_{xc}, it may seem as if we have simply rewritten the full Schrödinger equation to obscure the complex many-body terms without gaining very much. However, for many physical systems of interest, the E_{kin}^{KS} and E_{Har} terms together constitute almost all of the total energy, and these can be computed exactly in the KS picture using eqns. 3.5 and 3.6, respectively. Furthermore, simple and easy-to-compute approximations of E_{xc} have been found to be accurate for many systems of interest.

Now, using $\psi_n(\mathbf{r})$ again to represent the single particle KS wavefunctions, we can write a Schrödinger equation based on equations 3.7 and 3.3:

$$(-\frac{1}{2}\nabla^2 + V_{\text{KS}}(\mathbf{r}))\,\psi_n(\mathbf{r}) = \epsilon_n\psi_n(\mathbf{r}), \tag{3.9}$$

where $V_{\text{KS}}(\mathbf{r}) = V_{\text{ext}}(\mathbf{r}) + V_{\text{Har}}(\mathbf{r}) + V_{\text{xc}}(\mathbf{r})$, is the effective potential that the independent electrons experience. This is known as the Kohn-Sham equation.

A final, practical point to consider in trying to solve the KS equation is the circularity in the above formulation. Equation 3.9 suggests that we would need the density in order to obtain the orbitals; recall, however, that the density is defined in terms of these orbitals (eqn. 3.4). We get around this circularity by adopting an iterative approach: we first generate an initial trial density, then calculate V_{KS} and solve eqn. 3.9 to obtain the orbitals. We then calculate (via the eqn. 3.4) the density from the orbitals and compare this output density to our initial guess density. If the input and output densities are the same, then we have reached *self-consistency*. If the input and output densities are not the same (to within some tolerance) we use the output density as a new initial trial density and repeat. In practice, because this iterative loop is highly non-linear, we often need to employ certain techniques to converge on the correct density. Typically we obtain the next starting charge density by mixing in some of the density from previous steps. Several techniques to do this exist, ranging from a simple linear mixing scheme to more complex, weighted schemes [56–59].

3.4 Fundamental limitations with KS-DFT

3.4.1 Exchange and correlation contributions

As described above, the KS approach to DFT effectively maps our uncertainty with regard to the universal functional, $F[\rho(\mathbf{r})]$, onto the *xc* term, $E_{\text{xc}}[\rho(\mathbf{r})]$. The advantage of doing this is that the *xc* term is typically a small contribution to the total energy of

[5] Of course this has only been formulated for the ground state of the system, and in general does not hold for the excited states of the system.

[6] i.e. beyond the Born-Oppenheimer approximation discussed earlier.

the system, and so even relatively large errors in $E_{\mathrm{xc}}[\rho(\mathbf{r})]$ can nevertheless often yield quantitatively meaningful results.

Most approaches to approximating the *xc* functional are based on the homogeneous electron gas (HEG), for which we have very accurate approximations (for example from quantum Monte Carlo techniques [60]). The most simple of these, the local density approximation (LDA), assumes that for any infinitesimal region of charge density, the *xc* energy contributed by that region is simply equal to the *xc* energy of a HEG with that given density; i.e.

$$E_{xc}^{\mathrm{LDA}}[\rho(\mathbf{r})] = \int d\mathbf{r}\, \varepsilon_{\mathrm{xc}}^{0}(\rho(\mathbf{r}))\rho(\mathbf{r}), \tag{3.10}$$

where $\varepsilon_{\mathrm{xc}}^{0}(\rho(\mathbf{r}))$ is the *xc* energy per electron of a HEG with density $\rho(\mathbf{r})$.

To take into account the inhomogeneity of real systems, one might consider not only the electron density in a given region, but also the gradient of the density in that region, $\nabla\rho(\mathbf{r})$. However, early approaches to such an extension turned out to be *less* accurate than the LDA for most systems, owing to the fact that they violated known constraints on the true *xc* functional. To remedy this, Perdew, Burke and Ernzerhof (PBE) introduced a generalised gradient approximation (GGA) [61] that restored some of the known constraints and limiting behaviours of the true *xc* functional. This PBE-GGA (hereafter simply: PBE) represents a substantial improvement over the LDA in terms of accuracy for many systems, though it should be noted that it is still not a universal improvement. For example, the LDA has been found to more accurately predict the enthalpy of formation of InN than the GGA [62].

One can further improve the accuracy of a GGA, for particular properties and particular systems, by adjusting its various internal parameters. One of the more successful of these re-parameterisations is the so-called PBEsol functional in which the GGA parameters are chosen to improve predictions of lattice parameters and bond lengths in solids [63]. However, the gain in lattice constant accuracy typically comes at the expense of accurate cohesive energies [63]. More generally, empirical re-parameterisations tend to lose transferability[7] as they improve a specific property, or are optimised for a specific system type. Nonempirical GGAs, in which the internal parameters are chosen *ab initio*, are therefore often to be preferred in cases for which little is known empirically. The broad appeal of nonempirical GGAs is illustrated by the popularity of the PBE functional. For example, the paper that introduced PBE [61] was, as of 2014, the 16$^{\mathrm{th}}$ most cited paper of all time [64].

While the LDA and GGA *xc* functionals have been enormously successful in describing the properties of a wide range of matter, they tend to perform less well (or fail entirely) in a number of important cases. In the following section we discuss these failings: why they occur and how to overcome them.

[7] The transferability of a functional can either refer to how well it performs across different system properties, or to how it performs across different system types.

3.4.2 The delocalisation error

DFT, within the LDA or GGA, performs well for systems in which the electron density varies slowly in space. Conversely, DFT performs poorly for systems that have strongly localised electronic states (i.e. whose electron density varies rapidly in space). In order to see why, let us re-examine the electron–electron interaction.

As described above, KS-DFT is a mean-field approach. This means that any given electron interacts with some background electric field that is composed of *all* of the electrons in the system, i.e. including itself. This 'self-interaction', however, is spurious and needs to be cancelled out. In Hartree-Fock (HF) theory this is done explicitly and exactly, by including the exact exchange energy term:

$$E_x^{\mathrm{HF}} = -\frac{1}{2}\sum_{n,m}^{\text{occupied}} \int d^3r d^3r' \, \frac{\psi_n^*(\mathbf{r})\psi_m^*(\mathbf{r}')\psi_m(\mathbf{r})\psi_n(\mathbf{r}')}{|\mathbf{r}-\mathbf{r}'|}, \tag{3.11}$$

whilst in DFT it is done implicitly and approximately via the xc term. The failure of approximate xc functionals to perfectly cancel the self-interaction, known as the self-interaction error (SIE), results in a myriad of problems ranging from underestimated band gaps and chemical reaction barrier heights to overestimated charge-transfer binding energies and electric field responses.

A commonly used example to make the problem of self-interaction clearer is that of an $H_2{}^+$ molecule. If one considers separating the two H nuclei to a very large distance (beyond the dissociation limit), it is clear that whether the electron is localised on one hydrogen (i.e. $H + H^+$) or the other (i.e. $H^+ + H$), the system will have the same total energy. What about the case in which the electron is split over both such that each H ion has 'half an electron'; i.e. $H^{+0.5} + H^{+0.5}$? It turns out that this delocalised configuration would have exactly the same energy as those in which the electron is fully localised on one H or the other [65]. Hartree-Fock theory correctly predicts this;[8] DFT based on the LDA or GGA, on the other hand, incorrectly finds the delocalised configuration to have the lowest energy.

More generally, consider the energy of any system as a function of electron number. Perdew *et al.* [65] show that this function is composed of a series of straight line segments joining the energies at integer electron number. We sketch such a curve in Fig. 3.1 together with the LDA and HF curves. The convex nature of the LDA (or similarly for the GGA) is the cause of the systematic delocalisation error in DFT. The error is sometimes referred to as the 'derivative discontinuity error' since the LDA fails to capture the derivative discontinuity at integer electron number. A related argument concerning fractional *spins* (as opposed to fractional *charges*) can be made in order to explain the systematic error in static correlation in DFT [66, 67]. For more detail on the deficiencies of DFT from the fractional charge and fractional spin perspectives, see the review by Cohen, Mori-Sánchez and Yang [68].

[8] HF is exact in the limit of having only one electron.

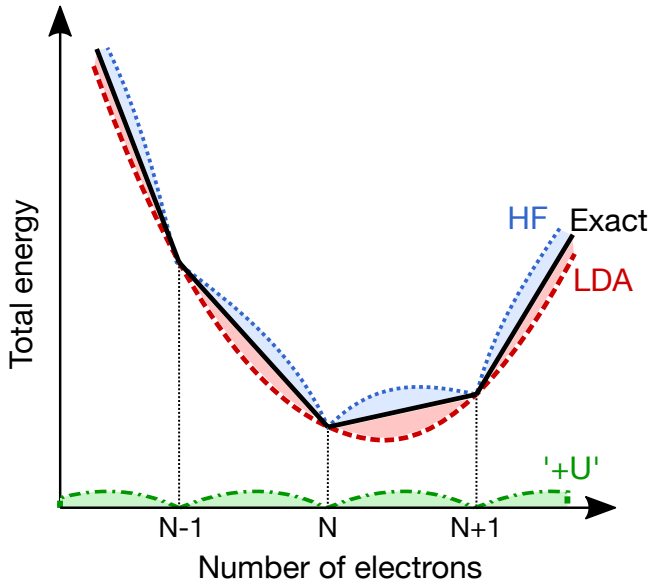

Figure 3.1: Sketch of the variation of total energy with electron number. Notice that HF has concave curvature (corresponding to a localisation error) whereas LDA has convex curvature (corresponding to a delocalisation error) for fractional electron number. The '+U' correction, discussed below, is meant to compensate for the delocalisation error of LDA.

3.4.3 Correcting for the delocalisation error

3.4.3.1 Hybrid functionals

As we mentioned above, in Hartree-Fock theory the self-interaction of the Hartree energy is exactly cancelled out by the E_x^{HF} term of eqn. 3.11. A reasonable approach to correcting the delocalisation error in DFT is therefore to incorporate some fraction of E_x^{HF} into the *xc* functional. An *xc* functional constructed in this manner—effectively combining aspects of DFT and HF theory—is known as a hybrid functional. An intuitive motivation for including this hybrid approach can be gained by re-examining Fig. 3.1. Because the LDA and HF curves have opposite curvature, building a functional that is composed of some fraction of LDA exchange and some fraction of HF exchange can approximate the exact curve (which has zero curvature) [69]. The fraction of exact exchange, α, can either be determined empirically [70] or via the adiabatic connection theorem [71].

While hybrid functionals, and in particular the screened-hybrid functionals, have been found to accurately predict many properties of ferroelectric materials [72], they typically come at a vastly increased computational cost relative to semi-local DFT functionals. For example, Stroppa *et al.* note that, for bismuth ferrite, the HSE functional [73] takes about 50 times more CPU time than the PBE functional per electronic minimisation step [72]. The high computational cost limits their use to relatively small systems. Systems that have breaks in translational symmetry, such as surfaces, defects or heterostructures, may require faster methods such as the meta-GGA or DFT+U approaches discussed

below.

3.4.3.2 Meta-GGAs

A natural extension of the GGA would be to include a dependence of the *xc* functional on the *second* derivative of the electron density, in addition to the first. So-called 'meta-GGA's have been developed that have such a dependence. More precisely, these meta-GGAs have a dependence on the orbital kinetic energy density, $\tau = 2\sum_n^{occ}(1/2)|\nabla\psi_n|^2$. By including a dependence on τ, in addition to ρ and $\nabla\rho$, meta-GGAs are able to more accurately predict band gaps for a large range of systems [74], indicating a reduction of the delocalisation error. Like the GGAs, the meta-GGAs can be parameterised either by examining the conditions that the exact *xc* functional must obey, or by fitting the parameters to known experimental results.

The recently developed SCAN functional [75] is constructed to satisfy all known exact conditions as well as some appropriate norms such as having uniform and slowly-varying densities. In a recent benchmark study [76] for ferroelectric materials (including bismuth ferrite), the SCAN functional was found be as accurate as the ferroelectric-optimised B1-WC hybrid functional [77–79]. Given that the computational cost of a SCAN calculation is only marginally greater than an LDA or GGA calculation, this approach is particularly appealing for large ferroelectric systems. .

3.4.3.3 DFT+U

Returning once more to Fig. 3.1, we see that another way to 'cancel' out the convex nature of the DFT curve—and thus to alleviate the delocalisation error—would be to combine it with the curve labelled '+U'. This so-called DFT+U[9] method was introduced by Anisimov *et al.* [80] to address the failure of the LDA to reproduce the behaviour of Mott insulators (LDA predicts that they should be metallic). Since then, and with developments due to Dudarev and others, the method has become widely used in the study of a broad range of systems beyond Mott insulators. In this section we outline the rationale behind the correction and give some details of the specific version employed in this work. For a more complete picture of the DFT+U method we recommend, in addition to the original papers cited below, the chapter by Matteo Cococcioni in Ref. 81.

Our starting point is the Hubbard model [82–87], developed by John Hubbard around the same time as Hohenberg and Kohn laid the groundwork for DFT. The model consists of N particles that may occupy lattice of sites, interacting with their immediate neighbours. The simplest, one-band Hubbard Hamiltonian is the following:

$$\hat{H}_{\text{Hub}} = -t \sum_{\langle i,j\rangle,\sigma} (\hat{c}^{\dagger}_{i,\sigma}\hat{c}_{j,\sigma} + c.c.) + U \sum_i \hat{n}_{i,\uparrow}\hat{n}_{i,\downarrow}, \tag{3.12}$$

[9] The term 'LDA+U' is often used synonymously with DFT+U in the literature, even when functionals other than the LDA are used with '+U'.

where the first sum represents the energy associated with a particle of spin: σ, hopping between nearest neighbour sites: $\langle i, j \rangle$ and with t being the hopping constant. This term effectively captures the kinetic energy of the system. The second sum represents the on-site energy with the constant, U, capturing the effective Coulomb repulsion of particles located at the same site. The operators, $\hat{c}^{\dagger}_{i,\sigma}$, $\hat{c}_{j,\sigma}$, and $\hat{n}_{i,\sigma}$ are the usual particle creation, annihilation and number operators, respectively.

Without going into too much detail, consider the limiting behaviour of t and U. In the limit of $t \ll U$, the energy gained by a particle hopping from one site to another is far outweighed by the energetic cost of having two particles at the same site. Since hopping is negligible in this limit, the particles are effectively localised to a particular site. At the other extreme, $t \gg U$, the total energy is dominated by the kinetic contribution and so total energy is minimised by effectively delocalising the particles.

Real materials, of course, can have a mixture of more localised (e.g. d and f states) and more delocalised states (e.g. s and p states) with DFT performing poorly for the former and well for the latter. The insight of Anisimov and co-workers [80, 88–90] was to realise that one could use a Hubbard-like term to describe certain chosen localised states, whilst letting DFT describe the rest. The basic DFT+U correction is therefore:

$$E_{\mathrm{DFT+U}}[\rho(\mathbf{r})] = E_{\mathrm{xc}}[\rho(\mathbf{r})] + E_{\mathrm{Hub}}[\{n^{I\sigma}_{mm'}\}] - E_{\mathrm{dc}}[\{n^{I\sigma}\}], \tag{3.13}$$

where E_{Hub} is a functional of the occupancies, $\{n^{I\sigma}_{mm'}\}$, of the chosen localised states at site I. E_{dc} is a double counting term—required since the energy contributions from the chosen states are already included in E_{xc}.

In 1998, building on earlier forms of the DFT+U method, Dudarev *et al.* [91] introduced a simplified version of this correction. We employ the Dudarev approach extensively in Chapters 4 and 5. According to this version, the Hubbard correction is given by:

$$E_U[\{n^{I\sigma}_{mm'}\}] = E_{\mathrm{Hub}}[\{n^{I\sigma}_{mm'}\}] - E_{\mathrm{dc}}[\{n^{I\sigma}\}], \tag{3.14}$$

$$= \frac{U - J}{2} \sum_{I,\sigma} Tr[\mathbf{n}^{I\sigma} - (\mathbf{n}^{I\sigma})^2], \tag{3.15}$$

in which only one parameter: $U_{\mathrm{eff}} = U - J$ enters. Notice that E_U acts to penalise non-idempotent orbital occupation matrices, i.e. those for which $\mathbf{n}^{I\sigma} \neq (\mathbf{n}^{I\sigma})^2$. Therefore, this correction will favour either fully occupied or fully unoccupied states.

The effective strength of this correction—governed by the U_{eff} parameter—has a large effect on the predicted properties of materials such as bismuth ferrite. In practice, U is often chosen such that a certain predicted property (e.g. band gap) fits that found in experiment. As will be discussed in detail in Chapter 4, however, great care is required to ensure unwanted effects are not introduced during this fitting.

3.5 Practical limitations and how to get around them

3.5.1 Basis sets

In order to perform numeric calculations for a given system, we need to represent the system's wavefunction in some basis set. The choice of basis set will depend on a number of considerations and usually involves some trade-off between desirable properties.

The first of these considerations is the suitability of a basis set to the system of interest. For example, a localised basis set made up of pseudo-atomic orbitals is particularly well-suited to an atomic or molecular system in that only a few basis functions are required to accurately describe the system's wavefunction. More precisely, we require that the basis set is well-adapted to the states of the system that we wish to describe. As we shall discuss below, we often make approximations regarding core electrons that allow us to only consider valence states explicitly. Making such approximations, we find that the 'nearly-free' valence states of an *sp* bonded metal, for example, are well described using plane waves, $e^{i\mathbf{G}\cdot\mathbf{r}}$.

A second consideration is the convergence behaviour of a particular basis set with respect to the basis set size. In most cases, the basis set used will be incomplete, leading to an error in predicted properties relative to that of a complete basis set. The manner in which this error decreases as one increases the basis set size is what we mean by 'convergence behaviour'. In the case of plane waves, convergence is smooth and systematic; i.e. the error due to an incomplete basis can be systematically reduced to a desired precision simply by increasing the basis set size. As it is relevant to Chapters 4, 5 and 6, we note that the size of a plane wave basis is usually specified in terms of an energy cut-off: $E_{cut} = (\hbar^2/2m_e)G_{cut}^2$, where all plane waves with a kinetic energy less than this are included. In the case of pseudo-atomic orbitals, the convergence with basis set size is much less straightforward or systematic.

A further practical consideration is the scalability of a given basis set, both in terms of its applicability for linear-scaling DFT approaches [92], and in terms of modern parallel processing more generally. The scalability of a plane wave basis set suffers from their real-space non-locality. That is, because plane waves are completely delocalised in real-space, one cannot easily divide up the unit cell into different parts to be handled by different processors for computational efficiency. Modern plane wave codes therefore parallelise by k-point and/or by band. A further consequence of this real-space delocalisation is that plane waves occupy the empty space that is sometimes used to separate periodic images (for example, when one wants to simulate an isolated molecule or a surface).

A final consideration is the difficulty in calculating certain quantities within DFT, most notably the forces on atoms. Force calculations are substantially simplified by the application of the Hellman-Feynman theorem. However, for basis sets that change with atomic position, such as pseudo-atomic orbtials, extra (Pulay) terms are required in order to calculate accurate forces.

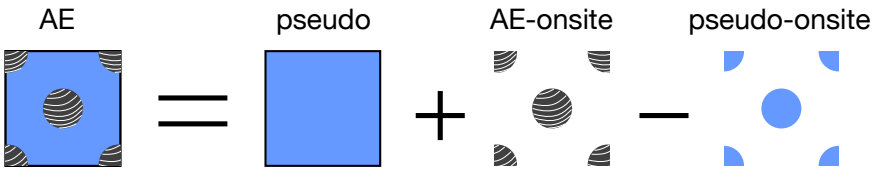

Figure 3.2: Schematic of the PAW method. The all-electron (AE) wavefunction is expressed as the sum of a pseudo-wavefunction and AE-onsite contributions. The pseudo-onsite contributions are subtracted in order to avoid double counting.

3.5.2 Dealing with the core electrons

The Coulomb potential between a positively charged nucleus and an electron, $V_{\text{ext}}(\mathbf{r})$, diverges as their separation decreases. This means that the wavefunction of an electron near the nucleus varies very rapidly (i.e. has a large kinetic energy). In terms of plane waves, this means that the wavefunction requires a very large number of plane waves in order to approximate it. Fortunately, however, we are very often not interested in the behaviour of states near the nuclei (core states) as they typically play no role in determining the chemical properties of a material. The effect of these core states on the valence states—apart from Pauli excluding them from the region close to the nucleus—is to screen them from the bare nuclear Coulomb potential. We can therefore replace the potential near the nucleus with a 'pseudopotential' which is much weaker than the bare Coulomb potential, provided the pseudopotential has the same net effect on the valence states. Note that, in addition to requiring a smaller basis set to describe the regions near the nuclei, once we have constructed the pseudopotential, we no longer deal with the core electrons explicitly – a double gain in computational efficiency!

However, care is required when constructing these pseudopotentials. In particular they must be made such that they are identical with the true potential outside of some cut-off radius, r_c, from the nucleus. Furthermore, the valence eigenvalues of the pseudopotential and the true potential must be identical. A final constraint is that of norm-conservation—i.e. the total charge of the pseudopotential and the true potential wavefunctions are required to be identical:

$$\int_0^{r_c} \left|\tilde{\psi}(\mathbf{r})\right|^2 r^2 d\mathbf{r} = \int_0^{r_c} |\psi(\mathbf{r})|^2 r^2 d\mathbf{r}, \tag{3.16}$$

where $\tilde{\psi}(\mathbf{r})$ and $\psi(\mathbf{r})$ are the wavefunctions associated with the pseudopotential and the true potential respectively. Note that the constraint of norm-conservation can be relaxed, by including extra terms, in order to construct *ultrasoft* pseudopotentials [93]. These require an even smaller plane wave basis set to reach convergence. The extra terms must a) recover the correct total charge density and b) compensate for the reduction in transferability of the pseudopotentials due to dropping the norm-conservation constraint [94].

Throughout this work we employ an alternative (though related) approach based on

the work of Peter Blöchl [95]. Blöchl's *Projector Augmented Waves* (PAW) method replaces the all-electron wavefunction by a combination of a) a smooth pseudo-wavefunction that describes valence states and b) a set of localised partial waves that describe core states. More precisely, the method consists of a linear transformation, $\hat{T}$, that maps some smooth pseudo-wavefunction to the true all-electron wavefunction:

$$|\psi\rangle = \hat{T}\,|\tilde{\psi}\rangle\,. \tag{3.17}$$

We can achieve such a transformation by separating $\hat{T}$ into onsite regions (often referred to as the *augmentation* region) and interstitial regions, with the pseudo-wavefunction coinciding with the true wavefunction in the latter. That is, we define:

$$\hat{T} = 1 + \sum_I \hat{T}^I, \tag{3.18}$$

where $\hat{T}^I$ is the onsite transformation, centred on atom I, and is only non-zero within the augmentation region defined by a spherical cutoff. Let us consider the AE and pseudo-wavefunctions within the augmentation region, expanding them in terms of the AE onsite ($|\phi_m\rangle$) and the pseudo-onsite ($|\tilde{\phi}_m\rangle$) partial waves:

$$|\psi\rangle = \sum_m c_m\,|\phi_m\rangle\,, \tag{3.19}$$

and

$$|\tilde{\psi}\rangle = \sum_m c_m\,|\tilde{\phi}_m\rangle\,. \tag{3.20}$$

Now we note that, since $|\psi\rangle = \hat{T}\,|\tilde{\psi}\rangle$, the coefficients, c_m, are equal in the two expansions. Thus we can write:

$$|\psi\rangle = |\tilde{\psi}\rangle + \sum_m c_m(\,|\phi_m\rangle - |\tilde{\phi}_m\rangle). \tag{3.21}$$

The coefficients, c_m, can be expressed in terms of an inner product with local[10] projector functions, $\langle\tilde{p}_m|$: $c_m = \langle\tilde{p}_m|\tilde{\psi}\rangle$. We can therefore write $\hat{T}$ as:

$$\hat{T} = 1 + \sum_m (\,|\phi_m\rangle - |\tilde{\phi}_m\rangle)\,\langle\tilde{p}_m|. \tag{3.22}$$

The projector functions are chosen to a) be localised within the augmentation sphere and b) to be orthonormal to the pseudo-onsite partial waves, i.e. $\langle\tilde{p}_n|\tilde{\phi}_m\rangle = \delta_{nm}$.

Now, comparing equations 3.17, 3.21 and 3.22, we find:

$$|\psi\rangle = |\tilde{\psi}\rangle + \sum_m (\,|\phi_m\rangle - |\tilde{\phi}_m\rangle)\tilde{p}_m\,|\tilde{\psi}\rangle, \tag{3.23}$$

[10] These are *chosen* to be localised within augmentation region, though in principle they could extend beyond it.

in which the terms are ordered as in the schematic Fig. 3.2. Thus the PAW method provides access to the AE wavefunction, albeit usually within the frozen-core approximation, at the computational cost of a pseudopotential method.

4 | Effects of the Hubbard U on density functional-based predictions of $BiFeO_3$ properties

Abstract

First principles studies of multiferroic materials, such as bismuth ferrite (BFO), require methods that extend beyond standard density functional theory (DFT). The DFT+U method is one such extension that is widely used in the study of BFO. In this chapter, we present a systematic study of the effects of the U parameter on the structural, ferroelectric and electronic properties of BFO. We find that the structural and ferroelectric properties change negligibly in the range of U typically considered for BFO (3–5 eV). In contrast, the electronic structure varies significantly with U. In particular, we see large changes to the character and curvature of the valence band maximum and conduction band minimum, in addition to the expected increase in band gap, as U increases. Most significantly, we find that the t_{2g}/e_g ordering at the conduction band minimum inverts for U values larger than 4 eV. We therefore recommend a U value of at most 4 eV to be applied to the Fe d orbitals in BFO. More generally, this study emphasises the need for systematic investigations of the effects of the U parameter not merely on band gaps but on the electronic structure as a whole, especially for strongly correlated materials.

4.1 Introduction

The magnetoelectric multiferroic material, bismuth ferrite ($BiFeO_3$; BFO), combines a spontaneous polarisation with an antiferromagnetic ordering in a single phase, at room temperature. This combination of properties makes BFO an interesting material for both fundamental research and a wide range of applications, from spintronics [96] to photovoltaics [97, 98]. In photovoltaic applications, the giant spontaneous polarisation ($\sim$100 $\mu C/cm^2$ [99, 100]) is thought to aid in charge separation via the bulk photovoltaic effect [10, 101]. Ferroelectric (FE) domains are thought to further enhance the photovoltaic prospects of BFO by allowing above-band gap photovoltages across the FE domains [11], and conduction along them [12].

Another attractive feature of the BFO system is the tunability of its properties with experimentally accessible changes to its crystal structure. A wide range of crystal structures with widely varying optoelectronic properties can be stabilised through the epitaxial strain engineering of BFO thin films [22, 102]. The subtle interplay between structural and electronic degrees of freedom that underlies the tunability of the BFO system, however, make this material particularly challenging to model. For example, the weak (Dzyaloshinskii-Moriya) ferromagnetism observed in BFO cannot be captured without including the effects of spin-orbit coupling (SOC) [21].

More generally, as discussed in Section 3.4.2 of the previous chapter, standard DFT methods are known to have systematic failures in describing the electronic structure of materials with strongly correlated d states, such as BFO. In particular, local density and generalised gradient approximations of the exchange-correlation (xc) functional incorrectly describe the on-site Coulomb interactions of highly localised electrons due to erroneous electron self-interaction.

In the previous chapter we outlined a number of methods that can improve the description of localised electronic states beyond the LDA and GGA. Hybrid functionals, in particular the Heyd-Scuseria-Ernzerhof (HSE) screened hybrid functional, have been shown to accurately capture many properties of BFO. However, these come at a vastly increased ($\sim$50$\times$) computational cost compared to standard DFT [72]. For simple bulk BFO, the additional cost is perfectly feasible on modern computer architectures. However, exciting developments in the study of BFO suggest that ferroelectric domains [12, 96, 103], doping [104, 105] and hetero-interfaces [106–110] with this material hold great technological promise. The theoretical investigation of such systems requires large simulation cells, which can be prohibitively expensive using hybrid functionals.

The 'DFT+U' method, by contrast, comes at essentially the same computational cost as an LDA or GGA calculation, but nevertheless offers a generally improved description of BFO's electronic structure. In theoretical studies of BFO, the approach of Dudarev *et al.* [91] is commonly used. In this approach (see Section 3.4.3.3), only a single parameter is used: $U_{eff} = U - J$. While the U_{eff} parameter can be obtained from *ab initio* calculations [81], it is typically chosen semi-empirically by comparing some predicted property to the available experimental data. The property used for calibration purposes depends on the intended aim of the study, with the electronic band gap and oxidation energies [111] being two of the most commonly chosen.

Careful tests are required, however, to ensure that other material properties are not adversely affected by one's choice of U_{eff}. For example, if U_{eff} is chosen such that the predicted band gap agrees with experiment, one should ensure that no significant error is introduced into the calculated lattice parameter as a result. Previous studies of the effects of the U_{eff} parameter have been conducted on the structural and electronic properties of BFO. Neaton *et al.* found that choosing a value of $U_{eff} = 4$ eV within the local spin density approximation (i.e. the LDA+U) improves the accuracy of the calculated lattice parameter, rhombohedral cell angle and the electronic band gap [20]. For their finite-temperature study of BFO, Kornev *et al.* used the scheme of Cococcioni

and de Gironcoli [112] to self-consistently determine the value of U within the LDA+U to be 3.8 eV [113]. However, they found that the parameters in their effective Hamiltonian were extremely sensitive to the value of U, stating that some of these parameters changed by about 20% when U was slightly reduced from 3.8 to 3.5 eV. Applying the U correction to the generalised gradient approximation (GGA+U), a U value of 5 eV was determined by Young *et al.* to most accurately reproduce the experimental imaginary permittivity near the band gap [114].

The effects of the U_{eff} parameter on the crystal structure, band gap and permittivity of BFO are therefore known, but those on other electronic properties have not yet been reported for BFO as far as we are aware. In this chapter we extend the systematic study of the U_{eff} parameter to include the curvature and character of the band edges in BFO. We find that the electron and hole effective masses, inversely proportional to the band curvature, are highly sensitive to the chosen value of U_{eff} and that the ordering of the Fe d orbitals at the conduction band minimum inverts for $U_{eff} > 4$ eV. These findings have important implications for theoretical studies of BFO and related materials, especially in cases where the charge carrier effective masses and band character play significant roles, such as those described in Chapter 5.

4.2 Computational details

All of the results presented here are based on DFT simulations using version 5.4.1 of the Vienna *ab initio* Simulation Package [115–118] (VASP). The calculations were carried out using the projector-augmented plane-wave method [95, 119], treating explicitly 15 electrons for Bi ($5d^{10}6s^26p^3$), 14 for Fe ($3p^63d^64s^2$), and 6 for O ($2s^22p^4$).[1] We use a plane-wave cut-off energy of 520 eV and perform Brillouin zone integrations on a Γ-centred $9 \times 9 \times 9$ Monkhorst-Pack mesh [120]. The GGA xc functional parameterised by Perdew, Burke and Ernzerhof (PBE) [61] is used throughout this chapter, with comparisons to the LDA, PBEsol [63] and more recent SCAN [75] functionals where appropriate.[2] We apply the effective Hubbard-like correction, U_{eff}, to the Fe d orbitals using the method of Dudarev *et al.* [91], varying the magnitude of U_{eff} between 0 and 8 eV.

We use the ground-state, rhombohedral BFO structure (space group: $R3c$) [121] as our model for all calculations. This phase exhibits a large spontaneous polarisation along the pseudo-cubic [111] direction ($[111]_{pc}$), primarily due to a Bi translation along this direction. This phase adopts a nearly G-type antiferromagnetic ordering [122] which we approximate as exactly G-type by using a 10-atom unit cell (two formula units), with the spin on the Fe atoms alternating along the $[111]_{pc}$ direction. See the insets in Fig. 4.2 for a depiction of the structure used.

As previously mentioned, SOC has been found to be significant in describing the

[1] The Bi, Fe and O PAWs are dated: 6th Sept. 2000, 2nd Aug. 2007 and 8th Apr. 2002 respectively

[2] Note that, for the studies using the SCAN functional, a later version of VASP (5.4.4) was used as this functional was not available in version 5.4.1.

weak ferromagnetism in BFO [21]. However, we find (and discuss in more detail in Chapter 5) that SOC negligibly affects the curvature and character of the band edges in $R3c$ BFO. In particular, for the $U_{eff} = 4$ eV relaxed structure, the calculated absolute hole effective mass increased from 0.748 m_0 with SOC to 0.763 m_0 without SOC, where m_0 is the electron rest mass. Similarly, the electron effective mass increased from 2.950 m_0 with SOC, to 3.017 m_0 without SOC. Such differences are significantly smaller than those being investigated here, and we therefore neglect SOC hereafter.

The following procedure was repeated for each value of U_{eff}, tested in the range $0 \leq U_{eff} \leq 8$ eV: first, a full geometry optimisation was performed in which the internal coordinates were relaxed such that the maximum force was below the finite-basis error of around 7 meV/Å; see Appendix A.1 for more details of the tests for convergence with respect to basis-set size and Brillouin zone sampling. The unit cell shape and size were optimised such that all stress components were smaller than 2 MPa. Following the geometry optimisation, an accurate self-consistent calculation was performed.

The spontaneous polarisation, P_s, was calculated using the modern theory of polarisation (MTP) [48, 123, 124]. Recall that, according to the MTP, only *differences* in polarisation are well-defined, and that bulk polarisation is best understood as a lattice of values [48, 123, 124]. In general, one needs to construct a ferroelectric switching path to resolve the ambiguity in the calculated polarisation—i.e. to find out on which branch of the polarisation lattice the calculated polarisation lies. By constructing such a switching path, we found that P_s is related to our raw calculated polarisation, P_{calc}, and the so-called quantum of polarisation, Q, via $P_s = P_{\text{calc}} + Q/2$. For more details on the necessity of this additional step in the context of BFO, see Ref. [20].

We calculate the hole and electron effective masses for value of U_{eff} as follows. The effective mass of a given band, n, at a particular location in reciprocal space, $\boldsymbol{k}$, is a 3×3 tensor quantity whose magnitude in a given direction is inversely proportional to the band curvature in that direction. m^* can therefore be defined as:

$$\left(\frac{1}{m^*}\right)_{ij} = \frac{1}{\hbar^2}\frac{\partial^2 E_n(\boldsymbol{k})}{\partial k_i k_j}, i, j = x, y, z, \tag{4.1}$$

where $E_n(\boldsymbol{k})$ is the energy dispersion relation for the n^{th} band, and i and j represent reciprocal space components. To obtain m^*, we first compute the full band-structure along a path of high symmetry. We then identify the location of the VB_{max} and the CB_{min} in reciprocal space. The band curvatures at these points correspond to the hole effective mass, m_h^*, and the electron effective mass, m_e^*, respectively. Having identified these k-points of interest, we employ the method and code outlined in Ref. 125 to obtain the full m^* tensors. In brief, the method involves generating a fine mesh around the k-point of interest, calculating the energy eigenvalues, and using a finite difference method to build up the tensor of second derivatives. The dependence of m^* on the spacing of this mesh was investigated, and spacings of less than 0.05 bohr^{-1} were found to give consistent results. For this work we calculate the eigenvalues of the effective

mass tensor, which correspond to the effective masses along the principle directions. In order to compare the effective masses at different values of U_{eff} we calculated the eigenvalues of each m^* tensor, which correspond to the m^* along the principle directions, and selected the smallest eigenvalue in each case.

Several alternative approaches to estimating m^* exist. One could, for example, focus on the curvature of a fixed band at a fixed k-point, for all values of U_{eff}. This has the benefits of being more straightforward, and of isolating changes in the curvature of the chosen band from changes to the location and character of the band edges. Another approach would be to average m^* across the whole of the lowest band or set of bands as was done by Hautier *et al.* [8, 9]. The latter approach is of particular value in cases where the bands around the Fermi level are very flat, since in such cases multiple band extrema become energetically relevant to conduction. In this work we choose to focus on the curvature of VB_{max} and CB_{min}, although the location may change with U_{eff}, in order to emphasise the role of these points in determining the response of the conduction electrons/holes. With this approach, we find that abrupt changes in m^* provides an indication of changes to the character of the band edges.

Finally, we computed the electronic density of states. We note that, because the FeO_6 octahedra do not align with the Cartesian axes in the rhombohedral unit-cell setting, VASP fails to correctly model the fine details of the projected DOS. In particular, in the rhombohedral setting, the DOS does not exhibit any of the typical splitting of the Fe d orbitals that one would expect given the octahedral environment of Fe. To obtain more detailed and accurate DOS projections we converted each of the relaxed structures into their 40-atom, pseudo-cubic, unit cell setting. Although the FeO_6 octahedral axes still do not line up perfectly with the Cartesian axes in this setting (due to the tilting of the octahedra), a clear splitting between the projected t_{2g} and e_g states is observed in this setting, as expected by symmetry. To obtain a more accurate DOS, a finer $11 \times 11 \times 11$ Monkhorst-Pack mesh was used, in addition to using the larger 40-atom unit cell.

The full VASP input files and structures are available, together with much of the analysis, in an online repository at Ref. 126.

4.3 Results and Discussion

4.3.1 Crystal structure

In Fig. 4.1 we plot the relaxed rhombohedral lattice parameter and angle as we vary U_{eff} in the PBE+U xc functional. We compare the response of the PBE+U functional to that of two other commonly used xc functionals: PBEsol+U and LDA+U, as well as to the newer SCAN functional. We find that, for the PBE, PBEsol and LDA xc functionals, increasing U_{eff} up to 4 eV leads to an increase in lattice parameter and a decrease in rhombohedral angle, in agreement with Neaton *et al.* [20]. We note that an increase in lattice parameter with U_{eff} represents an improvement in structural accuracy for the LDA+U because of its tendency to overbind. In contrast, because the PBE functional

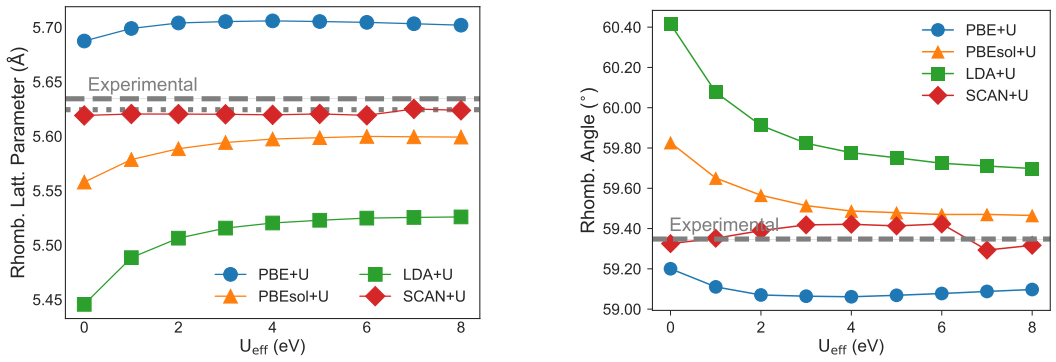

(a) (b)

Figure 4.1: Rhombohedral (a) lattice parameters and (b) cell angles as a function of U_{eff} across the PBE+U (blue circles), PBEsol+U (orange triangles), LDA+U (green squares) and SCAN (red diamonds) xc functionals. The grey dashed 'experimental' line in each comes from the 298 K structure from neutron diffraction results, provided in Ref. 121. The reported uncertainty of the experimental values is too small to be seen on this scale. In (a) we also show (grey dotted line) the reported lattice constant at 5 K from the high resolution synchrotron radiation diffraction results of Ref. 127.

underbinds BFO, an increase in lattice parameter constitutes a decrease in accuracy. Nevertheless, even the least accurate lattice parameter found with PBE+U ($< 1.3\%$ error, occurring when $U_{eff} = 4$ eV) is in better agreement with the experimental lattice parameter of 5.63443(5) Å [121], than the most accurate LDA+U value ($> 1.9\%$ error, occurring when $U_{eff} = 8$ eV). Interestingly, the PBEsol+U slightly overbinds BFO for all values of U, though performs significantly better than both the LDA+U and the PBE+U, with a lattice parameter error of 0.6% occurring when $U_{eff} = 5$–8 eV. The SCAN functional was found to have excellent agreement with the experimental unit cell for all values of U_{eff}.

The error in lattice parameter can be reduced even further—to $\approx 0.3\%$—by using the hybrid HSE functional, as reported by Stroppa *et al.* [72]. However, while very accurately reproducing the experimental lattice parameter, the authors note that this method requires around 50 times more computational time per self-consistent step than does plain PBE or PBE+U. The HSE method is therefore limited to small unit cells. For larger cells, such as those required to model defects, grain boundaries or domains, the more computationally cost-effective SCAN or DFT+U methods may be preferred. Stroppa *et al.* also report a PBE relaxed structure with which our PBE results is in near perfect agreement: our calculated lattice parameter for $U_{eff} = 0$ eV, 5.687 Å, agrees exactly (to all reported digits) with their results, and the rhombohedral angle differs by just 0.02°.

Interestingly, for U_{eff} larger than 4 eV, we see the trend in lattice parameter and rhombohedral angle reverse. This effect may be driven by the qualitative change in the electronic structure that occurs around $U_{eff} = 4$ eV (as discussed in section 4.3.3). However, further work would be needed to establish this link.

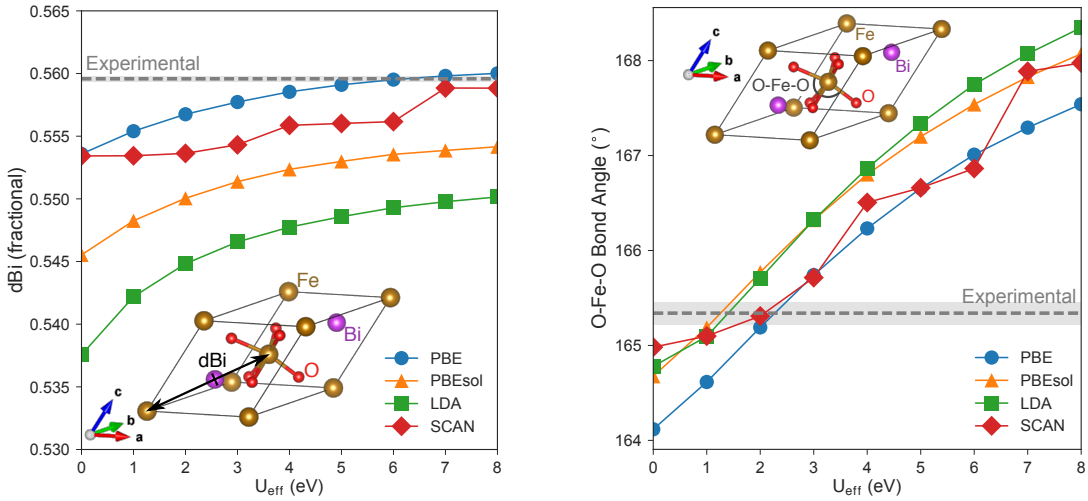

(a) Bi Translation (b) O–Fe–O Bond Angle

Figure 4.2: Effects of U_{eff} on (a) position of Bi along the $[111]_{pc}$ direction as a fraction of Fe–Fe separation, and (b) O–Fe–O bond angle. Results from PBE+U (blue circles), PBEsol+U (orange triangles), LDA+U (green squares) and SCAN (red diamonds) xc functionals are shown. The dotted 'experimental' line in each is measured from the (298 K) structure provided in Ref. 121, and the shaded range represents the uncertainty of those measurements. Note that in (a) this uncertainty is too small to be visible. The inset figures in each panel represent the $R3c$ structure and indicate the quantity being measured.

In addition to the changes in the unit cell parameters, we observe changes in the internal coordinates of the atoms, as U_{eff} is increased. We are particularly interested in the two key structural transformations in $R3c$ BFO relative to the cubic perovskite structure. The first is a translation of the Bi ions *along* the $[111]_{pc}$ direction; the second is an out-of-phase rotation of the FeO_6 octahedra *about* the $[111]_{pc}$ direction ($a^-a^-a^-$ in the notation of Glazer [128]). The former is the main driver for the large spontaneous polarisation in BFO, while the latter is thought to influence properties of BFO such as the charge carrier effective masses (see Chapter 5), polar order [107, 110] and spin state [18].

In Fig. 4.2a, we represent the translation of Bi by plotting its position as a fraction of Fe–Fe separation along the $[111]_{pc}$ direction. In the perfect cubic perovskite structure, a Bi atom would lie exactly halfway between two Fe atoms in the $[111]_{pc}$ direction (i.e. dBi= 0.5 as defined in Fig. 4.2a). Compared with the experimental fractional translation, $dBi_{exp} = 0.55958(18)$, we see an improvement in the description of the translation of Bi as U_{eff} is increased. At $U_{eff} = 6$ eV, dBi most closely matches that found in experiment. Note that we compare the fractional displacement of Bi (as opposed to absolute displacements), in order to take into account the changing lattice parameters at each value of U_{eff}.

In the $R3c$ structure of BFO, the FeO_6 octahedra are rotated about $[111]_{pc}$ by $\sim 14°$. We find that the angle of rotation changes by $\approx 0.4°$ when varying U_{eff} between

0 and 8 eV (for the PBE+U functional). Given that the angle of this rotation found in experiment spans the range 11–14° [129–131], we conclude that the change in octahedral rotation due to U_{eff} is negligible.

Another manifestation of the distortion of $R3c$ BFO with respect to the cubic perovskite structure is the deviation of the O–Fe–O octahedral angle from 180°. We find that the dependence of this angle on U_{eff} is also small, increasing (for PBE+U) from 164.1° to 167.5° as U_{eff} increases from 0 to 8 eV. In Fig. 4.2b we show this increase in O–Fe–O bond angle towards 180° as a function of U_{eff}. Nevertheless, all of the O–Fe–O angles predicted here are in reasonably good agreement with the experimental angle of 165.34(12)°, determined by high-resolution neutron diffraction at 298 K [121].

4.3.2 Polarisation

From the observed changes to the lattice geometry with varying U_{eff}, one might expect the spontaneous polarisation P_s to be affected. The increased Bi translation with U_{eff} would suggest an *increase* in P_s with increasing U_{eff} since the dipole moment per unit cell increases. However, as we have found the lattice parameter (and hence unit cell volume) increases with U_{eff}, we may expect an overall *decrease* in P_s as U_{eff} increases (recall that polarisation is inversely proportional to unit cell volume). We note that the structural changes due to U_{eff} may affect both the ionic and the electronic contributions to P_s. At the same time, independent of any structural changes, increasing U_{eff} itself may result in additional changes to the electronic contribution. We distinguish between structural and purely electronic effects by calculating P_s both for the PBE+U relaxed structures ('relaxed'), and for a chosen fixed structure ('fixed') in which we only vary U_{eff}. The fixed structure used for this purpose was that relaxed at PBE + U_{eff} = 4 eV.

In Fig. 4.3 we plot the variation in P_s with increasing U_{eff} for both the relaxed and fixed set of structures. There are two regimes present in Fig. 4.3: a sharp decrease in P_s with respect to U_{eff}, followed by much weaker dependence. The first regime, $U_{eff} \leq 2$ eV, can be explained by the sharp increase in lattice parameters. We note that the increase in lattice parameters dominates over the increase in Bi translation along $[111]_{pc}$ that would otherwise suggest an *increase* in P_s. The second regime, $U_{eff} > 2$ eV, in which we see a weaker dependence of P_s on U_{eff}, is dominated by changes only in the electronic structure, as the relaxed and fixed structure cases have the same dependence on U_{eff} beyond 2 eV.

As with the changes in lattice parameter and angles with U_{eff}, the most significant change in P_s occurs between a U_{eff} of 0 and 2 eV, with only minor changes thereafter. Since the typical values of U_{eff} chosen for Fe d orbitals in BFO lie between 3 and 5 eV [20, 104, 105, 113, 114, 132–135], the accuracy of calculated unit cell parameters and P_s depends more on the choice to use the DFT+U method at all, rather than on the particular value of U_{eff} one chooses. Thus, within the range of U_{eff} usually considered in the context of BFO, we conclude that the crystal structure varies negligibly with U_{eff}.

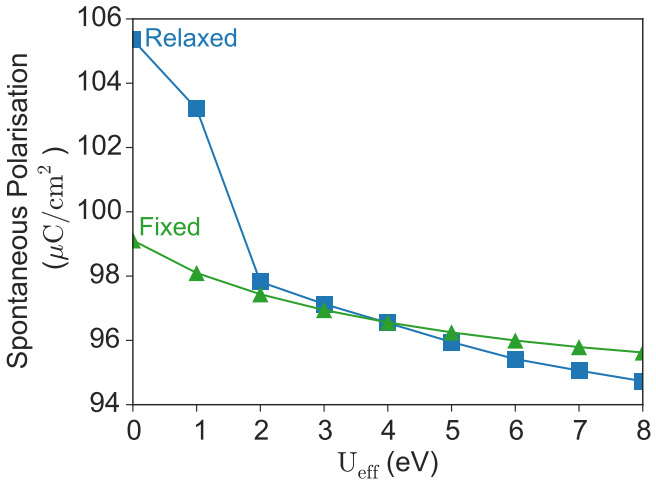

Figure 4.3: Variation in calculated spontaneous polarisation as a function of U_{eff}. We compare two cases: one in which we relax the structure fully for each value of U_{eff} (blue squares), and the second, in which we keep the structure fixed (green triangles) to that of $U_{eff} = 4$ eV.

4.3.3 Electronic structure

The influence of U_{eff} on the band character and curvature, often neglected in studies using PBE+U, will be the focus of this section. We quantify the curvature at the band extrema by calculating the charge carrier effective masses (Fig. 4.4), and represent the character using projected band structures and DOS (Fig. 4.5).

As with the polarisation, changes to the effective masses with U_{eff} can be broken down into structural contributions (by relaxing the structure at each U_{eff}) and purely electronic ones (by keeping the structure fixed in each case). In Fig. 4.4 we plot the electron and hole effective masses as a function of U_{eff} for both the relaxed and fixed structures.

For the relaxed structures we see a large reduction in the electron effective mass m_e^*: from 8.3 m_0 for $U_{eff} = 0$ eV to 0.6 m_0 for $U_{eff} = 5$ eV, indicating an increase in curvature at the CB_{min} with increasing U_{eff}. Between a U_{eff} of 5 and 8 eV we see little ($\sim$0.1 m_0) further change in m_e^*. The curvature of the VB_{max} also increases with U_{eff}, though most of the change occurs between a U_{eff} of 0 and 2 eV. The hole effective mass m_h^* decreases from 1.9 m_0 for $U_{eff} = 0$ eV to 0.7 m_0 for $U_{eff} = 2$ eV.

For the cases in which the structure was kept fixed to the $U_{eff} = 4$ eV relaxed structure, we see a similar dependence of m^* on U_{eff}. This similarity in trend between the relaxed and fixed structure cases indicates that changes in m_h^* and m_e^* with U_{eff} are dominated by changes purely to the electronic structure. The notable exception to this similarity is the m_e^* calculated for the fixed structure when $U_{eff} = 0$ eV ($m_e^* = 4.1$ m_0). The reason for this anomaly is a change in the location of the CB_{min} relative to all other $U_{eff} < 5$ eV cases. The CB_{min} for the anomalous result lies between Γ and $Z = [\frac{1}{2}, \frac{1}{2}, \frac{1}{2}]$, rather than exactly at Z as it is for the other $U_{eff} < 5$ eV cases. We attribute the change in location to the effective tensile strain resulting from using the $U_{eff} = 4$ eV relaxed

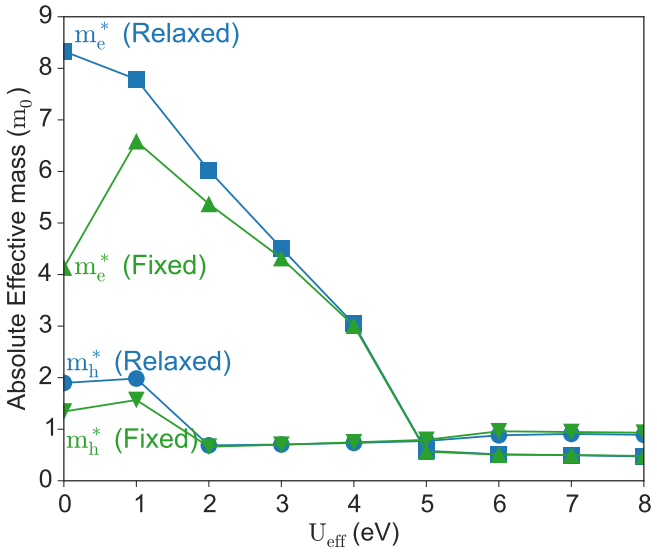

Figure 4.4: Absolute charge carrier effective mass versus U_{eff}. Blue squares and circles respectively represent the electron and hole effective masses for the PBE+U relaxed structures. Green triangles pointing up and down represent, respectively, the electron and hole effective masses for the fixed structure (fixed to the $U_{eff} = 4$ eV structure). m_e^* and m_h^* are the electron and hole effective masses, in units of the electron rest mass, m_0^*.

geometry; see Chapter 5 for more details on the effects of strain on m^* in BFO.

In order to explain the observed changes in m^* with U_{eff}, we investigate changes to the band character as U_{eff} increases. We represent the band character using the projected band structure shown in Fig. 4.5. The contributions from O, Fe and Bi to each band at each k-point are represented on a normalised colourspace by red, green and blue respectively. Similar figures comparing the projected bands of the PBE+U, PBEsol+U, LDA+U and SCAN+U xc functionals can be found in Fig. S6 of the SI [126]. We find only minor differences in the band structures of these xc functionals in terms of the trends identified below. In Fig. 4.5, we also present the projected density of states (pDOS) in order to resolve the contributions from individual orbitals.

Beginning with the character of the valence bands, we make the following observations. A change in the character of the topmost valence bands, occurring between a U_{eff} of 0 and 2 eV, is clear from the colour change in the bands. The change from a mix of red and green at $U_{eff} = 0$ eV to almost pure red at $U_{eff} = 2$ eV in the topmost valence band (VB) indicates a reduction in the Fe–O hybridisation, leaving O to dominate the VB_{max}. From the pDOS we resolve these contributions further: at $U_{eff} = 0$ eV, the top of the VB is made up of a hybridisation of O p and Fe e_g states; the character of these bands changes to primarily O p, with minor contributions from Bi s and Fe e_g states above a U_{eff} of about 2 eV. The change in the character corresponds to the decrease in m_h^* at $U_{eff} = 2$ eV. Given that the lattice vectors change most significantly in the 0 to 2 eV range of U_{eff}, we might expect that the changes to the crystal structure of BFO are driving this shift in band character. However, as we saw in Fig. 4.4, the associated pattern in m_h^* is similar in both the relaxed and fixed structure cases, indicating that

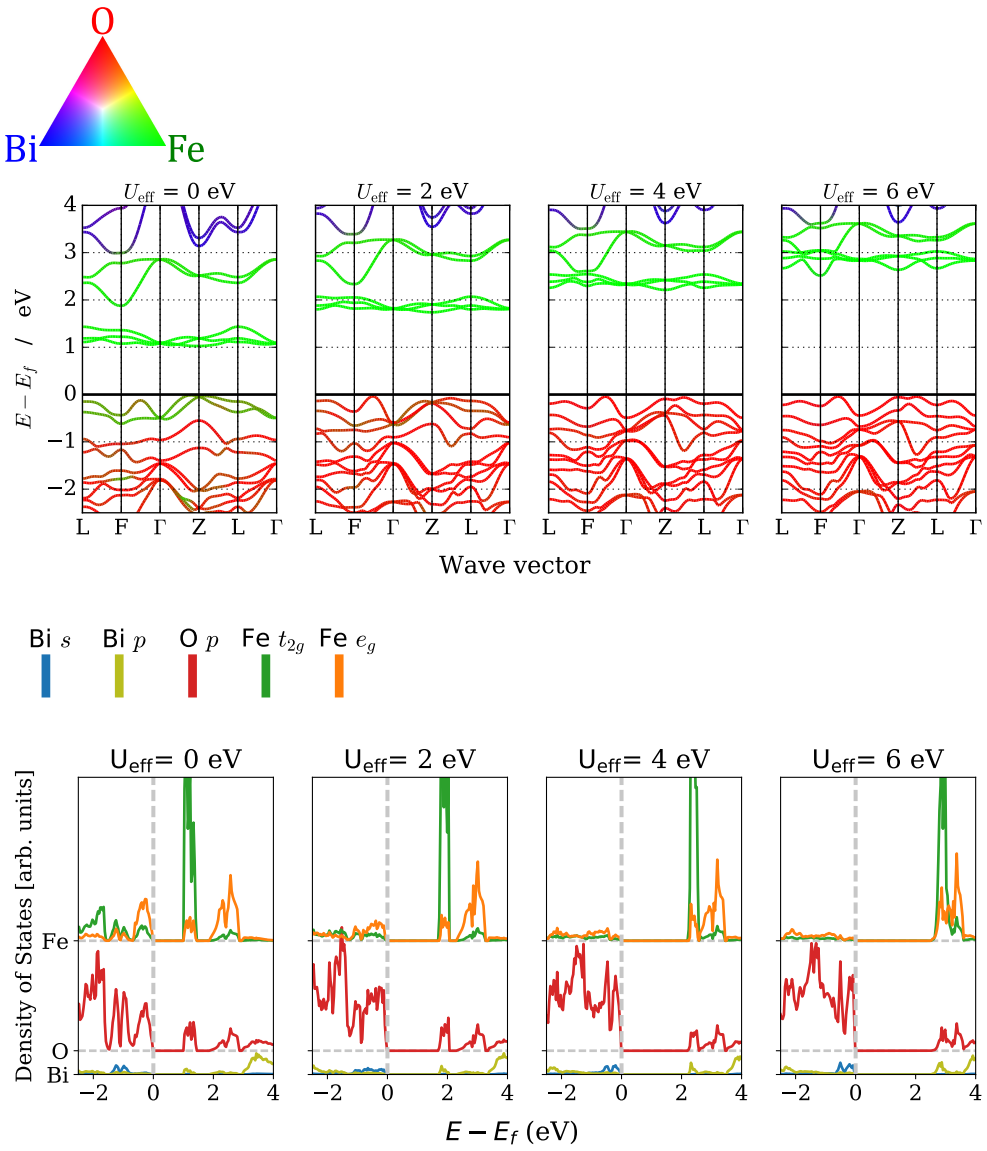

Figure 4.5: Variation in projected bands (top row) and density of states (bottom row) as a function of U_{eff}. The bands are coloured, at each k-point, based on wavefunction projections onto the elements. The contributions from O, Fe and Bi are represented on a normalised colourspace by red, green and blue respectively as shown by the colour triangle. The DOS is calculated in the pseudo-cubic setting in order to obtain accurate projections onto the selected atomic orbitals (indicated by the coloured vertical lines). Note that, since BFO adopts a G-type anti-ferromagnetic ordering, the spin up and spin down contributions are symmetrical. Here we are plotting the sum over both spin channels and over all atoms of each species.

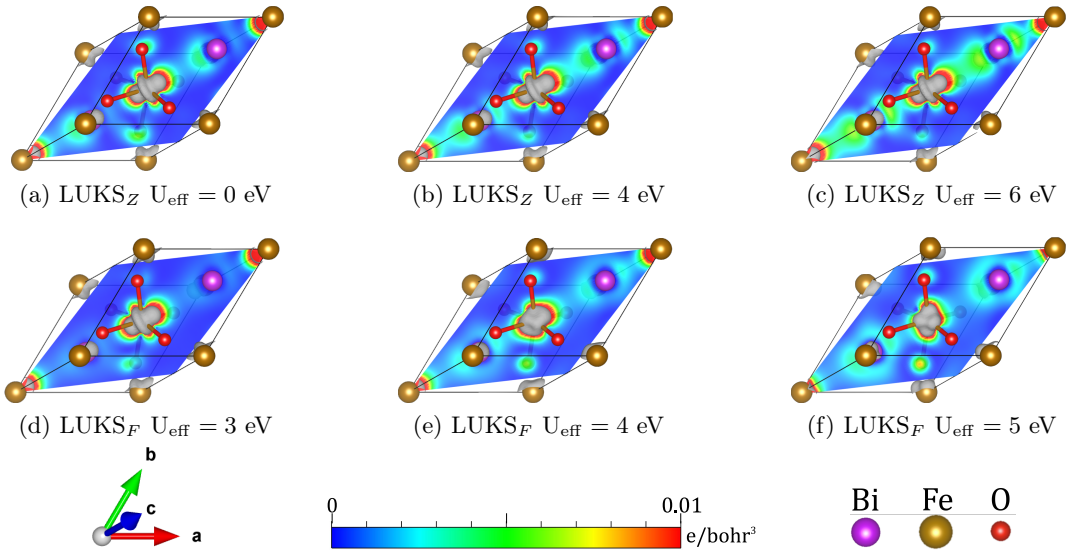

(a) LUKS$_Z$ U$_{\text{eff}}$ = 0 eV (b) LUKS$_Z$ U$_{\text{eff}}$ = 4 eV (c) LUKS$_Z$ U$_{\text{eff}}$ = 6 eV

(d) LUKS$_F$ U$_{\text{eff}}$ = 3 eV (e) LUKS$_F$ U$_{\text{eff}}$ = 4 eV (f) LUKS$_F$ U$_{\text{eff}}$ = 5 eV

Figure 4.6: PBE+U lowest unoccupied KS orbitals (LUKS) at the Z (a–c) and F (d–f) k-points for various values of U$_{\text{eff}}$. The KS orbitals are represented by a gray 0.02 e/bohr^3 isosurface. We plot the charge density from the KS orbitals in a $(1\,1\,\bar{2})$ plane, with colour saturation levels indicated by the colour bar.

the change is dominated by purely electronic effects. That this is not purely a structural effect is confirmed by observing the same shift in character in the projected bands and DOS for the fixed structure calculations, which can be found in Fig. S4 [126].

In addition to the decrease in Fe contributions to the VB$_{\text{max}}$, the pDOS shows that a Bi s antibonding peak moves up in energy from around 1.5 eV below the VB$_{\text{max}}$ for U$_{\text{eff}}$ of 0 eV, to the VB$_{\text{max}}$ itself for U$_{\text{eff}} \geq 2$ eV. The presence of a small Bi s contribution to the VB$_{\text{max}}$ is consistent with the HSE hybrid functional results by Stroppa and Picozzi [72]. An experimental study comparing VB$_{\text{max}}$ energies of BFO, Bi_2O_3 and Fe_2O_3 also proposes a non-negligible contribution from the Bi s states, as well as Fe d states, to the VB$_{\text{max}}$ of BFO [136]. The findings of these two previous works are better reflected in our calculated electronic structures of the VB$_{\text{max}}$ for U$_{\text{eff}} \geq 2$ eV.

From the projected conduction bands (Fig. 4.5), we see little change in the *elemental* contributions to the CB$_{\text{min}}$; Fe dominates the CB$_{\text{min}}$ for all U$_{\text{eff}}$ investigated here. The band structures do indicate, however, a change in the relative *orbital* contributions to the CB$_{\text{min}}$. We might expect the three lowest unoccupied bands to be Fe t_{2g} in character and the two next unoccupied bands to be Fe e_g, based on the octahedrally coordinated Fe. Indeed, we see at the Γ-point that the five Fe d bands form neatly into distinct triply and doubly degenerate sets. Detailed analysis of the crystal-field splitting in this system could be achieved using Wannier functions as in Ref. 137, though this lies beyond the scope of the present work. The designation of the five green (Fe) bands into t_{2g} and e_g groups in order of increasing energy is supported by the projected DOS, in which we see the energy difference between the e_g and t_{2g} manifolds decrease with an increase in U$_{\text{eff}}$. For values of U$_{\text{eff}}$ greater than 4 eV however, Fig. 4.5 suggests that one of the two Fe e_g

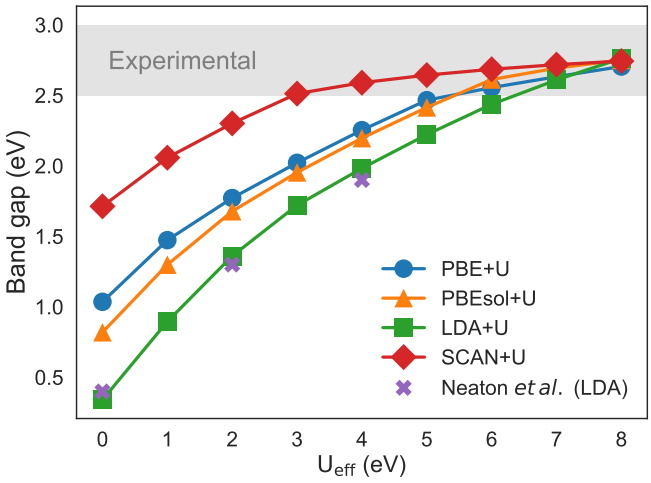

Figure 4.7: Variation in calculated electronic band gap as a function of U_{eff} for the PBE+U (blue circles), PBEsol+U (orange triangles), LDA+U (green squares) and SCAN (red diamonds) xc functionals. The range of band gaps reported in the experimental literature is shown as the shaded region. The LDA+U results reported by Neaton *et al.* (purple crosses) [20] are shown for comparison.

bands dips below the three Fe t_{2g} bands. That is, above a U_{eff} of 4 eV, the character of the CB_{min} transitions from Fe t_{2g} to Fe e_g.

To investigate the shift in orbital character from t_{2g} to e_g further, we plot the lowest unoccupied Kohn-Sham (KS) orbitals in Fig. 4.6. Because the CB_{min} is located at $Z = [0.5, 0.5, 0.5]$ for $U_{eff} \leq 4$ eV and at $F = [0.5, 0.5, 0.0]$ for $U_{eff} > 4$ eV, we plot the KS orbitals at each of these locations, for relevant values of U_{eff}. To visualise some of the more subtle changes, we plot the charge density from the KS orbitals in a $(1\,1\,\bar{2})$ plane, in addition to the isosurface. These plots highlight two distinct effects that U_{eff} has on the character of the CB_{min}.

Firstly, at the Z point (which is the CB_{min} for $U_{eff} < 5$ eV), there is a gradual increase in hybridisation between the Fe t_{2g} and Bi p orbitals along the $[111]_{pc}$ direction as U_{eff} increases, evident from the increase in intensity between Fe and Bi on the $(1\,1\,\bar{2})$ plane. This increase in overlap between Fe and Bi states contributes to the decrease in m_e^* between a U_{eff} of 0 and 4 eV.

Secondly, at the F point, we see a transition from t_{2g} to e_g character from the KS isosurface plot as U_{eff} increases from 3 eV to 5 eV, as expected from the band structures. Additionally we see a slight increase in intensity around the Bi and O atoms on the $(1\,1\,\bar{2})$ plane. The transition to e_g character is associated with a further decrease in m_e^*, possibly due to the increased overlap with O p states. Above 5 eV there is little change in the KS orbitals (see Fig. S3 of the SI [126]), and correspondingly, we see little change in m_e^*.

The significant shift in the location and character of the CB_{min} for $U_{eff} > 4$ eV suggests that $U_{eff} = 4$ eV be taken as a maximum, at least in cases for which the character and curvature of the CB_{min} plays a significant role.

Given that U_{eff} is sometimes chosen such that the calculated band gap matches that found in experiment, we now explicitly examine the effect of U_{eff} on the electronic band gap. We expect that, as U_{eff} increases, the band gap will increase due to the enhanced localisation of the Fe d orbitals. Indeed we see such a relationship in Fig. 4.7, where we plot the electronic band gap against U_{eff}. The trends across the PBE+U, PBEsol+U, LDA+U and SCAN+U functionals are similar, though the LDA+U gaps are significantly smaller than those of the PBE+U and PBEsol+U functionals for all $U_{eff} \leq 6$ eV. The SCAN functional, as expected for a meta-GGA, more accurately predicts the band gap than the LDA or either GGA. The LDA+U values are in excellent agreement with those found in Ref. 20, also plotted in Fig. 4.7. In Ref. 114, the PBE+U band gap is calculated from the theoretical optical absorption spectrum to be 2.58 eV for a U_{eff} of 5 eV. Their band gap value is 0.11 eV higher than the electronic band gap found in this work, 2.47 eV, for the same U_{eff} value.

In order to match the experimental band gap range of 2.5–3.0 eV [138–140], a U_{eff} of 5 eV or larger is clearly required for the commonly used LDA/GGA functionals (> 3 eV in the case of SCAN+U). As we have seen above however, the ordering of the Fe d orbitals at the CB_{min} inverts for $U_{eff} > 4$ eV[3], suggesting that fitting U_{eff} to the electronic band gap alone may introduce some spurious effects. While a $U_{eff} < 4$ eV underestimates the electronic band gap, we note that the DFT+U method can, at best, only correct the self-interaction error in the orbitals to which it is applied (in this case the Fe d orbitals). Self-interaction error from the other BFO orbitals, together with other sources of error intrinsic to Kohn-Sham DFT [141] are not accounted for in the '+U' correction. Furthermore, the experimentally reported band gaps are optical gaps rather than electronic (fundamental) gaps and thus will generally be lower in energy than the true electronic gap. That is to say, we ought to expect some remaining underestimation of the electronic band gap, even for the value of U_{eff} that most accurately localises the Fe d orbitals.

4.4 Conclusions

We have employed the DFT+U method to calculate the optimum crystal geometry and electronic structure of the $R3c$ phase of BFO for a range of U_{eff} between 0 and 8 eV, applied to the Fe d orbitals. We showed that the Bi displacement from its centrosymmetric position, the rotation of the FeO_6 octahedra, the distortion of the octahedra, and the spontaneous polarisation change negligibly within the U_{eff} range typically employed in the context of BFO.

The electronic structure, in contrast, varies significantly with U_{eff}, as designed: the application of U_{eff} is meant to correct the over-delocalisation of the states to which it is applied. With increasing U_{eff}, we find that the character of the states near the band edges changes, in addition to the band gap, leading to enormous changes in calculated

[3]This was found for the PBE+U method; similar values apply for the LDA+U, PBEsol+U and SCAN+U values. See the SI for more details [126].

charge carrier effective masses. In particular, the ordering of the Fe d orbitals at the CB_{min} inverts for U_{eff} values larger than 4 eV.

Using a U_{eff} of 4 eV leads to a 10–25% underestimation in the calculated band gap with respect to experimental values. To match the experimental band gap, a U_{eff} value of between 5 and 8 eV would be required. However, in this range of U_{eff}, the CB_{min} is Fe e_g in character rather than the Fe t_{2g} character found for U_{eff} values less than 5 eV. The widespread practice of selecting the U_{eff} parameter to match the experimental band gap therefore clearly needs to be exercised with caution, particularly in cases for which the character of the band edges play a significant role. We strongly recommend a thorough analysis of the effect of U_{eff} on the calculated electronic structure before proceeding with calculations that depend on the character of the band edges such as charge carrier effective masses, optical absorption energies and oxidation energies.

5 | Influence of crystal structure on charge carrier effective masses in $BiFeO_3$

Abstract

Ferroelectric-based photovoltaics have shown great promise as a source of renewable energy, thanks to their in-built charge separation capability, yet their efficiency is often limited by low charge carrier mobilities. In this chapter, we compare the photovoltaic prospects of various phases of the multiferroic material $BiFeO_3$ by evaluating their charge carrier effective masses from first-principles simulations. We identify a tetragonal phase with the promising combination of a large spontaneous polarisation and relatively light charge carriers. From a systematic investigation of the octahedral distortions present in $BiFeO_3$, we clarify the relationship between structure and effective masses. This relationship is explained in terms of changes to the orbital character and overlap at the band edges that result from changes in the geometry. Our findings suggest some design principles for how to tune effective masses in $BiFeO_3$ and similar materials through the manipulation of their crystal structures in experimentally accessible ways.

5.1 Introduction

As discussed in Chapter 1,the field of ferroelectric (FE) photovoltaics, dating back to 1956 [15], experienced something of a renaissance in 2009 with the discovery of the switchable diode and bulk photovoltaic effects (BPVE) in the multiferroic material, bismuth ferrite ($BiFeO_3$; BFO) [16]. The BPVE, observed in BFO, arises from the absence of inversion symmetry in the crystal structure of the room temperature, $R3c$ phase [10]. This asymmetry results in a giant spontaneous polarisation ($\sim 100\mu C/cm^2$)[99, 100], thus setting up an in-built bias in the bulk that aids in charge separation in a photovoltaic device.

We should note that there are several proposed contributing (and sometimes competing) mechanisms to the BPVE; these may be separated into intrinsic and extrinsic effects. Young and Rappe have demonstrated that the intrinsic 'shift-current' mechanism

plays an important role in the BPVE in BFO [114]. According to this model, charge carrier separation in the BPVE is driven by coherent excitations, rather than a built-in electric field. In a monodomain FE material, therefore, the magnitude and direction of the photocurrent does not necessarily depend on the magnitude or orientation of the FE polarisation; it is sufficient to have an absence of inversion symmetry. Extrinsic mechanisms include factors such as FE domains, point defects and band bending due to surfaces.

Despite the intrinsic charge separation ability, FE materials such as BFO generally suffer from limited device efficiency due to low charge carrier mobilities which lead to high recombination losses [142–144]. Increasing the mobilities in such FE materials would therefore lead to enhanced photovoltaic device efficiency.

Although mobility is a macroscopic quantity, it is the mobility associated with the electronic band edges that is of particular relevance to recombination rates. Since mobility is directly related to the dispersion of these bands, a material's charge carrier mobilities can be altered by modifying the curvature of the bands near the Fermi level. Manipulation of the crystal structure, for example by strain engineering, is one such route to tuning the curvature of electronic bands. Strain engineering, together with chemical doping, have been widely exploited in the semiconductor industry to control mobility in silicon-based devices [145]. In BFO, a wide range of crystal structures can be stabilised through strain [22, 102] and interface [109, 110] engineering. These structures include both FE and non-FE ones, of which the former are of particular interest for photovoltaic applications. There has been a great deal of interest in the tetragonal (spacegroup: $P\,4\,m\,m$) and tetragonal-like phases of BFO thin films, in particular, due to their giant spontaneous polarisation of *ca.* 150 $\mu C/cm^2$ [22, 102].

How do the mobilities of the charge carriers compare across the BFO phases? In this chapter, we present an investigation within density functional theory (DFT) of the electronic properties of several FE and non-FE phases of BFO. We begin by considering the ground-state $R\,3\,c$ phase, the higher temperature orthorhombic $P\,n\,m\,a$ and cubic $P\,m\,\bar{3}\,m$ phases, and the prototypical tetragonal $P\,4\,m\,m$ phase. We also consider the theoretical $R\,\bar{3}\,c$ phase, which is similar to the $R\,3\,c$ phase but without the ionic displacement that gives the latter its spontaneous polarisation. We compare the charge carrier effective masses (m^*), which are inversely proportional to the mobilities, across these phases. We will show that the carriers in the ground-state FE phase ($R\,3\,c$) have considerably higher m^* compared to some non-FE phases. Nonetheless we find that the tetragonal phase ($P\,4\,m\,m$) of BFO, which has a large spontaneous polarisation, has relatively low electron and hole effective masses.

In order to explain the differences in m^* across the BFO phases, we systematically study the geometric transformations that map the BFO phase with the lowest m^*, to the phase with the highest m^*. The effects of these transformations on the m^* are explained in terms of changes to the orbital character and overlap at the band edges. Previous works [22] have indicated that, with a judicious choice of substrate material, a BFO lattice with the desired spontaneous polarisation and m^* can be fabricated. Our

results therefore provide insight towards the rational design of materials with optimum properties, particularly for applications in light harvesting.

5.2 Computational details

We consider the $R3c$, $Pnma$, $P4mm$, $Pm\bar{3}m$ and $R\bar{3}c$ phases of BFO. Simulations of these phases were performed using DFT as implemented in VASP (version 5.4.1) [115–118]. We employed the PBE [61] GGA as the exchange-correlation functional, with an effective Hubbard correction (U_{eff}) applied to the Fe d orbitals using the method of Dudarev *et al.* [91]. In the previous chapter we discussed, at some length, the effect of the U_{eff} on the properties of BFO, focussing on the character and curvature of its band edges. Here we use the recommended $U_{eff} = 4$ eV for all calculations.

The projector-augmented plane-wave method [95, 119] was used throughout, with a plane-wave cut-off energy of 520 eV, treating explicitly 15 electrons for Bi ($5d^{10}6s^26p^3$), 14 for Fe($3p^63d^64s^2$), and 6 for O ($2s^22p^4$).[1] A 40-atom, pseudocubic (pc) unit cell setting was used for all but the effective mass calculations in section 5.3.2 which, for reasons of efficiency, were performed using a 10-atom rhombohedral cell. Brillouin zone integrations for the relaxations and static calculations were performed on Γ-centred Monkhorst-Pack (MP) [120] grids: $9 \times 9 \times 9$ for the pc unit cells and $11 \times 11 \times 11$ for the rhombohedral unit cells. Density of states (DOS) calculations, requiring finer sampling of the Brillouin zone, were performed using a Γ-centred $11 \times 11 \times 11$ MP grid in the pc unit cell setting. We relaxed the low-energy phases of BFO such that all force components were less than 5 meV/Å. The unit cell shape and sizes of these phases were optimised such that all stress components were smaller than 0.06 GPa. All of the structure files and raw data are available, together with the code used for analysis, in an online repository of supplementary information (SI) at Ref. 146.

We use the modern theory of polarisation (MTP) [48, 124] to calculate the spontaneous polarisation of each structure. As noted in the previous chapter, much care is needed when performing these calculations, especially in systems such as BFO for which the spontaneous polarisation, P_s, is of the same order of magnitude as the quantum of polarisation, Q. We again follow the procedure outlined in Ref. 20.

We calculate the hole and electron effective masses for each of the considered BFO phases following the procedure outlined in the previous chapter. We again compute the eigenvalues of the effective mass tensor, which correspond to the effective masses along the principle directions. We quote the smallest of these eigenvalues as 'the' effective mass of the phase; the full m^* tensors can be found at Ref. 146.

To make the calculations tractable, we limit ourselves to a collinear treatment of spin, thus neglecting the long-wavelength ($\sim$ 620 Å) spiral spin structure found experimentally [122]. All of the low-energy phases in the present chapter, with the exception of the $P4mm$ phase, are found to adopt a G-type antiferromagnetic (AFM)

[1] The Bi, Fe and O PAWs are dated: 6th Sept. 2000, 2nd Aug. 2007 and 8th Apr. 2002 respectively

ordering, consistent with previous work [147]. The C-type AFM ordering was found to be slightly lower (6 meV /f.u.) in energy than the G-type ordering for the $P\,4\,m\,m$ phase, again in agreement with previous work [147, 148]. A change from G-type to C-type ordering in the $P\,4\,m\,m$ phase had little effect on the character or curvature of the band edges.

5.3 Results

5.3.1 Effective masses of the phases of BFO

Table 5.1 shows the calculated m^*, polarisation and relative stability of the considered BFO phases. The results for the relative stability agree well with the literature, differing by at most 5% with respect to the PBE+U ($U_{eff} = 4$ eV) work of Diéguez *et al.* [147]. For the FE $R\,3\,c$ phase, the calculated P_s agrees well with both experiment and theory, which report values of between 90–100 $\mu C/cm^2$ [20, 100, 149, 150]. For the tetragonal $P\,4\,m\,m$ phase, we find a P_s of 185 $\mu C/cm^2$, larger than those reported in previous theoretical (151–152 $\mu C/cm^2$ [147, 151] and experimental ($\sim$ 130 $\mu C/cm^2$ [152]) works. The difference between the theoretical results obtained here and those reported in the literature might be attributed to our larger c/a ratio: 1.30 here compared to 1.27–1.28 in Refs. 147, 151. Another possible source of discrepancy is the quantum of polarisation. Because a simple linearly interpolated ferroelectric switching path does not remain insulating along the entire pathway (within the PBE+U framework), some ambiguities remain as to which branch of the polarisation one is on. Thus reported differences in polarisation may differ by a quantum of polarisation (in this case $\sim$ 30 $\mu C/cm^2$). The results presented here are, however, consistent with independent polarisation estimates using Born effective charges.

Comparing the charge carrier effective masses, reported in Table 5.1, we find the room-temperature FE phase of BFO ($R\,3\,c$) to have largest m_e^*, and the second largest m_h^*. The tetragonal $P\,4\,m\,m$ phase, which is also ferroelectric, has an m_e^* an order of magnitude smaller and an m_h^* 20% smaller than those of $R\,3\,c$. The paraelectric $R\,\bar{3}\,c$ phase has an m_e^* comparable to that of $P\,4\,m\,m$ and an m_h^* comparable to that of $R\,3\,c$. Both m^* are smallest in the paraelectric $P\,m\,\bar{3}\,m$ phase. From these results we therefore observe that the ferroelectric phases do not necessarily have lower m^* than the paraelectric phases.

To gain insight into the variation of m^* with the phases, we examine and compare the electronic structures of the BFO phases, particularly at the band edges—the locations at which the m^* are evaluated. In Fig. 5.1 the band structure and DOS, projected onto spherical harmonics, are shown for each phase of BFO studied here. Considering the lowest lying conduction bands in order of decreasing m_e^*, i.e. from $R\,3\,c$, $P\,n\,m\,a$, $R\,\bar{3}\,c$, $P\,4\,m\,m$ to $P\,m\,\bar{3}\,m$, we see that the major contribution to the states at CB_{min} gradually changes from Fe t_{2g} to Bi p. In Fig. S1 of the SI [146], we plot the corresponding Kohn-Sham (KS) orbitals. These orbital plots corroborate the spherical harmonic projections,

Table 5.1: Computed effective masses in units of electron rest mass, m_0, spontaneous polarisation values and relative energies of five PBE+U relaxed phases of BFO. Note that energies, E, are taken relative to the most stable phase: $R3c$.

Spacegroup	$\lvert m_h^* \rvert$ (m_0)	m_e^* (m_0)	Polarisation ($\mu C/cm^2$)	$E - E_{R3c}$ (meV per f.u.)
$Pm\bar{3}m$	0.34	0.24	0.0	971
$R\bar{3}c$	0.63	0.37	0.0	268
$P4mm$	0.54	0.33	185.3	84
$Pnma$	0.95	0.99	0.0	57
$R3c$	0.67	3.06	90.0	0

indicating that Fe t_{2g} states are the primary contributors to the CB_{min} for the $R3c$, $Pnma$ and $R\bar{3}c$ phases, while the Bi p states make up the CB_{min} for the $P4mm$ and $Pm\bar{3}m$ phases. Our results suggest that, at the CB_{min}, the presence of Bi p states leads to a lower m_e^* than that of Fe t_{2g} states.

Compared to the conduction bands, the topmost valence bands in Fig. 5.1 show a far less dramatic difference in character across the five phases. All of the phases considered here have an O p dominated VB_{max}. However, there are minor contributions from Fe e_g states to the VB_{max}, most notably in the $Pm\bar{3}m$ phase. To see more clearly the variation in the states at the VB_{max}, we show in Fig. 5.2 the cross-sections through KS orbitals corresponding to the topmost valence band. The figures show that, as m_h^* decreases from $Pnma$, $R3c$, $R\bar{3}c$, $P4mm$ to $Pm\bar{3}m$, the contribution from the Fe e_g states increases. This observation indicates that the presence of Fe e_g states at the VB_{max} plays a role in decreasing m_h^*.

5.3.2 Effects of structural transformations on effective masses

The different crystal structures of the BFO phases considered have been found to have a wide variation in the electronic structures and, in particular, in their charge carrier effective masses. As such, a substantial yet complex relationship exists between crystal structure and effective mass in BFO. In order to better understand this relationship, we now consider the geometric transformations that map the phase with the lowest effective masses, $Pm\bar{3}m$, to the phase with the largest effective masses, $R3c$. These transformations are: a) an antiphase rotation of the FeO_6 octahedra about the $[111]_{pc}$ direction (i.e. $a^-a^-a^-$ in Glazer's notation [128]), and b) a translation of the FeO_6 octahedra along the $[111]_{pc}$ direction. These transformations are illustrated in Fig. 5.3. More generally, these and similar geometric transformations can describe the other BFO phases, portrayed in Fig. 5.4, as follows:

- $Pnma$: an octahedral rotation out-of-phase along the $[100]_{pc}$ and $[010]_{pc}$ directions but in-phase along the $[001]_{pc}$ direction ($a^-a^-c^+$); and antipolar distortions in the $[110]_{pc}$ direction
- $R\bar{3}c$: an out-of-phase rotation about the $[111]_{pc}$ axis ($a^-a^-a^-$) with no translation

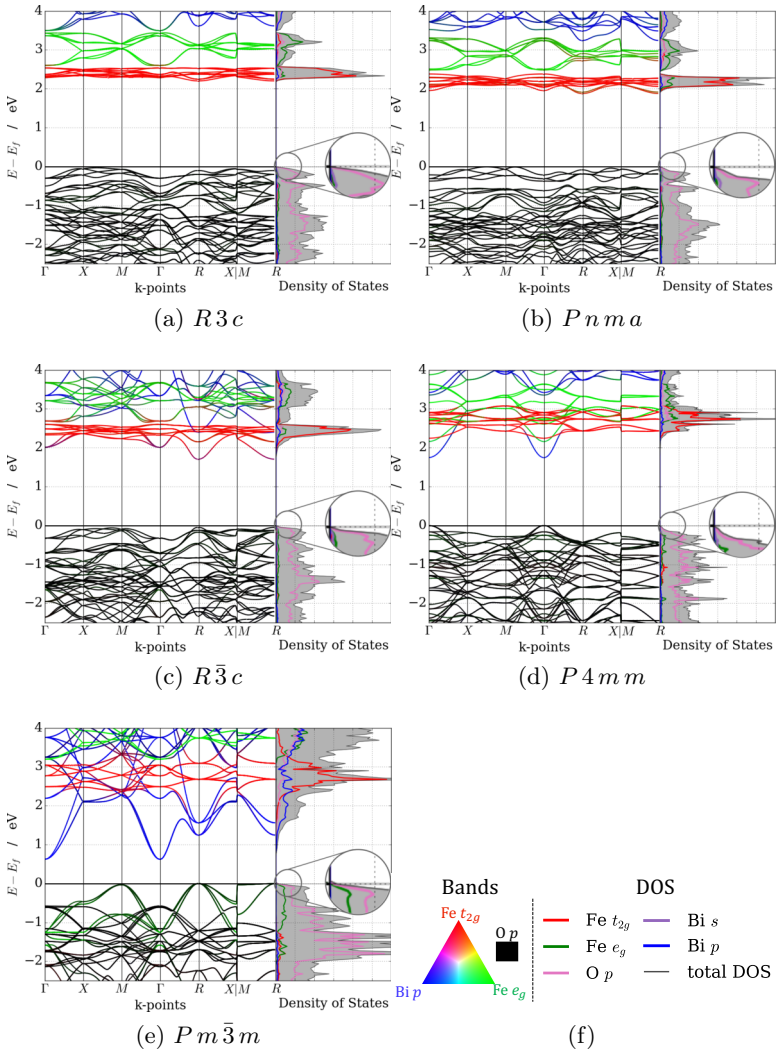

Figure 5.1: Projected bands and DOS for the (a) $R3c$, (b) $Pnma$, (c) $R\bar{3}c$, (d) $P4mm$ and (e) $Pm\bar{3}m$ phases of BFO, in their (pseudo-) cubic settings. The bands are coloured, at each k-point, based on wavefunction projections onto chosen orbitals. As indicated in the legend, red, green, blue and black represent projections onto Fe t_{2g}, Fe e_g, Bi p and O p states respectively.

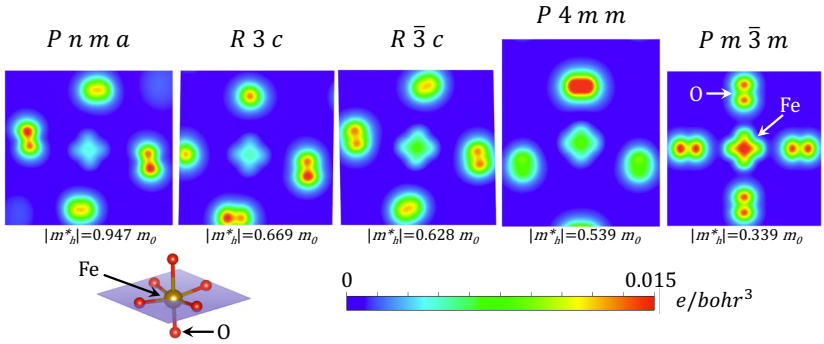

Figure 5.2: Kohn-Sham orbitals corresponding to top VB, summed over all k-points, for the five phases of BFO investigated. These are representative cross-sections through the FeO_2 plane in the case of the perfect cubic $P\,m\,\bar{3}\,m$ structure, and at least two O atoms and one Fe atom in the other phases, as illustrated in the bottom left diagram. The locations of the Fe and O atoms are labelled in the $P\,m\,\bar{3}\,m$ section, and the hole effective masses, m_h^* are shown below each panel for ease of reference. The full 3D data files are available in the SI [146].

- $P\,4\,m\,m$: no rotation but with a substantial polar distortion along the $[001]_{pc}$ direction

These transformations are accompanied by some strain to accommodate the change in the structure. We therefore consider the effects of strain, rotation and translation separately, particularly in relation to the ground state $R\,3\,c$ structure, which has shown remarkable structural flexibility in the context of heteroepitaxially grown BFO films [102].

5.3.2.1 Strain

Various experimental works have found the $R\,3\,c$ phase of BFO to be stable over a large range of epitaxial strain: from -2.6% to $+1.2\%$ [153–155]. In addition, spontaneous polarisation in BFO has been found to be relatively insensitive to epitaxial strain values of up to $\pm 3\%$ [149, 151]. Epitaxial strain can also be used to stabilise other phases of BFO, such as the tetragonal $P\,4\,m\,m$ phase, as summarised by Sando *et al.* [22, 102]. Since we are interested in the transformation from the $R\,3\,c$ to the $P\,m\,\bar{3}\,m$ phase, which involves a uniform change in lattice constants, we consider the case of uniform, rather than epitaxial strain. We apply uniform strains of between -5% to $+5\%$ to a BFO unit cell constrained to the $R\,3\,c$ symmetry. Fig. 5.5a shows the effect of such strain on the charge carrier effective masses.

The m_e^* changes significantly, decreasing from 3.02 m_0 in the unstrained cell, to 2.33 m_0 under 5% compressive strain. Under a tensile strain of between 1% and 3% we see an even larger decrease in m_e^*, from 3.19 m_0 to 0.60 m_0, corresponding to a change in the location and character of the CB_{min}. Figs. 5.5(b–d) show the projected bands and DOS for the -5, 0 and $+5\%$ strain cases. Similar figures for the other strain values are available in Fig. S2 of the SI [146]. From these figures a shift from an Fe t_{2g} to an Fe e_g dominated CB_{min} can be observed from 1% to 3% strain, which explains the sudden drop

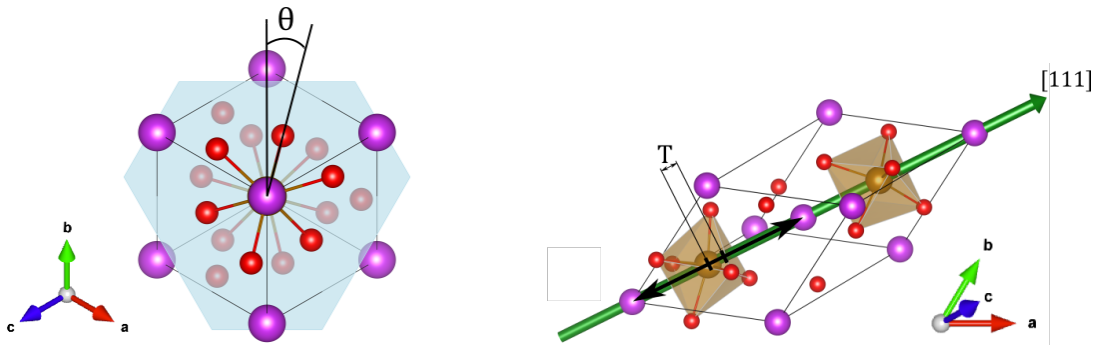

Figure 5.3: Schematic of the FeO_6 octahedral (a) rotations about, and (b) translations along the $[111]_{pc}$ direction present in the relaxed $R3c$ structure. In (a) we separate neighbouring octahedra along the $[111]_{pc}$ axis by a semi-transparent plane in order to highlight the out-of-phase nature of these rotations. The green arrow in (b) shows the $[111]_{pc}$ direction, and T is the displacement of the Fe atom from the mid-point between successive Bi atoms along this direction. Purple, ochre and red spheres represent Bi, Fe and O respectively.

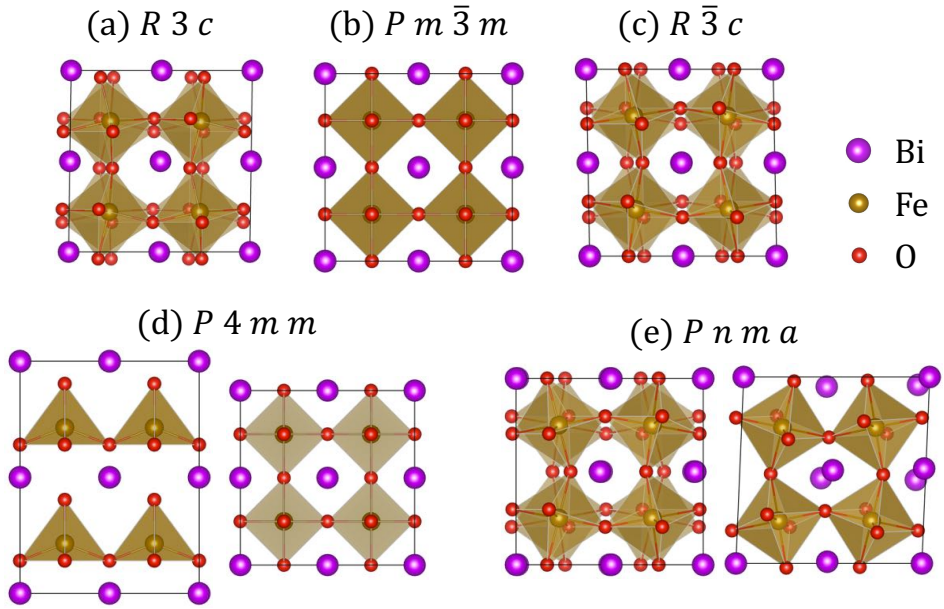

Figure 5.4: Crystal structures of five phases of BFO. For ease of comparison, all structures are presented in their cubic or pseudocubic settings. For the (a) $R3c$, (b) $R\bar{3}c$ and (c) $Pm\bar{3}m$ structures, the three pseudocubic axes are equivalent. The (d) $P4mm$ and (e) $Pnma$ structures however have one nonequivalent axis. For these structures the left (right) figure has the nonequivalent axis parallel (perpendicular) to the page. Note that in the (d) $P4mm$ case, the elongated cell causes the FeO_6 octahedra to break into square pyramidal FeO_5 units.

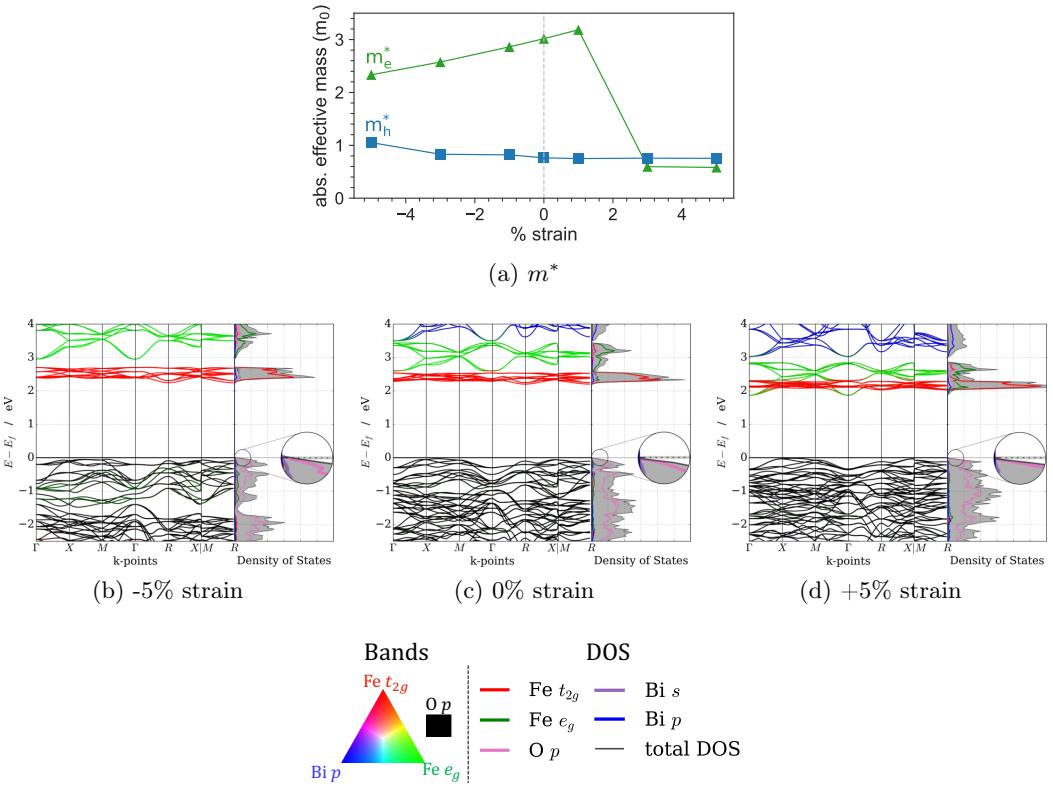

(a) m^*

(b) -5% strain (c) 0% strain (d) +5% strain

Figure 5.5: Effects of uniform strain on the (a) m_e^* (green triangles) and m_h^* (blue squares), and (b–d) projected bands and density of states. Note that while the DOS axis has arbitrary units here, the scale is the same in each subfigure. The bands are coloured, at each k-point, based on wavefunction projections onto chosen orbitals. As indicated in the legend in panel, red, green, blue and black represent projections onto Fe t_{2g}, Fe e_g, Bi p and O p states respectively.

in m_e^* for large tensile strain, since the e_g bands are more dispersive than the t_{2g} bands. We can understand the shift from a t_{2g} to an e_g dominated $\mathrm{CB_{min}}$ by considering the reduction in the splitting of the Fe d orbitals, due to the octahedral environment, as the Fe–O bond lengths increase. The m_h^* however, shows little dependence on strain. Over the range considered, $|m_h^*|$ is largest (1.051 m_0) at -5% strain, and smallest (0.753 m_0) at $+5\%$ strain. For all strain values considered, the $\mathrm{VB_{max}}$ remains strongly dominated by O p states as evident from Figs. 5.5(b–d). Thus, the negligible changes in m_h^* as the cell is strained are reflected by the minor changes in the character of the $\mathrm{VB_{max}}$.

5.3.2.2 Rotation of the FeO_6 octahedron

To examine the effect of octahedral rotation on the electronic properties of BFO, we rotate the FeO_6 octahedron from the perfect cubic perovskite geometry about the $[111]_{pc}$ axis in the out-of-phase manner shown in Fig. 5.3a. In Fig. 5.6 we plot the dependence of m^* on the rotation angle, θ. Both m_e^* and m_h^* increase with increasing θ. Around $\theta = 15°$ we see a marked increase in the gradient of this relationship.

To understand the trends in m^* with θ, we examine the electronic structures at

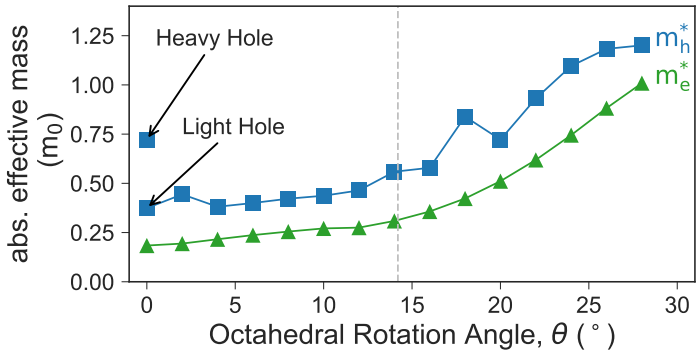

Figure 5.6: Absolute charge carrier effective mass versus octahedral rotation angle. The FeO_6 octahedra are rotated out-of-phase about the $[111]_{pc}$ axis. For each angle, θ, the m_h^* (blue squares) and m_e^* (green triangles) were calculated. Notice that in the perfect cubic structure ($\theta = 0°$), there is a band degeneracy at the top of the VB—hence the heavy and light holes. This degeneracy breaks as soon as we have any octahedral rotation. The rotation angle of the $R3c$ PBE+U relaxed structure ($\theta \approx 14.2°$) is indicated with a vertical dashed line.

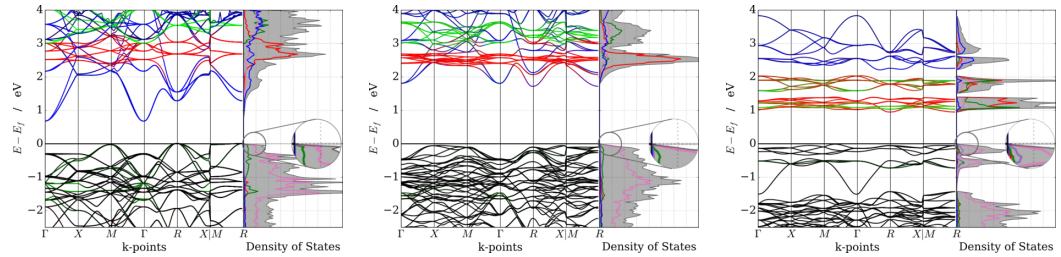

(a) $\theta = 0°$ (b) $\theta = 14°$ (c) $\theta = 28°$

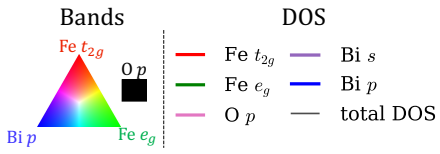

Figure 5.7: Variation in projected bands and density of states as a function of out-of-phase FeO_6 octahedral rotation about the $[111]_{pc}$ axis. Note that while the DOS axis has arbitrary units here, the scale is the same in each subfigure. The bands are coloured, at each k-point, based on wavefunction projections onto chosen orbitals. As indicated in the legend in panel, red, green, blue and black represent projections onto Fe t_{2g}, Fe e_g, Bi p and O p states respectively.

VB_{max} and CB_{min} as a function of θ. In Fig. 5.7 we plot the projected bands and DOS of BFO with the FeO_6 octahedron rotated at $\theta = 0°$, $\theta = 14°$ and $\theta = 28°$. Similar figures for the full range of θ considered can be found in Fig. S6 of the SI [146]. As θ increases up to $\theta = 14°$, the Bi p bands move up in energy but we see little change in the character of the CB_{min}, and correspondingly little change in m_e^*. Around 14° we see a shift in the location of the CB_{min} from Γ to R. For $\theta > 14°$, the character of the CB_{min} transitions from Bi p to Fe t_{2g}, and then to a possible[2] mix of Fe e_g and t_{2g} states for large θ. The Bi p to Fe t_{2g} transition is associated with the large increase in m_e^* with θ shown in Fig. 5.6.

Within the topmost valence bands, we find that O p states dominate for all values of θ considered. The states with minor contributions to the VB_{max} can be seen more clearly in the projected DOS. As θ increases, there is a decrease in the Fe e_g contribution and an increase in the Bi s contribution to the top of the VB. We therefore associate the increase in m_h^* with a decrease in Fe e_g contribution and an increase in Bi s contribution to the top of the valence band. Real-space plots of the KS orbitals as a function of θ can be found in Fig. S7 of the SI [146]. We also observe that for $\theta = 0°$, there is a band degeneracy at VB_{max}, and hence we present m_h^* values for both the heavy and light holes in Fig. 5.6. This degeneracy lifts as soon as we have any rotation.

5.3.2.3 Translation of the FeO_6 octahedron

We consider, independently, translations of distorted (rotated $\theta = 14°$ about the $[111]_{pc}$ axis) and perfect ($\theta = 0°$) FeO_6 octahedra along the $[111]_{pc}$ direction. The former translation is as illustrated in Fig. 5.3b. We find a marked difference between the two cases, as shown in Fig. 5.8 where we plot the dependence of m_e^* and m_h^* on the magnitude of the translation, T. Translating the perfect octahedron (Fig. 5.8a) has negligible effects on both m_e^* and m_h^*. Translating the distorted octahedron (Fig. 5.8b) also has little effect on m_h^*; however, there is a large effect on m_e^*.

Fig. 5.9 shows changes in the projected bands and DOS as the octahedra are translated. Once again we observe that changes in m^* are correlated with changes in the chemical character of the band extrema. Figs. 5.9 (a–c) confirm that the character at the CB_{min} of the structure with the perfect octahedron does not change within the range of T considered. Figs. 5.9 (d–f), however, show a shift from Bi p to Fe t_{2g} character in the case of the 14° rotated octahedron, corresponding to the substantial increase in m_e^*. Conversely, there is no change in character at the VB_{max}, and also little change in m_h^* with T, for both the perfect and the rotated octahedra. The VB_{max} degeneracy at $\theta = 0°$, that was lifted with octahedral rotations in Sec. 5.3.2.2, does not vanish in the

[2]Because we project the wavefunctions onto d orbitals defined with respect to the *global* Cartesian axes, the ability to resolve the difference between t_{2g} and e_g states diminishes as the local octahedral axes rotate relative to the global Cartesian axes. In other words, the 'mixing' of the t_{2g} and e_g manifolds may be an artefact of the way the projections are done. To unambiguously resolve the relative contributions of Fe t_{2g} and e_g states, one might perform a transformation from the global Cartesian basis to one that is local to each octahedron, as was done in Ref. 156. However, knowledge of the precise level of mixing between the Fe t_{2g} and e_g states goes beyond the requirements for the present study.

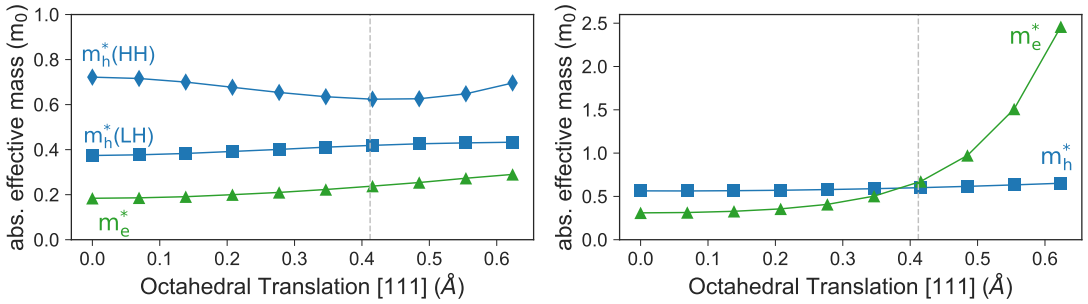

(a) $\theta = 0°$ (b) $\theta = 14°$

Figure 5.8: Absolute charge carrier effective mass versus $[111]_{pc}$ octahedral translation. In (a) we translate the perfect FeO_6 octahedron ($\theta = 0°$), while in (b) we translate a distorted octahedron ($\theta = 14°$). The angle, θ, is as defined in section 5.3.2.2. The m_e^* and m_h^* are represented by green triangles and blue squares respectively. In (a), the band degeneracy at VB_{max} gives rise to a heavy hole, HH (blue diamonds), in addition to the light hole, LH (blue squares). The vertical lines in each subfigure correspond to the PBE+U relaxed $R3c$ Fe translation along $[111]_{pc}$ (≈ 0.412 Å).

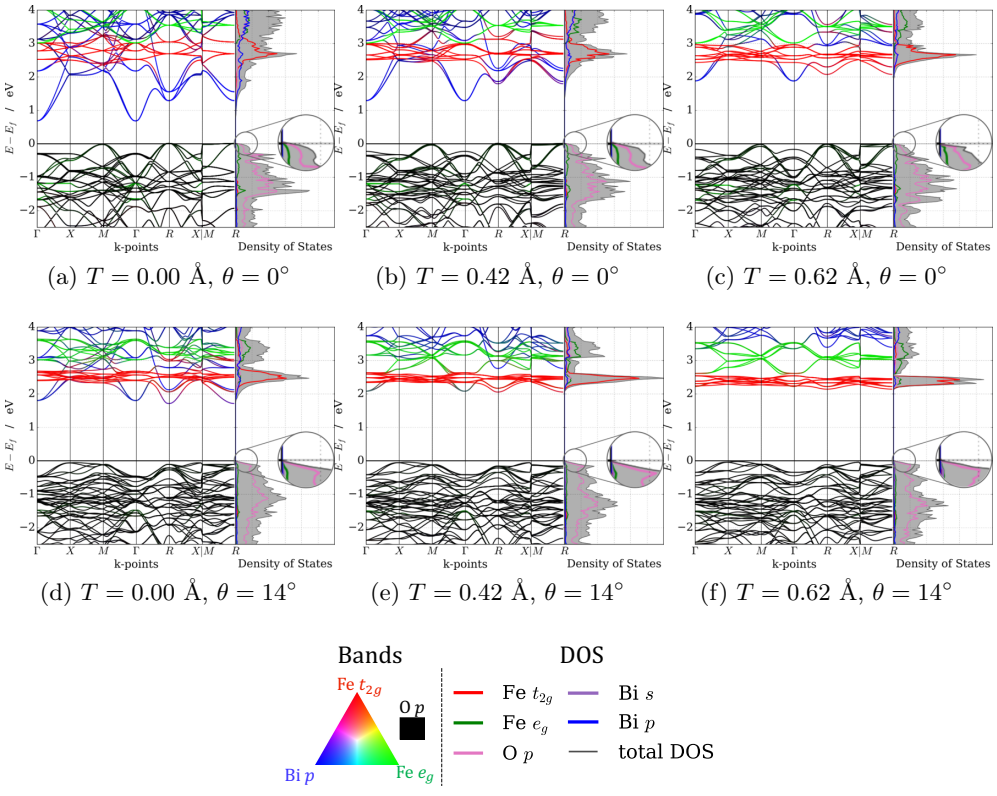

(a) $T = 0.00$ Å, $\theta = 0°$ (b) $T = 0.42$ Å, $\theta = 0°$ (c) $T = 0.62$ Å, $\theta = 0°$

(d) $T = 0.00$ Å, $\theta = 14°$ (e) $T = 0.42$ Å, $\theta = 14°$ (f) $T = 0.62$ Å, $\theta = 14°$

Figure 5.9: Variation in projected bands and density of states with FeO_6 octahedral translation along the $[111]_{pc}$ direction. $\theta = 0°$ and $\theta = 14°$ indicates the translation of the perfect (a–c) and distorted octahedra (d–f) respectively and T gives the translation magnitude. The bands are coloured based on projections onto chosen orbitals. As indicated in the legend, red, green, blue and black represent projections onto Fe t_{2g}, Fe e_g, Bi p and O p states respectively.

case of octahedral translations, as indicated in Figs. 5.9(a–c).

5.4 Discussion

In our investigations of the electronic properties in BFO, a clear link between the orbital characters at the band edges and the resulting m^* emerges. We find that presence of Fe e_g states at the VB_{max} and the Bi p states at the CB_{min} lead to relatively low m^*. At the VB_{max}, hybridisation between the Fe e_g and O $2p$ states leads to a more dispersive band and hence a lower m_h^*. In the conduction bands, the Bi p states are more dispersive than the Fe t_{2g}, and hence structures that have a CB_{min} that is dominated by Bi p states have a lower m_e^* than those whose CB_{min} is dominated by Fe t_{2g} states.

We have demonstrated that the changes in the band edge characters and hence m^* can be effected through geometric changes to the crystal structure. Extreme tensile strain, suppression of the octahedral rotation and suppression of the octahedral translation yield a much reduced m^* in BFO. This trend explains the variation in m^* across the BFO phases. The high m^* values of the $R3c$ and $Pnma$ phases can be attributed to the presence of octahedral rotation and translation in these phases. When we compare the $R3c$ and $R\bar{3}c$ structures, which contain similarly rotated octahedra, we find that the phase with the translated octahedron ($R3c$) has higher m^* values compared with the untranslated phase ($R\bar{3}c$). Interestingly, we find that when the rotation is completely suppressed ($\theta = 0$), translation of the octahedron (within the range of study) has little effect on m^*. Hence the $P4mm$ structure, which has translation without rotation, also has lower m^* values than those of $R3c$. The $Pm\bar{3}m$ structure has the lowest m^* values of all the structures considered since it has neither octahedral rotation or translation.

For applications in light harvesting, materials with low m^* values are required to allow the charge carriers to be transported to the electrode before the carriers recombine. Appreciable photovoltaic responses have already been recorded in BFO in the ground-state $R3c$ phase [16, 97, 98, 157, 158]. Our study indicates that its crystal structure may be modified to optimise m^*. Particularly in thin film heteroepitaxial growth, some degree of control over the octahedral tilt angle and tilt pattern has been demonstrated experimentally in BFO and other oxide systems [106, 107, 110, 159, 160]. While the high temperature $Pm\bar{3}m$ phase of BFO has the required geometric features to result in low m^*, it lacks the asymmetric potential required for the bulk photovoltaic effect. We find that the tetragonal $P4mm$ phase, which is experimentally accessible under compressive epitaxial strain, has both a large spontaneous polarisation and relatively low m^*. However, the $P4mm$ phase has been reported to have a larger optical gap than the $R3c$ phase, despite the smaller electronic gap, which would adversely affect the efficiency of the device [161]. While further work is required to elucidate these possibly competing effects, the $P4mm$ phase appears to be a promising PV candidate. Besides geometry manipulation, the band edge character can also be modified through chemical doping [104, 105], which may be an interesting subject for future work.

The effective masses obtained throughout this chapter correspond to those of pure bulk

BFO at 0 K. In real devices however, temperature, charge carrier doping concentrations, impurities, grain boundaries, polaronic effects and FE domain walls could all play important roles in determining m^* and hence μ. Some progress has been made towards including some of these factors in first-principles calculations, for example using semi-classical Boltzmann theory [162]. However, since our aim is to compare m^* between the BFO phases, and to suggest approaches to improve m^* further, we only consider *differences* in m^*. That is to say, while factors such as temperature are likely to affect m^*, we have made the assumption in this work that our 0 K results are a necessary precursor to including high temperature effects.

As noted in the previous chapter, the effect of spin-orbit coupling (SOC) has been found to be significant in describing certain properties of BFO, such as its weak (Dzyaloshinskii-Moriya) ferromagnetism [21]. We find a noticeable shift in the energy of the electronic bands and a small, Rashba-like shift in the location of the band edges. For example, the inclusion of SOC for the $R3c$ structure shifts the location of the CB_{min} slightly off the high-symmetry R point. Such a shift might improve the PV prospects of BFO by inhibiting charge carrier recombination. This Rashba effect, together with the effects of SOC on the m^* anisotropy, while beyond the scope of the present study, would be an interesting avenue for further investigation.

Despite the changes to the positions of the bands, the band curvatures around the Fermi level (and hence m^*) are largely unaffected by SOC. For the $R3c$ structure, we calculate the hole effective mass to be $-0.780\ m_0$ with SOC and $-0.669\ m_0$ without SOC. Similarly, the electron effective mass changed from $2.89\ m_0$ with SOC, to $3.06\ m_0$ without SOC. Note that in these comparisons we have kept constant the direction along which we evaluate m^*: $[-0.28366, 1.00000, -0.17603]$ for the hole mass and $[1, 1, 1]$ for the electron mass. These correspond to the principle directions that yield the lowest m^* in the non-SOC case; i.e. those that were used in Table 5.1 for $R3c$. Such differences are roughly an order of magnitude smaller than the differences in m^* that we found by comparing the various phases of BFO, and hence we neglect the effects of SOC throughout this work. Further tests of the effect of SOC on the character of bands as a function of octahedral rotations are available in Fig. S6 [146]. These tests indicate that, even in phases for which Bi p states dominate the CB_{min}, the effect of SOC on the curvature of the band edges is minimal. However, it would be interesting to further investigate the role of SOC in the $P4mm$ phase. In particular, the existence of a Rashba-like effect could further enhance the PV prospects of this tetragonal phase of BFO.

5.5 Conclusions

An important and often limiting factor in perovskite-based photovoltaics is their low charge carrier mobility. In this chapter we have employed first-principles methods to compare the charge carrier effective masses of both FE and non-FE phases of BFO and explore how the effective masses are influenced by changes in the crystal geometry.

We find that the ground-state, FE $R3c$ phase has relatively large m^* values compared to those of some non-FE phases. However, these non-FE phases lack the mechanism required for charge separation via the bulk photovoltaic effect. We therefore investigate the m^*-determining factors in BFO, with the aim of uncovering a FE phase with reduced m^* values. We discover that the differences in the m^* values are related to the orbital character at the band edges. BFO structures with Bi p or Fe e_g states, instead of Fe t_{2g} states, at the CB_{min} have lower m_e^* due to the localised nature of the t_{2g} bands. Structures with hybridised Fe e_g – O p states at the VB_{max}, rather than pure O p states, have lower m_h^* since the hybridisation leads to a more delocalised state. The change in the states at the CB_{min} leading to decreased m_e^* can be achieved with: (i) high tensile uniform strain, (ii) reduction of $[111]_{pc}$ translations of distorted FeO_6 octahedra, and (iii) a reduction in octahedral rotation about the $[111]_{pc}$ axis. The Fe e_g states emerges at the VB_{max} only with a reduction in octahedral rotations about $[111]_{pc}$.

These findings explain why the $Pm\bar{3}m$ phase, which has unrotated and untranslated octahedra, has the lowest m^* values of the BFO phases we have considered in this work. However, since we seek a FE phase and we find that m^* changes little with translation when the octahedral rotation about $[111]_{pc}$ is suppressed, then a structure resembling the tetragonal $P4mm$ phase would provide both ferroelectricity and reduced m^*. Our results demonstrate that manipulation of crystal geometry, which is easily achieved with advanced growth techniques, is a viable avenue to tune the electronic properties of materials particularly at the band edges.

6 | Two-dimensional electron gas formation at multiferroic interfaces

Abstract

The creation and characterisation of atomically sharp interfaces between different complex oxides has proven to be an exciting and fruitful area of research in recent years. Emergent properties of these interfaces, such as the two-dimensional electron gas (2DEG) at the $LaAlO_3/SrTiO_3$ interface, present novel opportunities for technological applications in addition to expanding our understanding of the fundamental physics and chemistry involved. In this chapter, we investigate the crystal and electronic structures of a series of $LaAlO_3/BiFeO_3$ superlattices (SL) using first principles simulations. We find that the thickness of the $BiFeO_3$ layer effectively allows one to tune (i) the tetragonality of the SL, (ii) the magnitude and direction of spontaneous polarisation and (iii) the electronic band gap of the SL. Above a critical thickness of around 6 $BiFeO_3$ unit cells, 2D electron and hole gases are predicted to form at opposing interfaces. The 2D gases form as a result of the spontaneous polarisation perpendicular to the interfaces. The ferroelectric origin of the gases, together with an emergent magnetism, suggests that this system holds promise as a source of novel multiferroic functionality. In particular, we suggest the possibility of switching the 2D electron and hole gases via an external electric field.

6.1 Introduction

In recent years, the growth and characterisation of atomically sharp interfaces between different complex oxides has proven to be an extremely fruitful area of research. In such heterostructures, the properties of the component oxides can combine and interact in useful ways. For example, materials consisting of alternating magnetic and ferroelectric components have been proposed as a source of novel multiferroic materials [163].

In addition to combining properties of the component oxides, heterostructures offer additional degrees of freedom (such as the relative thickness of the components) that can be exploited to further tune the properties of a material. For example, control over the octahedral tilts [107, 164, 165], magnetic anisotropy [160] and polarisation [110] has been demonstrated by varying the layer thickness and interface termination in complex

oxide heterostructures.

Finally, the interfaces themselves can exhibit intriguing emergent functionality. Perhaps the most well-known example of this is the formation of a two-dimensional electron gas (2DEG) at certain interfaces between $LaAlO_3$ (LAO) and $SrTiO_3$ (STO). The 2DEG at the LAO/STO interfaces has been found to possess some remarkable properties from superconductivity (even though both components are band insulators) to magnetism (even though both components are non-magnetic) [24, 25, 166, 167].

The ultimate origin of the 2DEG at the LAO/STO interface remains highly debated, despite well over a decade of intensive research. The most of the candidate explanations rely on the idea of a polar mismatch between LAO and STO. The idea is that STO has formally charge neutral layers (SrO and TiO_2) whilst LAO has formally[1] charged layers (LaO^+ and $AlO_2{}^-$). Therefore there is a discontinuity at the interface which is can be screened by the formation of a 2DEG. The main two proposed mechanisms for forming a 2DEG at LAO/STO interfaces are (i) electronic reconstruction, in which the 2DEG forms through an effective charge transfer from the top of the valence band to the bottom of the conduction band. (ii) Redox screening, in which redox reactions occur at the surface and resulting free carriers move to the interface to form the 2DEG. We should also note that imperfections at the interface (such as O vacancies) have also been proposed as explanations for the 2DEG formation. These typically do not rely on a polar discontinuity at the interface. We refer the reader to Ref.169 for a more detailed discussion of the various proposed mechanisms and also the ways in which theory may aid in adjudicating between them.

From a functional perspective, the 2DEG at the LAO/STO interface can be tuned during growth by, for example, diluting the LAO with STO [170] or by choosing an alternative interface orientation (e.g. (110) instead of the usual (100)) [171]. Once formed, the 2DEG can be further manipulated by various volatile and non-volatile means. An example of the former is the use of an applied electric field to tune the 2DEG density at the interface and thus use it as a transistor [172–174]. Non-volatile manipulation of the 2DEG can be achieved by growing a ferroelectric layer over the LAO. Switching the spontaneous polarisation in the ferroelectric layer has been found to greatly affect the charge transport properties of the 2DEG [175].

More recently, two-dimensional (2D) charge carrier gases have been proposed to form at interfaces between ferroelectric (FE) and non-FE materials [176, 177]. For example, either a 2DEG or 2D hole gas (2DHG) is predicted to form when lead titanate ($PbTiO_3$; PTO) films are grown on STO[2] [177]. This effect seems to be a direct result of the FE polarisation in PTO, with the direction of the polarisation determining whether a 2DEG or 2DHG forms. One of the enticing aspects of a FE-induced 2D charge carrier gas is the possibility of switching between a hole and electron gas at the interface via an

[1] Perovskites are well known to often have Born effective charges that differ substantially from their formal values. However, it has been shown that the formal charges are appropriate for the purposes of counting net interfacial charge in such systems. [168]

[2] A critical PTO film thickness is required before the 2DEG/2DHG emerges.

external electric field. A switchable 2DEG/2DHG opens up the possibility of being able to drastically alter the charge transport properties of the material *in situ*.

Some BFO-based heterostructures have also been found to form an interfacial 2DEG. The BFO/STO interface is a good example of this, though it seems that the 2DEG forms as a result of the polar discontinuity between BFO and STO (analogous to the LAO/STO case) rather than due to the spontaneous polarisation of BFO [178]. In addition, Chen *et al.* recently demonstrated that the diffusion of Ti cations to Fe sites also plays a role in the 2DEG formation in BFO/STO [179].

In this chapter we investigate LAO/BFO heterostructures motivated by a) by the prospects of a FE-induced 2D gas and b) the photovoltaic (PV) prospects of the tetragonal (T) phase of BFO (see Chapter 5). The combination of a wide-gap [180–184], non-FE material (LAO) and a FE material with a large spontaneous polarisation (BFO in the T phase [185–192]) provide the sorts of interface conditions under which one might expect the formation of a 2D charge carrier gas. Furthermore, because of the multiferroic nature of BFO, one might expect a 2D charge carrier gas in a BFO-based heterostructure to have interesting magnetic properties.

From the PV perspective, when BFO thin films are grown on LAO, the resulting compressive strain on BFO ($\approx 4.7\%$) favours either a tetragonal-like (T') or a mixed phase (with both rhombohedral (R) and T' regions) in BFO. The T' phase exhibits a giant polarisation [185–192] and, as we found in the previous chapter, low charge carrier effective masses. Persistent photoconductivity was also noted in T' thin-films by Bhatnagar *et al.* [193]. In mixed-phase thin films, an enhanced electromechanical response was found by Damodaran *et al.* [194]. Other properties of the T' and mixed-phase systems are summarised in the recent review by Sando *et al.* [22].

Having decided to investigate LAO/BFO, let us now discuss two possible heterostructure architectures for this system: thin films and superlattices. As mentioned above, the LAO/BFO system has been widely studied in the context of BFO thin films (these are reviewed extensively in Refs.102 and 22). However, there typically exists a critical film thickness one has to exceed in order to form a 2D charge carrier gas at the interface. Furthermore, for PV applications, thin films can be transparent. That is, they can be too thin to absorb sufficient incoming photons, thereby limiting device efficiency. Simply increasing the thickness of BFO films, however, is often not viable because of the large epitaxial strain imposed on BFO by LAO. If one continues to grow BFO layers on LAO, there comes a point at which the BFO relaxes to its bulk structure and dislocations form in order to accommodate the resulting lattice mismatch.[3]

An alternative architecture, and the one we adopt for this study, is that of the superlattice (SL). A SL is a crystalline structure in which the repeat unit contains two or more individual components. In our case, the SLs have a repeat unit that contains some number of LAO layers and some number of BFO layers. Two example repeat units are shown schematically in Fig.6.1. The SL architecture circumvents one difficulty of

[3]Recently it has been demonstrated, however, that by growing the films extremely slowly, which results in pockets of defects forming, T' films of BFO of > 70 nm can be stabilised on LAO [195].

thin films: SLs allow relatively tall structures to be grown coherently at a given strain. Moreover, at least in the case of the related PTO/STO system, SLs can be grown at lower temperatures than thin films [196]. A final advantage of the SL structure over that of the thin film is that, in principle, both a 2DEG and 2DHG could be supported simultaneously.

In this work, we construct a series of LAO/BFO SLs in which we keep the number of LAO layers fixed and vary the number of BFO layers in each repeat unit. We find that varying relative thickness of BFO provides a possible mechanism by which to tune the tetragonality, polarisation and electronic band gap of LAO/BFO SLs. Furthermore, we find that 2D electron and hole gases form at opposing interfaces for SLs above a critical thickness of BFO. The electronic and magnetic character of the 2DEG and 2DHG are of particular focus.

The rest of this chapter is organised as follows: in Section 6.2 we outline the assumptions and constraints used in constructing the SLs as well as detailing the computational methods employed here. In Section 6.3 we present and discuss the main results of this study, beginning with the effects of increasing BFO thickness on the crystal and electronic structure of the SLs. We then analyse in more detail the electronic and magnetic properties of the 2D electron and hole gases that form above a critical BFO thickness. We follow the results with a discussion of the caveats and limitations of the work in the context of the present literature. Finally, in Section 6.4, we summarise the key findings and make suggestions for future work.

6.2 Method

Here, we first outline the setup of the SLs to be investigated and later we describe the computational details of this work.

6.2.1 Building our superlattices

Two of the most basic degrees of freedom we have in our SLs are: the number of LAO layers (n), and the number of BFO layers (m) in the SL repeat unit. More precisely, n and m will refer to the number of AlO_2 and FeO_2 monolayers, respectively. In the present study, we are primarily interested in a) the possible formation of FE-induced 2D gases at the interface and b) the band characteristics of the BFO layer. We are therefore primarily interested in varying the thickness of BFO. Due to the computational demands of this system (discussed below) we limit ourselves to varying m and keeping the LAO thickness constant (to 2.5 pc unit cells in the out-of-plane direction).

A second crucial degree of freedom we have is the choice of interface termination. That is, a coherent interface between LAO and BFO can either consist of AlO_2/BiO, which we call the A-type, or of LaO/FeO_2, which we call the B-type interface. In this study we only consider symmetric SLs in which all of the interfaces are of the same type.

With the general setup that we have chosen in mind, let us consider the main

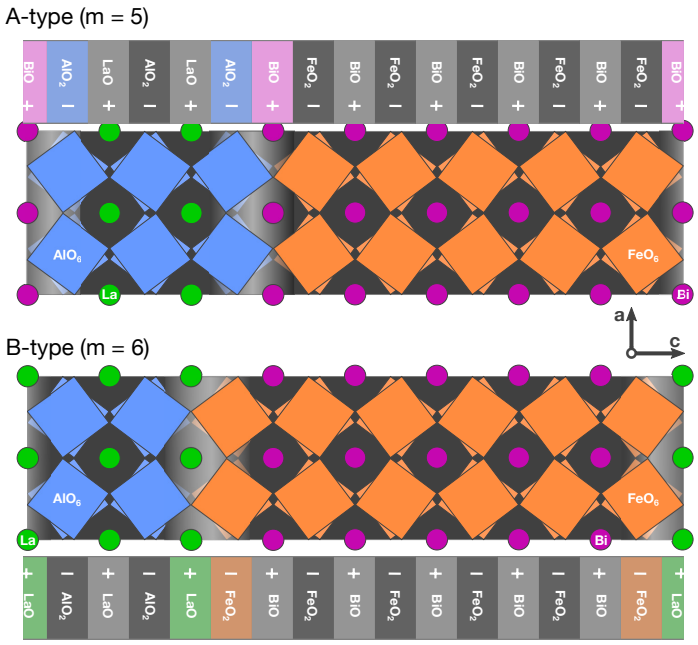

Figure 6.1: Schematic diagram comparing the A- and B-type superlattices for the cases of $m = 5$ and $m = 6$. m quantifies the number of layers of FeO_6 octahedra. The FeO_6 and AlO_6 octahedra are represented by orange and blue squares respectively. The O ions are located at the vertices of the octahedra. The circles represent Bi (purple) and La (green) ions. Notice that the interface layer in the A-type SL is composed of BiO/AlO_2 while that of the B-type is composed of LaO/FeO_2.

assumptions and constraints that were used to generate reasonable initial structures:

1. Because we envisage these SLs as growing on an LAO substrate, the first constraint we consider is that of fixing the in-plane lattice constants to bulk LAO values.[4] In order to improve the initial geometry, the isolated bulk BFO was first relaxed whilst constrained to the LAO in-plane unit cell and subsequently combined with LAO in the SL.

2. We assume a G-type antiferromagnetic (G-AFM) ordering in the Fe atoms. This is a good approximation of the magnetism in bulk $R3c$ BFO [197]. In the pure $P4mm$ phase, as discussed in Chapter 5, the C-type AFM is slightly lower in energy than the G-AFM ordering. However, we found this difference to be small (on the order of 2 meV per formula unit). Since the BFO, pre-relaxed to the LAO in-plane cell, lies somewhere between the $R3c$ and $P4mm$ phases, the G-AFM is a reasonable initial approximation. A consequence of assuming a G-AFM is that we require a pseudo-cubic (pc) 2×2 supercell parallel to the interface. A pc 2×2 supercell is also required by the octahedral rotation patterns in LAO and BFO, as discussed below.

3. The assumption of overall charge neutrality also puts constraints on possible

[4] These correspond to the DFT-relaxed values. See below for the full computational details.

structures. In particular, because LAO and BFO are both polar[5] materials, the total number of AO and BO_2 layers must be equal; i.e. the SL repeat unit must have an even number of monolayers overall. We refer the reader to Fig.6.1 for two examples of how to satisfy these constraints.

4. Both bulk LAO and bulk BFO have the $a^-a^-a^-$ octahedral rotation pattern in Glazer's notation [128]. We assume that the pattern in the phase of rotations is coherent across the LAO/BFO interface. That is, although the rotation angles differ between LAO and BFO, we assume that in going from one to the other, the pattern in the sign of the rotations is unchanged. Again we refer to the reader to Fig.6.1 for clarifying examples. This assumption requires the SL repeat unit to contain an even number of BO_2 monolayers (since there must be an even number of BO_6 octahedra in the out-of-plane direction). This requirement, combined with that of symmetric interfaces, imposes a distinction between odd and even m. That is, only the A-type SL satisfies the requirements for odd m, and only the B-type SL satisfies these for even m.

Importantly, we emphasise that these are *initial* constraints. As we discuss in Section 6.3.3, several of the constraints are violated during the course of the atomic relaxations, leading to several drastically different local minima. Before presenting resulting properties of the SLs thus generated, let us outline the details of the computations performed and discuss the computational challenges involved.

6.2.2 Computational details

The SLs described above pose challenges for DFT, many of which are shared with, and discussed at length in, previous chapters. In particular, the accurate description of strongly localised states such as those of the Fe d orbitals is challenging for semi-local DFT exchange-correlation (xc) functionals. In addition, in Chapter 5, we discussed the many competing low-energy phases of BFO and the strong effect of strain on the energy landscape. A shallow energy landscape poses problems for the various optimisation algorithms used here. Furthermore, because of the strong coupling between crystal and electronic degrees of freedom, very tight convergence criteria were required to find the minima—substantially increasing the cost of the calculations.

The over-delocalisation and shallow energy landscape problems are exacerbated by (i) the additional degrees of freedom in the SL structures (relative to the bulk materials), (ii) the strongly localised La f orbitals, and (iii) the increased size of the systems. The large[6] SL system sizes employed here are particularly problematic due to the $\mathcal{O}(\mathcal{N}^3)$ scaling of plane-wave DFT.

For the work presented in this chapter, we use DFT as implemented in VASP, version 5.4.4 [115–118]. The recent SCAN xc functional [75] has been found to very accurately

[5] That is, the pc AO layers have a formal charge of +1 and those of the BO_2 layers have a formal charge of −1.

[6] 'Large' is, of course, a relative term. The SL sizes we investigate are in the 90–200 atom range.

reproduce the crystal and electronic structures of BFO (see Chapter 4 and Ref.76). Our tests, which can be found in Appendix A.2, suggest that the SCAN functional also accurately captures important features of the crystal and electronic structures of LAO. In particular, we find that SCAN predicts the CBM to be primarily of La d character, in good agreement with the hybrid HSE06 functional and experiments [198]. By contrast, the PBE-GGA predicts the CBM to be of mixed La f and d character [198].

The calculations were carried out using the projector-augmented plane-wave method [95, 119] with a cut-off energy of 500 eV. The following electrons were treated as valence: Bi ($5d^{10}6s^26p^3$), Fe ($3p^63d^64s^2$), O ($2s^22p^4$), La ($5s^25p^65d^16s^2$) and Al ($3s^23p^1$). Brillouin zone integrations were performed on Γ-centred Monkhorst-Pack grids using the tetrahedron method with Blöchl corrections[7] [199]. For the ionic relaxations and static calculations, a $6 \times 6 \times N_z$ mesh was used, where N_z varies with the length of the unit cell in z. This corresponds to an in-plane k-point spacing of about 0.02 Å^{-1} and N_z was chosen such that the out-of-plane k-point spacing was less than 0.04 Å^{-1}. For density of states (DOS) calculations, the k-point grid was doubled in each direction. Note that for the $m = 6$ and $m = 7$ cases the band gap closes completely and a much finer k-point sampling was required as a result. We discuss these cases at length in section 6.3.2.

The ionic positions were relaxed such that the maximum force was less than 5 meV/Åand the unit cell was relaxed such that out-of-plane stress component was less than 0.07 GPa (again, the unit cell was fixed to that of bulk LAO in-plane). Initial relaxations of the $m = 3$ and $m = 5$ SLs forced these structures into what we later determined to be local minima. As we shall discuss in Section 6.3.3, this led to a systematic (though by no means exhaustive) exploration of alternative local minima with widely varying properties.

6.3 Results and Discussion

Having described the setup, we now present and discuss the key findings of this study. This discussion primarily concerns the lowest energy structures found for each m, with a discussion of competing polymorphs in Section 6.3.3.

6.3.1 Size effects

6.3.1.1 Tetragonality and polarisation

As discussed above, part of the motivation for studying the LAO/BFO system is the potential to stabilise a tetragonal or tetragonal-like phase of BFO. Let us therefore begin by examining the relaxed SL crystal structure as a function of BFO thickness. Specifically, we are interested in the tetragonality of the SL as a function of m. We capture this by the various c/a ratios shown in Fig.6.2.

[7] Note in cases for which the band gap closed, a Gaussian smearing approach was instead employed in order to get accurate forces during the ionic relaxations.

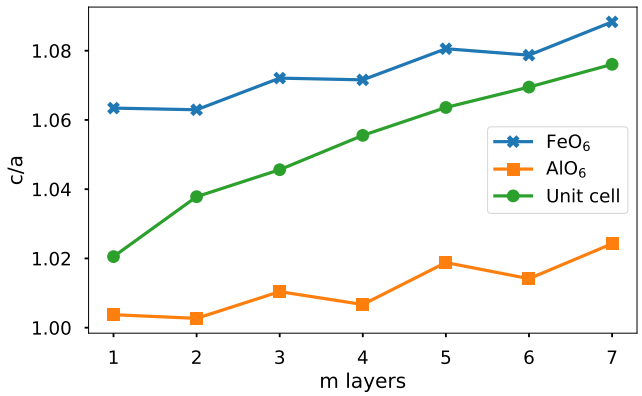

Figure 6.2: Measures of the tetragonality of a SL as a function of the BFO thickness, m. Distortions of the FeO_6 and AlO_6 octahedra are quantified by dividing the length of the apical O-O axis (roughly in the c-direction) by the average of those of the two equatorial O-O axes (roughly perpendicular to the c-direction). The unit cell c/a ratio given is simply the c/a ratio of the entire SL, normalised by the number unit cells.

We notice that the overall c/a ratio does indeed increase with m, as we would expect given the compressive in-plane strain imposed on BFO. However, the magnitudes of the c/a ratios here are still far below that of the $P4mm$ phase discussed in Chapter 5 (≈ 1.30). The trend in c/a ratio with m suggests that the unit cell tetragonality could be further increased for $m > 7$, though given the octahedral rotations discussed below, it is unlikely to reach that of pure $P4mm$ BFO.

Given the misalignment between the octahedral axes and those of the unit cell (due to octahedral tilting), we also examine the Jahn–Teller-like elongation of the FeO_6 and AlO_6 octahedra. These are shown in Fig.6.2. Unlike the overall c/a ratio, the elongation of the octahedra is not monotonic with m. Instead, the octahedral elongation seems to depend more on $n + m$, rather than m alone. That is, the pairs of m: $\{1, 2\}$, $\{3, 4\}$ and $\{5, 6\}$, have very similarly elongated octahedra. Recall that, because of the constraints discussed above, the total number of perovskite layers is given by $n + m$ and that $n = 3$ for odd m and $n = 2$ for even m. Thus, for example, in Fig.6.1 we saw how the $m = 5$ and $m = 6$ cases had the same number of octahedra in total (8).

In addition to the large c/a ratio, the pure $P4mm$ phase is characterised by having neither tilting nor rotation of the FeO_6 octahedra. In the SL structure, however, such an arrangement would likely be very unstable given the $a^-a^-a^-$ tilts in the LAO layers; indeed rotations/tilts are typically found experimentally [22]. We find that FeO_6 octahedra in our relaxed SLs are tilted and rotated with magnitudes comparable to those of $R3c$ BFO. The mean tilting (θ) and rotation (ϕ) angles, as defined in Ref.200, are shown in Fig.6.3. As can be seen, the mean angles do not vary significantly with m for $m \gtrsim 3$. A reduction in octahedral angles, suggested in Chapter 5 to be an important mechanism for the reduction of charge carrier mobilities in BFO, is therefore unlikely to be achieved by simply increasing m.

In general, the *range* of these angles across each SL (shaded regions of Fig.6.3)

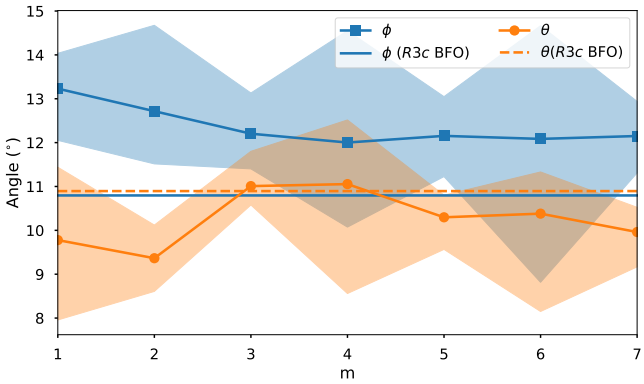

Figure 6.3: FeO_6 octahedral tilting (θ) and rotation (ϕ) angles as a function of m. θ and ϕ are as defined in Ref.[200]. The shaded regions represent the range of θ and ϕ across each SL, dominated by the angles of the interfacial octahedra.

appears to be smaller for the odd m than for even m. We can understand this by recalling that, for the A-type SLs (odd m), the interface is composed of BiO/AlO_2 layers and so in these cases the FeO_6 octahedra are shielded from the interface itself. In Fig.A.8 of Appendix A.5, we show that average angles are indeed brought down by the angles of the FeO_6 exactly at the interfaces, with little spatial dependence in the middle layers.

As the thickness of the BFO layer increases, we expect that the total polarisation of the SL should increase. Furthermore, given the increase in tetragonality discussed above, we also expect a rotation of the polarisation vector away from the initial $[111]_{pc}$ direction, towards the out-of-plane, $[001]_{pc}$ direction. In order to calculate the polarisation of the SL, as well as its spatial dependence, we use the Born effective charges (BEC) to estimate the local polarisation of each pc perovskite unit-cell, $\mathbf{P}_{local}$. This is done by identifying pseudo-cubic perovskite unit cells within the superlattice, overlaying a perfect cubic perovskite unit cell and computing the displacement of each site. We verified this method by computing the polarisation via the Berry phase approach for the $R3c$, $P4mm$, $Pnma$ and $Pm\bar{3}m$ phases of BFO and comparing these values to the estimates from the BECs. When identifying the perovskite units, one can choose between an A-site centred and a B-site centred unit cell; we compared the two centring choices and verified that these agree with each other.

Using the BEC method, we find that the magnitude and direction of the $\mathbf{P}_{local}$ estimates are, for the most part,[8] uniformly distributed within each component material. The distribution of $\mathbf{P}_{local}$ estimates across the SL are shown in Fig.A.7 in Appendix A.4 for each SL. We note that a substantial polarisation is induced in the LAO layers as a mechanism by which to minimise the interfacial depolarising field.

In Fig. 6.4, we show the components of the total SL polarisation, $\bar{\mathbf{P}}$, which is calculated as the mean of the polarisation of the individual pc perovskite units, plotted as a function of increasing BFO thickness. Note that, because the polarisation in BFO

[8]The case of $m = 1$ is somewhat of an exception here, as we might expect given how thin the BFO layer is.

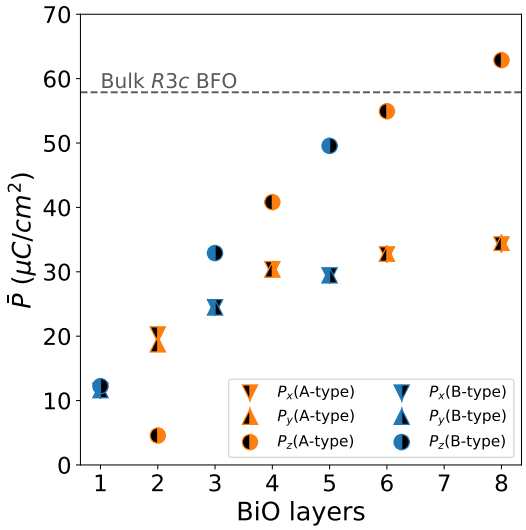

Figure 6.4: SL Polarisation, **P**, as a function of the number of BiO layers. P_x and P_y are the in-plane components and P_z is the out-of-plane component of **P**.

is driven by the Bi cations, in this figure we quantify the thickness of BFO in terms of the number of BiO monolayers,[9] rather than the number of FeO_2 monolayers, m. As expected, the magnitude of the polarisation increases and its direction rotates slightly out-of-plane as the BFO thickness is increased. This suggests a possible mechanism by which to tune the FE polarisation in LAO/BFO SLs.

6.3.1.2 Electronic structure

Let us now turn to electronic structure and to the effects that an increasing c/a ratio and $\bar{P}$ have on some key electronic properties. We begin with the electronic band gap, which is shown in Fig.6.5 plotted against m. We find that the band gap decreases rapidly with increasing m and, for $m \geq 6$, the gap closes entirely. The band gaps of the A- and B-type SLs show very similar behaviour, though the rate of decrease with m is slightly higher in the case of the B-type SLs. This slight difference becomes more apparent, and will be discussed further, in Section 6.3.2.

We can understand the decrease in gap with increasing m by considering the effect of polarisation on the band diagram of such a SL. In their 2009 paper, Bristowe *et al.* outline a simple capacitor-plates model of an LAO/STO superlattice, showing the effect of bound interfacial charge on the band diagram [201]. In that case, the interfacial charge arises out of a polar mismatch at the interface between LAO and STO. In the LAO/BFO superlattices we consider here, polarisation in the BFO layer also leads to bound interfacial charge and therefore a similar bending of the band diagram. We sketch such a diagram in Fig.6.5b. There we also sketch a band diagram for the case in which the polarisation in the BFO layer is zero (see for example the 'AFD' structure in Appendix A.6) and hence no band bending occurs. These two sketches illustrate how

[9] The number of BiO monolayers is given by $m + 1$ for the A-type, and $m - 1$ for the B-type SLs.

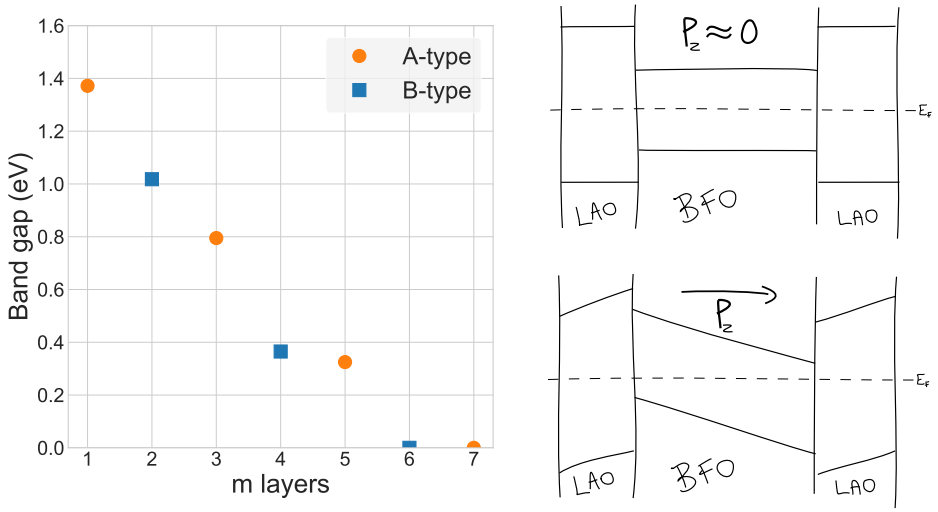

(a) (b)

Figure 6.5: (a) Electronic band gaps as a function of number of FeO_2 layers. The A- and B-type SLs are denoted by orange circles and blue squares respectively. Note that the band gap closes completely for $m \geq 6$. (b) Schematic band diagram explaining the decrease in band gap with m as a result of band tilting due to the out-of-plane polarisation.

a polarised BFO layer can affect the effective band gap of the SL. Note that simply increasing the thickness of the BFO layer would also result in a decreased band gap, even if the polarisation of each unit cell did not increase with thickness. That is, the dramatic decrease in band gap is attributable to *both* the increase in polarisation with m, and to the increase in BFO thickness itself.[10]

The band gaps were determined by computing the band structure along a path of high-symmetry.[11] We show three such spin-polarised band structures in Fig.6.6 for the $m = 2$, 4 and 6 cases. Band structures for the other cases can be found in Appendix A.3. The first point to note about these band structures is that, unlike bulk $R3c$ BFO, they all show a direct gap. This, coupled with the ability to tune the gap by varying m, suggests that the LAO/BFO SL architecture may be useful in optoelectronic applications. For the $m = 6$ case, we see that the gap closes completely, with the VBM and CBM overlapping at the $R_2(-1/2, -1/2, 1/2)$ and $V_2(1/2, -1/2, 0)$ points. We explore this interesting case in more detail in the following section.

We also note that the spin-up and spin-down bands appear, for the most part, identical. This is consistent with the AFM ordering. However, there does seem to be

[10] Note that if P_z were zero in BFO then increasing the thickness of BFO would not decrease the band gap.

[11] The path through k-space was determined using *seeK-path* and following the conventions of Ref.202.

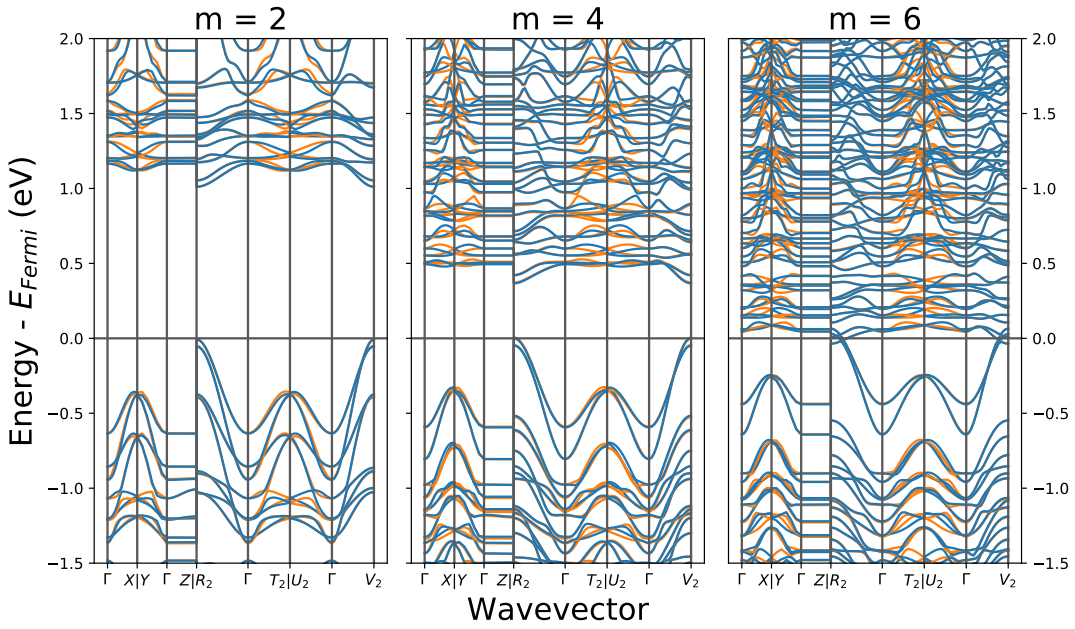

Figure 6.6: Electronic band structures for the $m = 2, 4$ and 6 cases. The colours represent the two spin channels.

an interesting spin asymmetry between the $\Gamma \to X$ and the $\Gamma \to Y$ paths. These two paths seem identical (as we might expect, given the symmetry of our system) apart from a reversal in the energy ordering of the two spin-channels. A similar spin asymmetry seems to exist in the related pair of paths: $\Gamma \to U_2(0, -1/2, 1/2)$ and $\Gamma \to T_2(-1/2, 0, 1/2)$.

There is a small amount of dispersion along $\Gamma \to Z$ for the $m = 2$ case and none at all for $m = 4$ and 6. This suggests that, for $m \geq 4$, the two interfaces present in each SL are effectively isolated from one another.

In Chapter 5, we emphasised the importance of the chemical character of the band edges on the effective mass of BFO. For the LAO/BFO superlattices studied here, the VBM is primarily composed of strongly hybridised Fe–O states, consistent with the relatively large amount of dispersion. The CBM, however, is made up almost solely of Fe states, consistent with less dispersive bands and hence a heavier electron. These characters can clearly be seen in the element-projected band structures and DOS plots in Fig.A.6.

6.3.2 Formation of 2DEG and 2DHG at opposite interfaces for $m \geq 6$

Let us now investigate in more detail the overlap between the VBM and CBM seen for the $m = 6$ SL. We can think of this overlap as resulting in an effective charge transfer from the VBM to the CBM. After this transfer, the newly occupied states of the CBM, localised to one interface, can be considered to be a 2DEG. At the opposite interface, the newly unoccupied states at the VBM can now be considered to be a 2DHG. We illustrate this with Fig.6.7 in which we sketch a possible band diagram showing the band overlap and the resulting 2DEG/2DHG.

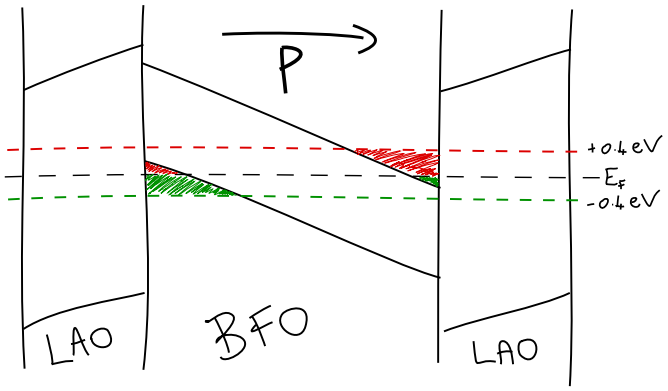

Figure 6.7: Schematic band diagram showing the origin of the 2D free carrier gases in the $m \geq 6$ cases. The green shaded region indicates the occupied states in the energy window from 0.4 eV below the Fermi level, up to the Fermi level. The red shaded region indicates the unoccupied states between the Fermi level and 0.4 eV above it. The red region at the left interface can be considered to be a 2DHG and the green region at the right interface can be considered a 2DEG.

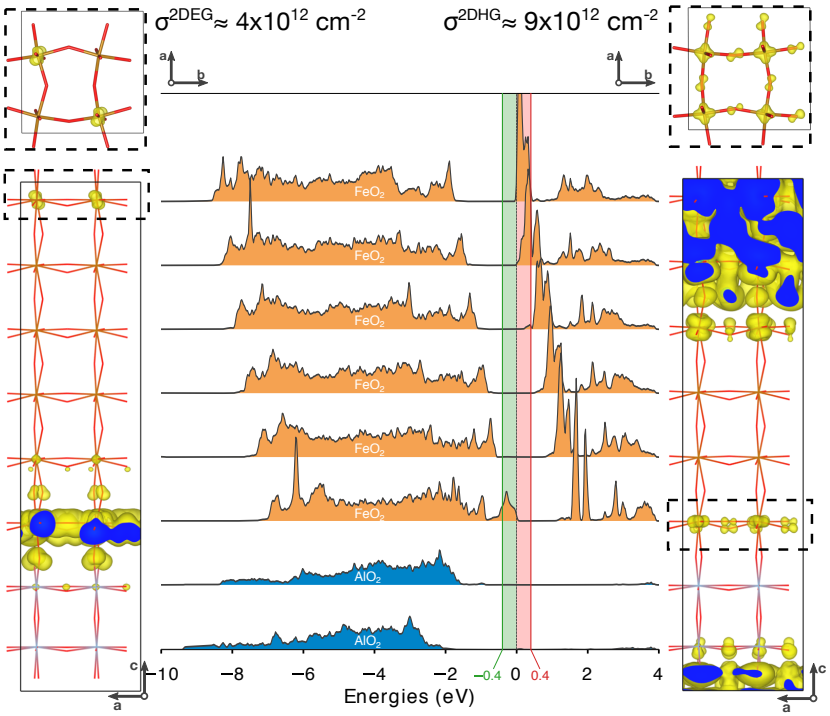

Figure 6.8: Density of states projected onto FeO_2 (orange) and AlO_2 (blue) layers for the $m = 6$ SL. The green and red shaded regions show the energy windows used to extract the highest occupied (left) and lowest unoccupied KS orbitals (right), respectively. For clarity, only the Al-O and Fe-O bonds are depicted in the KS orbital plots. The KS isosurfaces are plotted at a value of 5×10^{-4} $e/bohr^3$. The dashed rectangles indicate the free carrier gas regions; these are shown also at the top of the figure with the interface parallel to the page.

The band tilting of Fig.6.7 manifests itself in the layer-projected DOS, as shown in Fig.6.8. There we also plot the Kohn-Sham (KS) orbitals, which correspond to charge density contributions, from the states around the Fermi level. These indicate that the 2DEG is primarily Fe t_{2g} in character,[12] while the 2DHG is a hybridisation of Fe e_g and O p states. It is likely, therefore, that the transport characteristics of the hole and electron gases would differ substantially. Further investigation of the transport characteristics of these 2D gases, while beyond the scope of the present study, would be of considerable interest for potential applications.

In order to quantify the amount of free charge per unit area, σ, in our electron and hole gases, we follow the approach of Yin *et al.* [177]. In brief, the method involves calculating partial charge densities corresponding to a certain energy window (in our case this was -0.4 eV to E_F for the 2DEG and E_F to 0.4 eV for the 2DHG).[13] We then examine these partial charge densities in real-space and integrate the isolated electron and hole gas regions (the dotted rectangles in Fig.6.8). We find that, for $m = 6$, $\sigma^{2DEG} = 4.13 \times 10^{12} cm^{-2} = 0.66 \mu C\, cm^{-2}$ and $\sigma^{2DHG} = 9.46 \times 10^{12} cm^{-2} = 1.51 \mu C\, cm^{-2}$. While these are significant amounts of charge, they are much too small to completely screen the bulk polarisation ($\bar{P}_z \approx 49.6 \mu C\, cm^{-2}$) of the SL.

One might expect the magnitude of charge in the 2DEG and 2DHG to be exactly equal, if the 2D charge carrier gases are formed via an effective charge transfer. The above estimates suggest that in this case, however, there is roughly twice as much charge in the hole gas as there is in the electron gas. We are not certain as to why this is so, though in Fig.6.9 we show that these gases are localised to different extents in k-space. That is, the discrepancy may be a result of finite sampling. Indeed, using a Γ-centred $6 \times 6 \times 1$ mesh, we were unable to find the 2DEG at all. The values we present are based on a fully self-consistent calculation using a Γ-centred $16 \times 16 \times 1$ mesh.

Interestingly, the band structure for $m = 7$ SL shows less overlap between the VBM and CBM than the $m = 6$ SL (see Fig.A.5 of Appendix A.3), despite having a larger P_z and a thicker BFO layer. This is in keeping with the trend in band gaps identified earlier, namely that the A-type SLs have a slightly slower rate of decrease with increasing m than do the B-type SLs. One possible reason for this could be that the FeO_6 octahedra (whose states dominate the VBM and CBM) are more shielded from the interface in the A-type SLs than the B-type SLs.

As discussed in the previous section, the LAO/BFO SLs presented here have a direct band gap. The 2DEG and 2DHG of the $m = 6$ SL, therefore, form at the same region of k-space. By contrast, many other 2D gas forming heterostructures (e.g. LAO/STO [201], PTO/STO [177] and $PbZr_{0.2}Ti_{0.8}O_3$ /STO [203]) have an indirect gap. In Fig.6.9, we map out the contributions to the 2DEG and 2DHG from across the irreducible Brillouin zone (IBZ). This shows that both gases are strongly localised within the $(1/2, 1/2)$ pockets

[12] As found in Chapter 5, large octahedral rotation angles are found to favour an Fe t_{2g} over a Bi p character at the CBM. This is consistent with the large octahedral angles found in this SL.

[13] These energy windows were chosen based on the band structures. That is, large enough to include all of the contributions to the 2D gas, but not so large as to be unable to isolate the 2D gas in real-space.

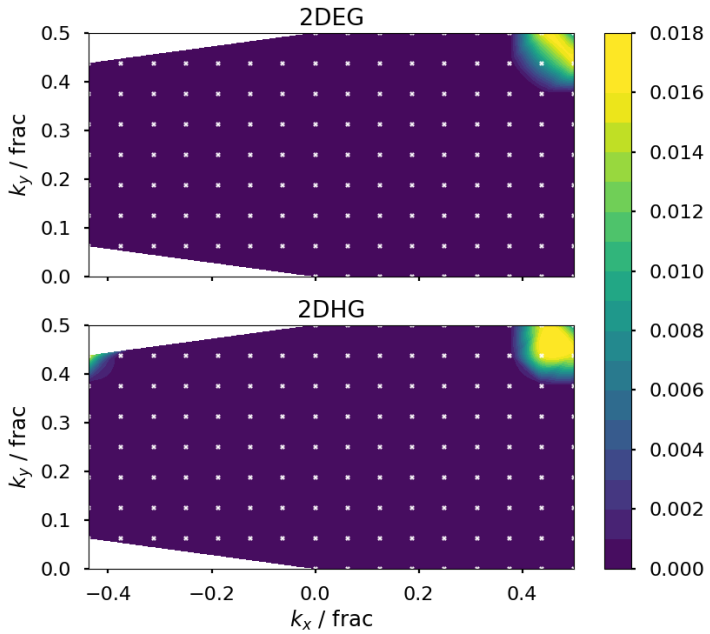

Figure 6.9: Reciprocal-space map of the contributions to the 2DEG and 2DHG from different k-points. The small white markers represent the irreducible Brillouin zone (IBZ) points corresponding to a Γ-centred 16×16 k-point grid. The slices shown are taken at $k_z = 0$. The colourbar indicates, in units of e, the magnitude of the charge contributions from the region around each k-point, according to a cubic-interpolation scheme.

of the IBZ, though they are localised to slightly different degrees. We again note the requirement of an extremely fine sampling of the IBZ in this case.

Finally, given the multiferroic nature of BFO, and also the ferromagnetism discovered at the LAO/STO interface, let us now consider the magnetism of the 2D gases in LAO/BFO. In Fig.6.10 we plot the spin-density of the 2DEG and 2DHG for $m = 6$. Two important points emerge from this figure: (i) both the 2DEG and 2DHG are well-localised in the z direction. (ii) A clear asymmetry exists between the spin-up and spin-down density for both the 2DEG and 2DHG. Since the 2D gases form as a consequence of the electric polarisation in this SL, it may be the case that an external electric field could be used to switch not only the electric polarisation, but also the spin-orientation of the 2D gases. That is, the electric field control of magnetism may be possible in this SL.

6.3.3 General discussion and caveats

While our results indicate that the LAO/BFO SLs host a rich variety of interesting properties, several open questions remain. The first question concerns the well-known underestimation of band gaps using semi-local xc functionals. In addition to predicting incorrect band gaps, this failure can lead to spurious effects in such complex oxide heterostructures. For example, in metal-FE heterostructures the band gap underestimation can manifest itself through a pathological charge spill-out [204].

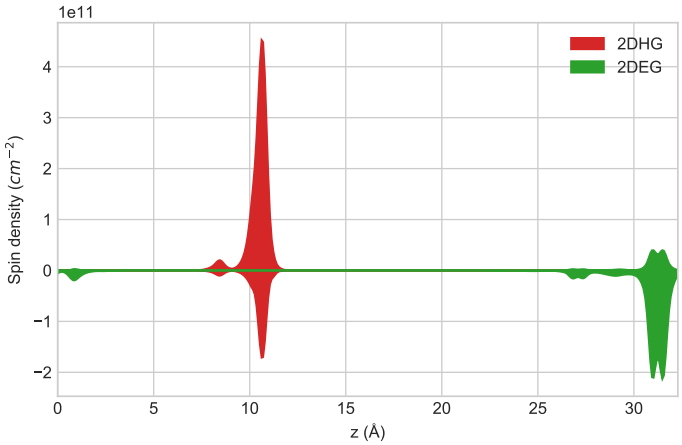

Figure 6.10: Planar-averaged spin density contributions from the 2DEG (green) and 2DHG (red).

We partially address this question by using the SCAN functional. As we saw in Chapter 4 and in Ref.76, SCAN more accurately predicts the crystal and electronic structures of BFO than the PBE or LDA functionals. Perhaps more importantly, although SCAN still underestimates the band gap of BFO, the identified *trend* in band gap with increasing BFO thickness is likely to be a robust finding. That is, a 2DEG/2DHG would still form in this system, even if the specific critical thickness for the formation of the 2D gases ($m = 6$) may be underestimated.

A second, and more challenging question to address is that of alternative low-energy structures that may form instead of those considered above. BFO-based superlattices can, as in bulk BFO, exist in multiple low-energy phases. Indeed, the initial relaxations of the A-type SLs led to structures that we subsequently found to be local minima. By perturbing the initial structures and re-relaxing, three different low-energy polymorphs were constructed for the A-type SLs. Representative results for the $m = 5$ can be found in Appendix A.6. The polymorphs we tested had dramatically different polarisation patterns, band structures and octahedral rotation patterns. The differences in total energy between these polymorphs were, however, relatively small (∼4 meV/atom). The existence of multiple low-energy structures may pose challenges for an exact experimental verification of our earlier predictions. On the other hand, as in BFO thin films, the exact SL growth conditions may be optimised so as to favour a particular low-energy structure and thus to tune the properties of the resulting SL.

Finally, one may wonder about the legitimacy of the assumption, implicit throughout, of a single FE domain. We know that a competing mechanism by which the depolarising field can be reduced is the formation of FE domains. In FE (and ferromagnetic) thin-films, the Kittel Law (KL) often applies. According to this, the width of domains, w, is proportional to the square-root of the film thickness, t [205]. A 2010 theoretical study found that BFO does indeed follow the KL, though for slightly different reasons than for most materials [206]. According this study, BFO (001) thin films with 71° FE domains

and a 1.5% compressive epitaxial strain were found to obey the KL down to about 5 unit cells thick (≈ 20 Å). Whether or not the KL law applies in the LAO/BFO superlattice architecture would certainly be an interesting avenue for future work. Because of the crucial role octahedral rotations were found to play in the KL in BFO [206], it may be the case that the LAO/BFO interfaces give rise to a qualitatively different behaviour. The applicability of the KL to LAO/BFO SLs, as well as the role of FE domains in these systems more generally, would therefore be interesting questions to explore in future studies.

6.4 Conclusions

We have investigated the effects of BFO layer thickness on the structural and electronic properties of LAO/BFO SLs. As one increases the BFO thickness, keeping the LAO thickness constant, we find the following: (i) an increased tetragonality of the SLs, (ii) an increase in $|\bar{\mathbf{P}}|$ and a rotation of $\bar{\mathbf{P}}$ towards the direction perpendicular to the interfaces. (iii) The band gap of the SLs is direct and decreases sharply with BFO thickness, due to the out-of-plane polarisation component. This suggests a mechanism by which to tune the electronic band gap of the SL. (iv) Above a critical thickness ($m = 6$), the formation of 2D electron and hole gases, each with a net spin. The 2D free carrier gases form due to the out-of-plane polarisation component which suggests the enticing possibility of a switchable ferromagnetic 2DEG/2DHG.

We therefore encourage attempts towards the experimental realisation of the proposed LAO/BFO SLs. In addition, we suggest that further theoretical work to elucidate the nature of the proposed 2DEG/2DHG may be fruitful.

7 | Conclusions and outlook

Ferroelectric perovskites in general, and BFO in particular, offer a seemingly endless supply of opportunities to learn subtle lessons in the physics and chemistry of materials. At the same time, these fascinating materials form the basis for vast improvements in existing technologies as well as holding the keys to a range of completely new ones.

In this final chapter we look back, summarising our key findings; we also look forward, reflecting on how these results fit into the broader understanding of materials and offering specific suggestions for future work.

In Chapter 4, we saw how the simple Hubbard-like correction to DFT (DFT+U) could be used to improve the predictions of certain properties of complex oxides such as BFO. We conducted a systematic investigation of the effects of the U parameter (as applied to the Fe d orbitals) on the crystal and electronic structures of bulk BFO. Because of their role in determining optoelectronic properties, we focussed on the natures of the conduction band minimum (CBM) and valence band maximum (VBM). We found dramatic changes to the location and curvature of the CBM in particular, which we traced to a change in the character of the CBM. Specifically, we found an inversion in the ordering of the Fe t_{2g} and e_g manifolds at the CBM when U exceeded 4 eV (for PBE+U). While we cannot say for certain whether the CBM is composed of Fe t_{2g} or e_g states, simple crystal field arguments suggest that it should be the former. We therefore recommend a U value of at most 4 eV to be applied to the Fe d orbitals in BFO (within PBE+U). More generally, this study emphasises the need for systematic investigations of the effects of the U parameter on the electronic structure as a whole (not merely on band gaps), especially in cases for which the character and curvature of band edges is of importance.

In Chapter 5, motivated by the PV prospects of BFO, we investigated the influence of crystal structure on effective mass of charge carriers. We began by comparing the effective masses of several known phases of BFO, finding orders of magnitude differences between them. The strain-induced tetragonal (T) phase emerged from this comparison as having the promising combination of a large spontaneous polarisation and relatively light charge carriers. In order to gain insight into the variation of effective masses across these phases, we systematically investigated those structural transformations that map the phase with the heaviest charge carriers to that with the lightest charge carriers. Specifically, we examined the effects of uniform strain, and translations and rotations of FeO_6 octahedra on the effective masses. We found that electron effective masses were

particularly sensitive to structural changes which we discussed in terms of changes to the orbital character of the CBM.

Emerging from the above investigations is a set of structural mechanisms by which to tune effective masses in BFO. Many of the specific recommendations (e.g. minimising octahedral rotations) would likely apply to related materials directly. More generally, the mode-decomposition approach employed here could be applied to other materials as well as other properties. In terms of PV applications, effective mass is just one of the many important factors that ultimately determine the efficiency of a device. For example, charge carrier mobilities depend on carrier lifetimes, in addition to their effective masses. Further work is therefore needed in order to determine the role that structural factors have in determining these other key properties.

In Chapter 6, we ventured beyond the bulk, exploring heterostructures of LAO and BFO. Our aims were twofold: (i) to stabilise a T-like phase in BFO and (ii) to investigate emergent interface effects. Specifically, we modelled LAO/BFO superlattices (SL) from first principles. By simply varying the thickness of the BFO layer, we found that one could tune the tetragonality, spontaneous polarisation and band gap of the SLs. Above a critical thickness (around 6 unit cells of BFO), two-dimensional electron and hole gases were found to form at the interfaces. We further investigated the properties of the emergent 2DEG/2DHG, quantifying the amount of charge in them and finding each to have a net spin. Given the magnetic character of these 2D gases and that the driving force behind their formation is the spontaneous electric polarisation, this system may be useful in a range of novel multiferroic applications. However, this work has some important caveats that could possibly hamper the experimental realisation of these 2D gases and their application. For example, competing mechanisms by which to screen the depolarising field, such as ferroelectric domain formation, could be more favourable than the monodomain structure considered here. Therefore, while the results of this study suggest that LAO/BFO superlattices could form the basis of exciting new technologies, a good deal of further work is needed before this potential is realised.

A | Appendix

A.1 DFT parameter convergence tests

In Fig. A.1 we plot PBE+U (U_{eff}= 4 eV) results of tests for convergence with respect to basis set size and Brillouin zone sampling. This was done by relaxing the internal coordinates of the BFO $R3c$ structure at a series of fixed unit cell volumes around the equilibrium volume at a range of plane-wave energy cut-offs and k-point densities. The Birch-Murnaghan (BM) equation of state [207] was then fitted to each of the resulting volume–energy datasets. In Fig. A.1 we plot the volume–energy curves and the fitted BM parameters, namely, the bulk modulus and the minimum in volume (V_0) as a function of plane-wave cut-off and k-point mesh. These indicate that, at a plane-wave cut-off energy of 500 eV, the bulk modulus is converged to within 0.3 GPa and the equilibrium volume is converged to within 0.03 Å^3 per f.u. At a Γ-centred $6 \times 6 \times 6$ Monkhorst-Pack mesh for the 10-atom cell, the predicted bulk modulus is converged to within 0.005 GPa and the equilibrium volume is converged to within 6×10^{-4} Å^3 per f.u.

In Fig.A.2 we plot the results of further tests for the convergence of forces with respect to basis set size and k-point sampling. For this, we perform static, self-consistent calculations of the experimental $R3c$ structure of BFO at a series of plane-wave cut-offs and k-point meshes. The maximum force on any atom is converged to within 7 meV/Å at a 500 eV plane-wave cut-off energy. At a Γ-centred $6 \times 6 \times 6$ k-point mesh, the maximum force on any atom differs by just 0.1 meV/Å with respect to that from the $14 \times 14 \times 14$ mesh.

A.2 Crystal and electronic properties of $LaAlO_3$ with the SCAN functional

Recent work by Shen *et al.* finds that the PBE GGA fails to accurately predict the orbital character of the conduction band minimum (CBM) of $LaAlO_3$ (LAO) [198]. In this appendix, we investigate the orbital character of the CBM as predicted by the SCAN functional. In addition, we report its predicted crystal structure parameters in Table A.1, finding good agreement with experimental values.

If Fig.A.3, we plot the LAO band structure, computed with the SCAN functional. In agreement with the HSE06 screened hybrid functional, we find that the CBM is

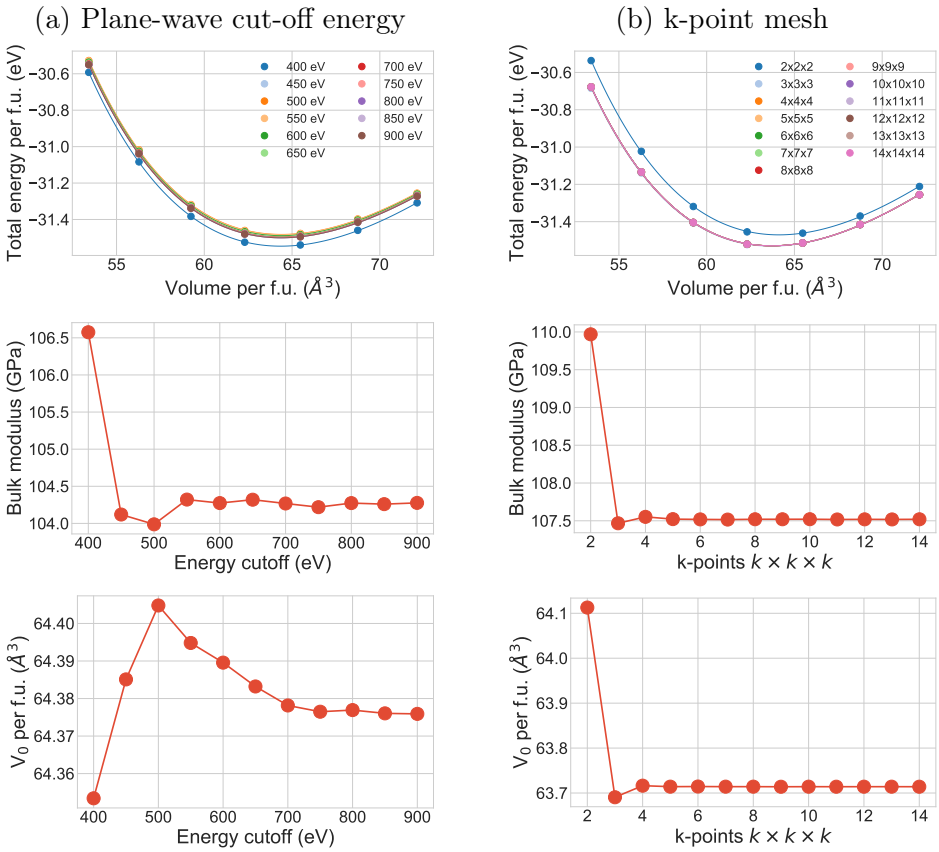

Figure A.1: Convergence of $R3c$ BFO volume-energy curves with respect to plane-wave cut-off and k-point sampling. This is done with the PBE+U (U_{eff} = 4 eV) xc functional.

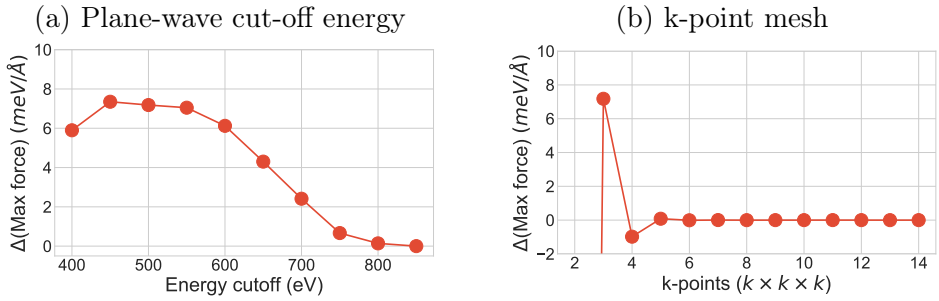

Figure A.2: Convergence of the maximum force in the experimental $R3c$ BFO [121] with respect to (a) plane-wave cut-off energy and (b) k-point sampling. These calculations are performed using the PBE+U (U_{eff} = 4 eV) xc functional.

Table A.1: Structural parameters of *R*3*c* LAO as predicted by the SCAN functional, compared to those values reported in the literature. We compare the lattice constant, a, the rhombohedral unit cell angle, α and the octahedral tilt angle, θ as defined in Ref. 198.

Property	SCAN	PBE	PBE	PBE	HSE06	HSE06	Exp.
a (Å)	5.347	5.392	5.346	5.422	5.342	5.381	5.357
α (°)	60.13	60.22	60.30	60.31	60.20	60.20	60.10
θ (°)	5.3	6.3		4.0	5.7	3.1	5.7
Ref.	Present work	[198]	[208]	[209]	[198]	[209]	[210]

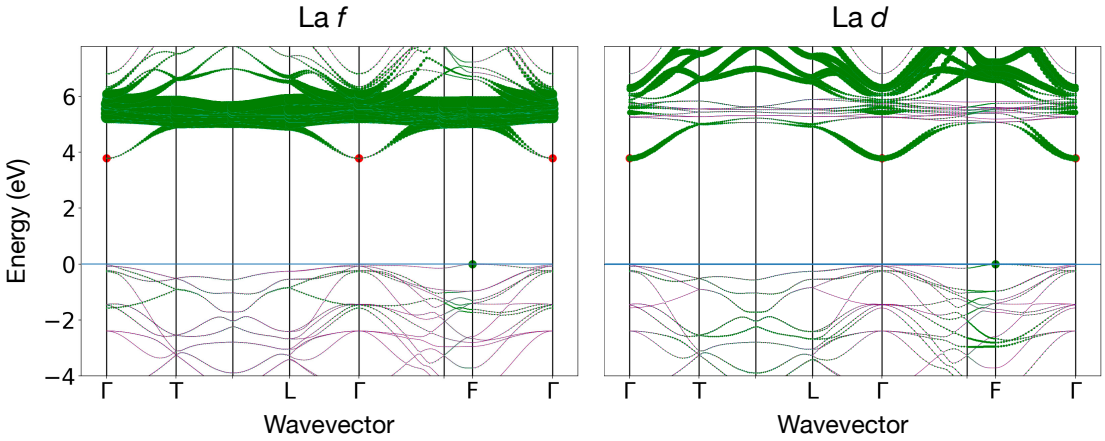

Figure A.3: Band structure for *R*3*c* LAO. The size of the green markers correspond to projections onto La f (left) and La d (right) states. The valence band maximum and conduction band minimum are marked with circles. The figure was produced with pymatgen [211].

composed primarily of La d states.

A.3 Band structures for all LAO/BFO superlattices

The electronic band structures for the range of m tested in Chapter 6 are shown here in Fig.A.4. We additionally plot the band structures for the $m = 6$ and $m = 7$, zoomed into the region around the Fermi level in Fig.A.5. In Fig.A.6 we plot the projected band structures and densities of states (DOS), showing the elemental contributions in each case. These plots indicate that the VBM in each case is primarily composed of a Fe-O hybridised state and the CBM is primarily composed of Fe states.

A.4 Local polarisation maps in LAO/BFO superlattices

For each of the superlattices, we compute the local polarisation of all the component pseudo-cubic perovskite unit cells. In Fig.A.7 we plot the components of these local polarisation vectors as a function of position in the unit cell.

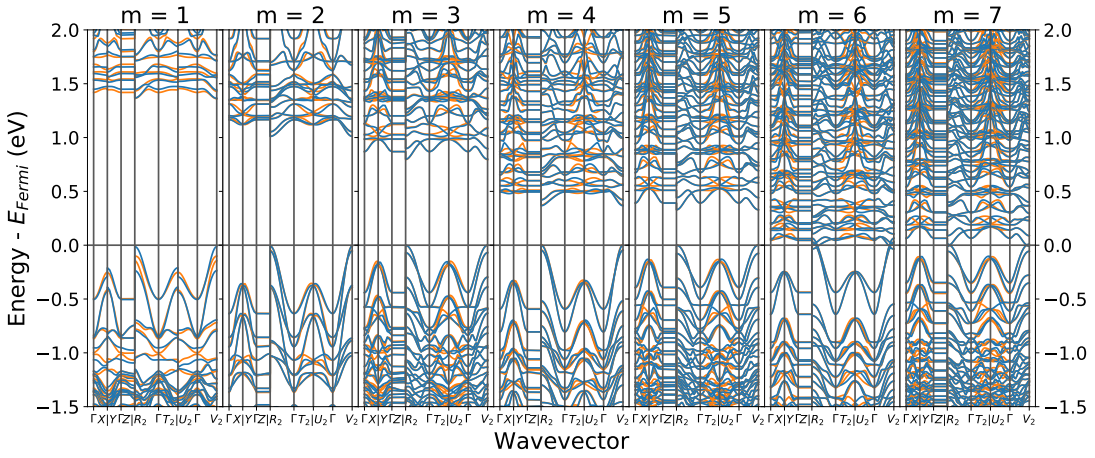

Figure A.4: Electronic band structures for the increasing BFO thickness, in LAO/BFO superlattices. The colours correspond to the different spin channels.

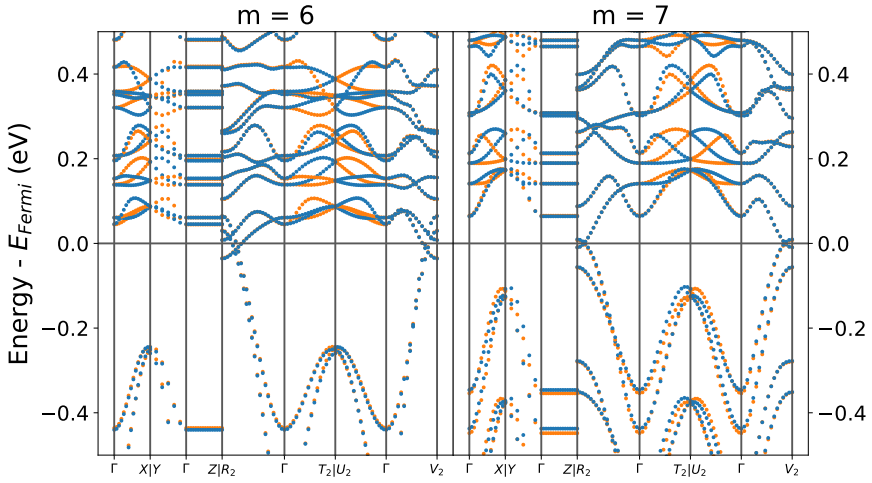

Figure A.5: Electronic band structures for $m = 6$ and $m = 7$ superlattices, focussing on the region around the Fermi level. The colours correspond to the different spin channels.

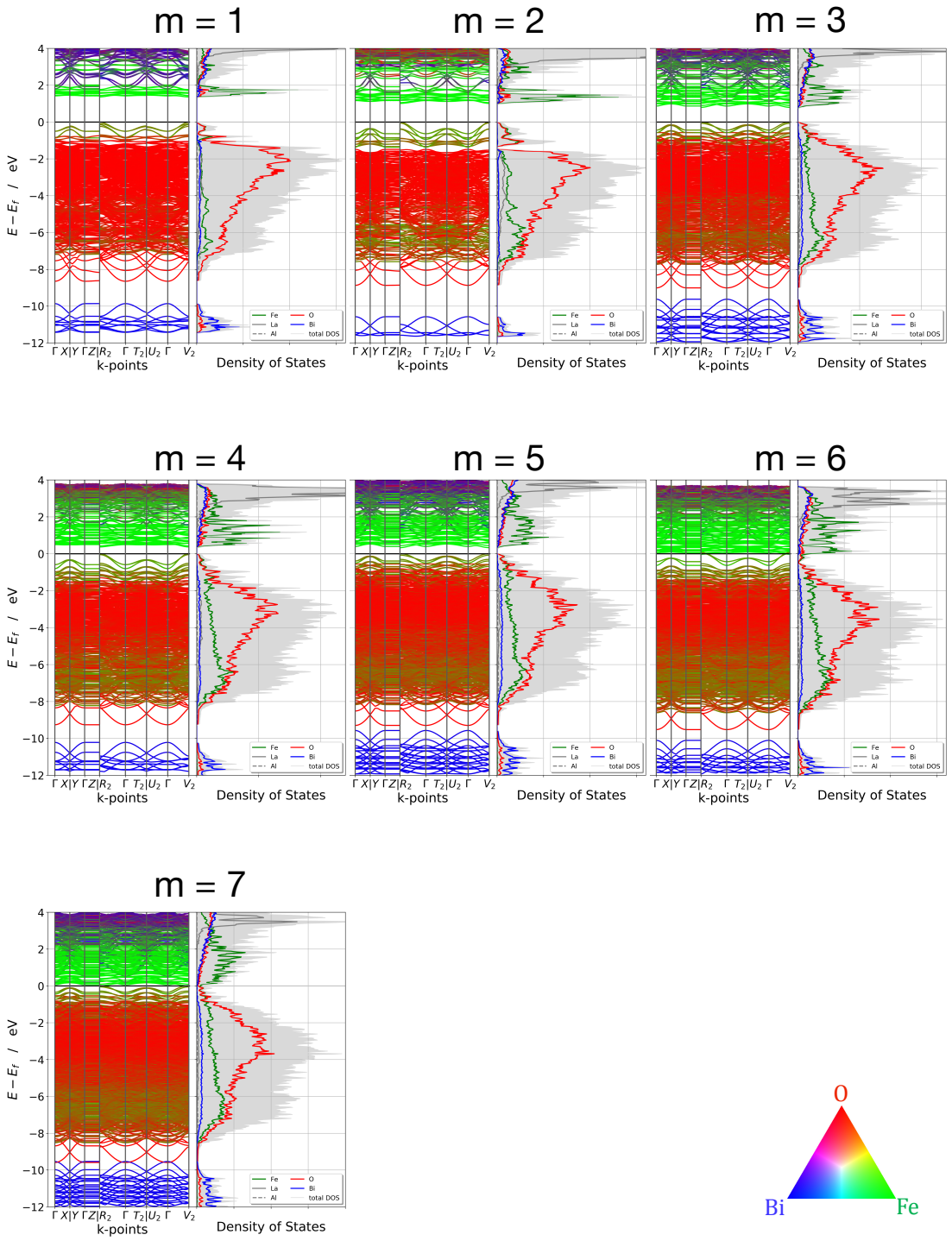

Figure A.6: Electronic band structures for the increasing BFO thickness, in LAO/BFO superlattices. The colours represent elemental contributions. For each band and each k-point, the relative contributions from Bi, O and Fe are projected onto the colour map shown in the bottom right.

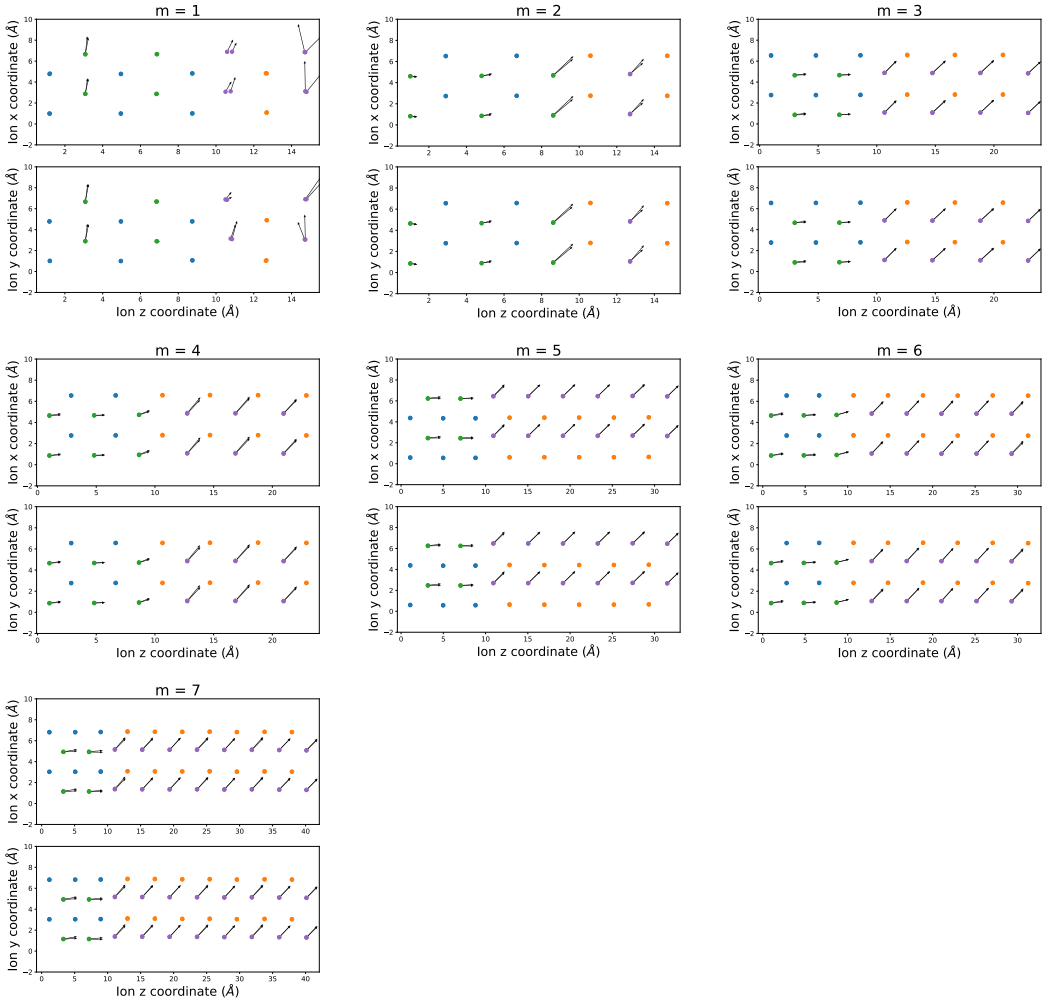

Figure A.7: Local polarisation maps for the LAO/BFO superlattices of varying BFO thickness. Local polarisation vectors are represented by arrows whose length indicates the relative magnitude of the polarisation. The positions of the atoms are given by circles coloured by species: La (green), Al (blue), Bi (purple) and Fe (orange). The O positions are omitted for clarity.

Table A.2: Properties of three low-energy polymorphs of the $m = 5$ SL.

	P111	zigzag	AFD
Total energy w.r.t P111 (meV/atom)	0	4	6
Electronic band gap (eV)	0.325	0.512	1.131
Approx. rotation pattern (Glazer notation)	$a^-a^-c^-$	$a^-a^-c^+$	$a^-a^-c^+$
P_x ($\mu C/cm^2$)	32.70	-1.70	-0.11
P_y ($\mu C/cm^2$)	32.82	-1.86	0.49
P_z ($\mu C/cm^2$)	54.93	46.86	1.41
VBM location	R_2/V_2	R_2/V_2	R_2/V_2
CBM location	R_2/V_2	Γ	R_2/V_2

A.5 Octahedral tilting maps in LAO/BFO superlattices

For each of the superlattices, we compute the octahedral tilting and rotation angles for each BO_6 octahedron. In Fig.A.8 we plot these angles as a function of position along the out-of-plane direction (z).

A.6 Competing local minima

Here we summarise the key factors that distinguish the three identified low-energy structures for the $m = 5$ SL. We label the three polymorphs: P111, zigzag and AFD in relation to their local polarisation patterns (see Fig. A.9). We find the P111 structure to have the lowest total energy, with the zigzag and AFD phases being approximately 4 meV/atom and 6 meV/atom higher in energy, respectively. The P111-type structures are those used throughout Chapter 6, unless otherwise stated.

In Fig.A.9 we show the band structures and local polarisation maps for the P111, zigzag and AFM polymorphs of $m = 5$. In TableA.2 we summarise the key differences between them. The first point to note is the drastic difference in band structures of the three cases. In the AFD band structure, the lowest-lying conduction bands are strongly localised in energy, whereas the corresponding bands in the zigzag and P111 cases are spread over a large energy range. This can be explained by the difference in the out-of-plane polarisation (P_z) of the three cases. The polarisation-induced spreading out the bands in the P111 and zigzag cases reduces their band gap substantially relative to the AFD structure. Another important feature of the band structures is that the P111 and AFD structures both have direct band gaps whereas the zigzag structure has an indirect gap. This has important consequences for the light-absorbing characteristics of the three structures. Finally, we see that a nearly-zero in-plane polarisation (P_x and P_y) is associated with an $a^-a^-c^+$ octahedral rotation pattern, as in the $Pnma$ structure of bulk BFO.

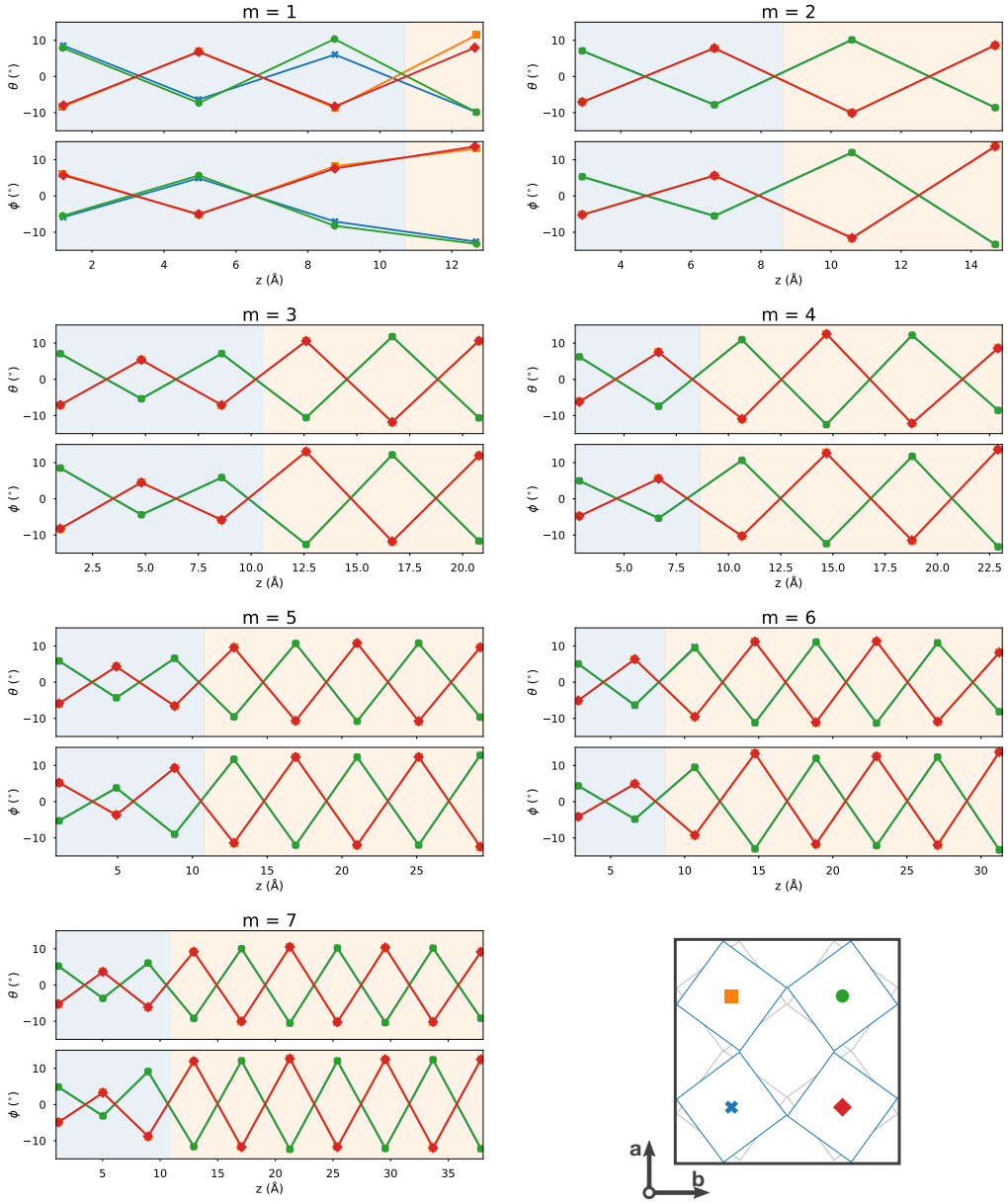

Figure A.8: Octahedral tilting and rotation angles as a function of position along z. We mark and connect angles based on the x and y positions of each octahedron, as shown in the schematic in the final panel. This indicates the anti-phase nature of these rotations. The blue and orange shaded regions indicated LAO and BFO, respectively.

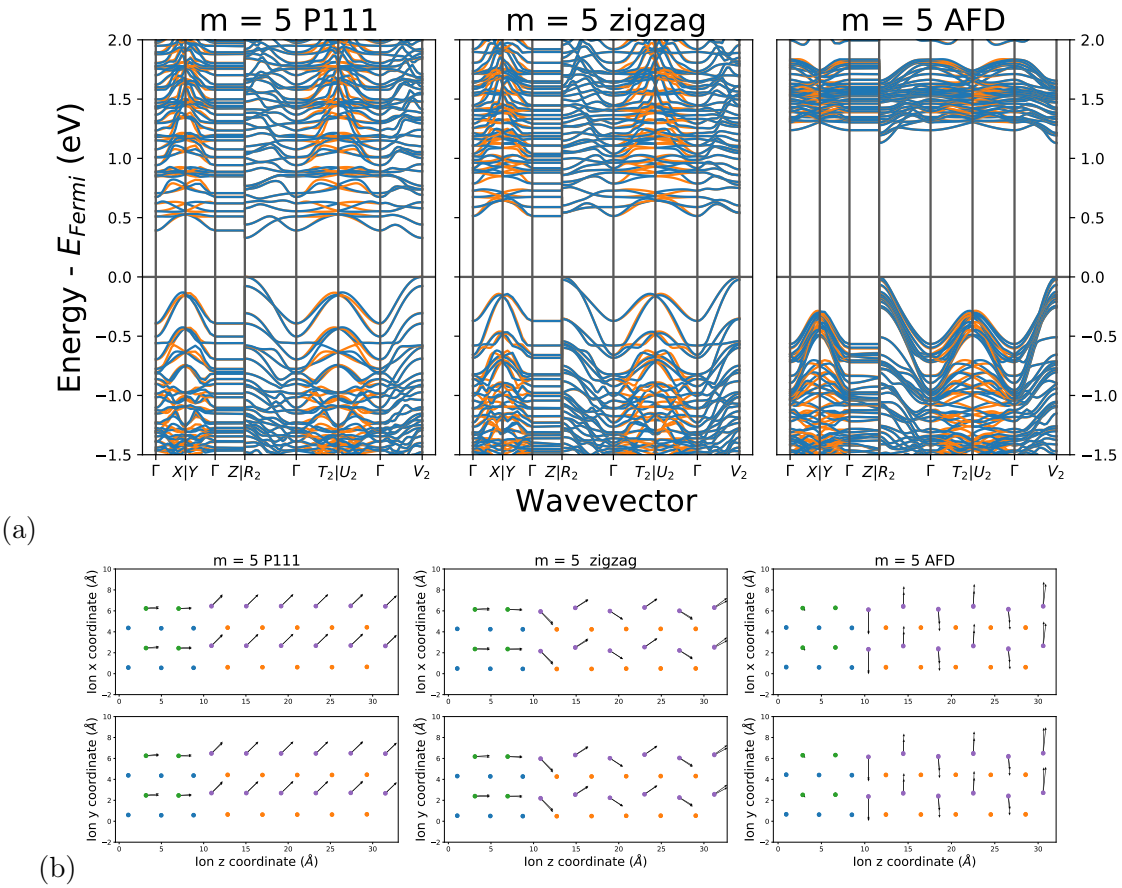

Figure A.9: (a) Band structures and (b) local polarisation for three different low-energy structures of the m = 5 LAO/BFO SL. In (a), the colours correspond to different spin channels. In (b), the positions of the atoms are given by circles coloured by species: La (green), Al (blue), Bi (purple) and Fe (orange). The O positions are omitted for clarity.

Bibliography

[1] Gaëtan Massin, Izumi Kaizuka, and Carlotta Cambiè. A Snapshot of Global PV (1992-2017). Technical report, International Energy Agency, 2018. 13

[2] O. Theodore Benfey. August Kekulé and the birth of the structural theory of organic chemistry in 1858. *Journal of Chemical Education*, 35(1):21, jan 1958. 14

[3] Pavlo Zubko, Jacek C. Wojdeł, Marios Hadjimichael, Stéphanie Fernandez-Pena, Anaïs Sené, Igor Luk'yanchuk, Jean Marc Triscone, and Jorge Íñiguez. Negative capacitance in multidomain ferroelectric superlattices. *Nature*, 534(7608):524–528, jun 2016. 14

[4] Keith T. Butler, Daniel W. Davies, Hugh Cartwright, Olexandr Isayev, and Aron Walsh. Machine learning for molecular and materials science. *Nature*, 559(7715):547–555, jul 2018. 14

[5] Stefano Curtarolo, Gus L.W. Hart, Marco Buongiorno Nardelli, Natalio Mingo, Stefano Sanvito, and Ohad Levy. The high-throughput highway to computational materials design. *Nature Materials*, 12(3):191–201, mar 2013. 14

[6] Scott M. Woodley and Richard Catlow. Crystal structure prediction from first principles. *Nature Materials*, 7(12):937–946, dec 2008. 14, 17

[7] Jeff Greeley, Thomas F. Jaramillo, Jacob Bonde, Ib Chorkendorff, and Jens K. Nørskov. Computational high-throughput screening of electrocatalytic materials for hydrogen evolution. *Nature Materials*, 5(11):909–913, nov 2006. 14

[8] Geoffroy Hautier, Anna Miglio, Gerbrand Ceder, Gian-Marco Rignanese, and Xavier Gonze. Identification and design principles of low hole effective mass p-type transparent conducting oxides. *Nature Communications*, 4, aug 2013. 14, 51

[9] Geoffroy Hautier, Anna Miglio, David Waroquiers, Gian-Marco Rignanese, and Xavier Gonze. How Does Chemistry Influence Electron Effective Mass in Oxides? A High-Throughput Computational Analysis. *Chemistry of Materials*, 26(19):5447–5458, oct 2014. 14, 51

[10] V. M. Fridkin. Bulk photovoltaic effect in noncentrosymmetric crystals. *Crystallography Reports*, 46(4):654–658, jul 2001. 15, 47, 63

[11] S Y Yang, J Seidel, S J Byrnes, P Shafer, C-H Yang, M D Rossell, P Yu, Y-H Chu, J F Scott, J W Ager, L W Martin, and R Ramesh. Above-bandgap voltages from ferroelectric photovoltaic devices. *Nature Nanotechnology*, 5(2):143–7, feb 2010. 15, 47

[12] J Seidel, L W Martin, Q He, Q Zhan, Y-H Chu, A Rother, M E Hawkridge, P Maksymovych, P Yu, M Gajek, N Balke, S V Kalinin, S Gemming, F Wang, G Catalan, J F Scott, N A

Spaldin, J Orenstein, and R Ramesh. Conduction at domain walls in oxide multiferroics. *Nature Materials*, 8(3):229–34, mar 2009. 15, 16, 47, 48

[13] Ce Wen Nan, M. I. Bichurin, Shuxiang Dong, D. Viehland, and G. Srinivasan. Multiferroic magnetoelectric composites: Historical perspective, status, and future directions. *Journal of Applied Physics*, 103(3):031101, feb 2008. 15

[14] Vladimir M. Fridkin. *Photoferroelectrics*, volume 9 of *Springer Series in Solid-State Sciences*. Springer Berlin Heidelberg, Berlin, Heidelberg, 1979. 15

[15] A. G. Chynoweth. Surface space-charge layers in barium titanate. *Physical Review*, 102(3):705–714, may 1956. 15, 63

[16] T. Choi, S. Lee, Y.J. J. Choi, V. Kiryukhin, and S.-W. Cheong. Switchable Ferroelectric Diode and Photovoltaic Effect in $BiFeO_3$. *Science*, 324(5923):63–66, apr 2009. 15, 63, 75

[17] William Shockley and Hans J. Queisser. Detailed balance limit of efficiency of p-n junction solar cells. *Journal of Applied Physics*, 32(3):510, jun 1961. 15

[18] Gustau Catalan and James F. Scott. Physics and Applications of Bismuth Ferrite. *Advanced Materials*, 21(24):2463–2485, jun 2009. 16, 53

[19] Pavlo Zubko, Stefano Gariglio, Marc Gabay, Philippe Ghosez, and Jean-Marc Triscone. Interface Physics in Complex Oxide Heterostructures. *Annual Review of Condensed Matter Physics*, 2(1):141–165, 2011. 16

[20] J. B. Neaton, C. Ederer, U. V. Waghmare, N. A. Spaldin, and K. M. Rabe. First-principles study of spontaneous polarization in multiferroic $BiFeO_3$. *Physical Review B*, 71(1):014113, jan 2005. 17, 27, 48, 50, 51, 54, 59, 60, 65, 66

[21] Claude Ederer and Nicola Spaldin. Weak ferromagnetism and magnetoelectric coupling in bismuth ferrite. *Physical Review B*, 71(6):060401, feb 2005. 17, 48, 50, 76

[22] D. Sando, Bin Xu, L. Bellaiche, and V. Nagarajan. A multiferroic on the brink: Uncovering the nuances of strain-induced transitions in $BiFeO_3$. *Applied Physics Reviews*, 3(1):011106, mar 2016. 18, 48, 64, 69, 81, 86

[23] A. Ohtomo and H. Y. Hwang. A high-mobility electron gas at the $LaAlO_3/SrTiO_3$ heterointerface. *Nature*, 427(6973):423–426, jan 2004. 18

[24] S Gariglio, N Reyren, A D Caviglia, and J. M. Triscone. Superconductivity at the $LaAlO_3/SrTiO_3$ interface. *Journal of Physics: Condensed Matter*, 21(16):164213, apr 2009. 18, 80

[25] A. Brinkman, M. Huijben, M. Van Zalk, J. Huijben, U. Zeitler, J. C. Maan, W. G. Van Der Wiel, G. Rijnders, D. H.A. Blank, and H. Hilgenkamp. Magnetic effects at the interface between non-magnetic oxides. *Nature Materials*, 6(7):493–496, jul 2007. 18, 80

[26] M E Lines and A. M. Glass. *Principles and applications of ferroelectrics and related materials*. International series of monographs on physics Y. Clarendon Press, Oxford, 1977. 21, 24

[27] K. M Rabe, Ch. H. Ahn, J. M M. Triscone, M Dawber, and C Lichtensteiger. *Physics of Ferroelectrics*, volume 105 of *Topics in Applied Physics*. Springer Berlin Heidelberg, 2007. 21, 22, 25

[28] Julio A. Gonzalo and Basílio Jiménez. *Ferroelectricity: The Fundamentals Collection*. Wiley-VCH Verlag GmbH, Weinheim, Germany, jan 2007. 21, 22, 24

[29] J. Valasek. Piezo-electric and allied phenomena in Rochelle salt. *Physical Review*, 17(4):475–481, apr 1921. 21

[30] J. Valasek. Piezo-electric activity of Rochelle Salt under various conditions. *Physical Review*, 19(5):478–491, may 1922. 21

[31] J. C. Slater. Theory of the transition in KH_2PO_4. *The Journal of Chemical Physics*, 9(1):16–33, jan 1941. 21

[32] B.M. Wul and I.M. Goldman. Dielectric constants of titanates of metals of the second group. *Dokl. Akad. Nauk, SSSR*, 46(154), 1945. 21

[33] A. von Hippel, R. G. Breckenridge, F. G. Chesley, and Laszlo Tisza. High dielectric constant ceramics. *Industrial & Engineering Chemistry*, 38(11):1097–1109, nov 1946.

[34] B.M. Wul and I.M. Goldman. Ferroelectric switching in $BaTiO_3$ ceramics. *C.R. Acad. Sci. URSS*, 51(21), 1946. 21

[35] W. Cochran. Crystal stability and the theory of ferroelectricity. *Advances in Physics*, 9(36):387–423, oct 1960. 22

[36] A.F. Devonshire. XCVI. Theory of barium titanate. *The London, Edinburgh, and Dublin Philosophical Magazine and Journal of Science*, 40(309):1040–1063, oct 1949. 22

[37] A.F. Devonshire. CIX. Theory of barium titanate— Part II. *The London, Edinburgh, and Dublin Philosophical Magazine and Journal of Science*, 42(333):1065–1079, oct 1951.

[38] A.F. Devonshire. Theory of ferroelectrics. *Advances in Physics*, 3(10):85–130, apr 1954. 22

[39] R. Clausius. *Die Mechanische Behandlung der Electricität*. Vieweg, Berlin, 1879. 22, 27

[40] O. F. Mossotti. Azioni e deformazioni nei dielettrici. *Memorie di Matematica e di Fisica della Società Italiana delle Scienze Residente in Modena*, 24(49), 1850. 22, 27

[41] Ronald E. Cohen. Origin of ferroelectricity in perovskite oxides. *Nature*, 358(6382):136–138, jul 1992. 23

[42] J F Scott. Ferroelectrics go bananas. *Journal of Physics: Condensed Matter*, 20(2):021001, jan 2008. 23

[43] Y. Xu. *Ferroelectric materials and their applications*. Elsevier Science Publishers B.V., Amsterdam, 1991. 24

[44] Yongping Du, Hang Chen Ding, Li Sheng, Sergey Y Savrasov, Xiangang Wan, and Chun Gang Duan. Microscopic origin of stereochemically active lone pair formation from orbital selective external potential calculations. *Journal of Physics: Condensed Matter*, 26(2):025503, jan 2014. 27

[45] Teng Gu, Timothy Scarbrough, Yurong Yang, Jorge Íñiguez, L Bellaiche, and H. J. Xiang. Cooperative Couplings between Octahedral Rotations and Ferroelectricity in Perovskites and Related Materials. *Physical Review Letters*, 120(19):197602, may 2018. 27

[46] R. Resta. Theory of the electric polarization in crystals. *Ferroelectrics*, 136(1):51–55, nov 1992. 28

[47] Raffaele Resta. Macroscopic polarization in crystalline dielectrics: the geometric phase approach. *Reviews of Modern Physics*, 66(3):899–915, jul 1994. 28

[48] R. D. King-Smith and David Vanderbilt. Theory of polarization of crystalline solids. *Physical Review B*, 47(3):1651–1654, jan 1993. 28, 29, 50, 65

[49] D. Thouless, M. Kohmoto, M. Nightingale, and M. den Nijs. Quantized Hall Conductance in a Two-Dimensional Periodic Potential. *Physical Review Letters*, 49(6):405–408, aug 1982. 29

[50] M. V. Berry. Quantal Phase Factors Accompanying Adiabatic Changes. *Proceedings of the Royal Society A: Mathematical, Physical and Engineering Sciences*, 392(1802):45–57, mar 1984. 30

[51] Raffaele Resta. Manifestations of Berry's phase in molecules and condensed matter. *Journal of Physics: Condensed Matter*, 12(9):R107–R143, mar 2000. 30

[52] Xiao-Liang Qi and Shou-Cheng Zhang. Topological insulators and superconductors. *Reviews of Modern Physics*, 83(4):1057–1110, oct 2011. 30

[53] P Hohenberg and W Kohn. Inhomogeneous Electron Gas. *Physical Review*, 136(3B):B864–B871, nov 1964. 33, 35

[54] P. A. M. Dirac. Quantum Mechanics of Many-Electron Systems. *Proceedings of the Royal Society A: Mathematical, Physical and Engineering Sciences*, 123(792):714–733, apr 1929. 33

[55] W. Kohn and L. J. Sham. Self-consistent equations including exchange and correlation effects. *Physical Review*, 140(4A), 1965. 36

[56] G P Kerker. Non-singular atomic pseudopotentials for solid state applications. *Journal of Physics C: Solid State Physics*, 13(9):L189–L194, mar 1980. 37

[57] H Akai and P H Dederichs. A simple improved iteration scheme for electronic structure calculations. *Journal of Physics C: Solid State Physics*, 18(12):2455–2460, apr 1985.

[58] Péter Pulay. Convergence acceleration of iterative sequences. the case of scf iteration. *Chemical Physics Letters*, 73(2):393–398, jul 1980.

[59] D. D. Johnson. Modified Broyden's method for accelerating convergence in self-consistent calculations. *Physical Review B*, 38(18):12807–12813, dec 1988. 37

[60] D. M. Ceperley. Ground State of the Electron Gas by a Stochastic Method. *Physical Review Letters*, 45(7):566–569, aug 1980. 38

[61] John P Perdew, Kieron Burke, and Matthias Ernzerhof. Generalized Gradient Approximation Made Simple. *Physical Review Letters*, 77(18):3865–3868, oct 1996. 38, 49, 65

[62] Agostino Zoroddu, Fabio Bernardini, Paolo Ruggerone, and Vincenzo Fiorentini. First-principles prediction of structure, energetics, formation enthalpy, elastic constants, polarization, and piezoelectric constants of AlN, GaN, and InN: Comparison of local and gradient-corrected density-functional theory. *Physical Review B*, 64(4):45208, 2001. 38

[63] John P. Perdew, Adrienn Ruzsinszky, Gábor I. Csonka, Oleg A. Vydrov, Gustavo E. Scuseria, Lucian A. Constantin, Xiaolan Zhou, and Kieron Burke. Restoring the Density-Gradient Expansion for Exchange in Solids and Surfaces. *Physical Review Letters*, 100(13):136406, apr 2008. 38, 49

[64] Richard Van Noorden, Brendan Maher, and Regina Nuzzo. The top 100 papers. *Nature*, 514(7524):550–553, oct 2014. 38

[65] John P. Perdew, Robert G. Parr, Mel Levy, and Jose L. Balduz. Density-Functional Theory for Fractional Particle Number: Derivative Discontinuities of the Energy. *Physical Review Letters*, 49(23):1691–1694, dec 1982. 39

[66] Aron J. Cohen, Paula Mori-Sánchez, and Weitao Yang. Fractional spins and static correlation error in density functional theory. *The Journal of Chemical Physics*, 129(12):121104, sep 2008. 39

[67] Paula Mori-Sánchez, Aron J Cohen, and Weitao Yang. Discontinuous nature of the exchange-correlation functional in strongly correlated systems. *Physical Review Letters*, 102(6), 2009. 39

[68] Aron J Cohen, P. Mori-Sánchez, and Weitao Yang. Insights into Current Limitations of Density Functional Theory. *Science*, 321(5890):792–794, aug 2008. 39

[69] Thomas Körzdörfer, Robert M. Parrish, Noa Marom, John S. Sears, C. David Sherrill, and Jean-Luc Brédas. Assessment of the performance of tuned range-separated hybrid density functionals in predicting accurate quasiparticle spectra. *Physical Review B*, 86(20):205110, nov 2012. 40

[70] Axel D. Becke. Density-functional thermochemistry. IV. A new dynamical correlation functional and implications for exact-exchange mixing. *The Journal of Chemical Physics*, 104(3):1040–1046, jan 1996. 40

[71] John P. Perdew, Matthias Ernzerhof, and Kieron Burke. Rationale for mixing exact exchange with density functional approximations. *Journal of Chemical Physics*, 105(22):9982–9985, jun 1996. 40

[72] A Stroppa and S Picozzi. Hybrid functional study of proper and improper multiferroics. *Physical Chemistry Chemical Physics*, 12(20):5405–16, jan 2010. 40, 48, 52, 58

[73] Jochen Heyd, Gustavo E. Scuseria, and Matthias Ernzerhof. Hybrid functionals based on a screened Coulomb potential. *The Journal of Chemical Physics*, 118(18):8207, apr 2003. 40

[74] Fabien Tran and Peter Blaha. Accurate Band Gaps of Semiconductors and Insulators with a Semilocal Exchange-Correlation Potential. *Physical Review Letters*, 102(22):226401, jun 2009. 41

[75] Jianwei Sun, Adrienn Ruzsinszky, and Johnp Perdew. Strongly Constrained and Appropriately Normed Semilocal Density Functional. *Physical Review Letters*, 115(3):036402, jul 2015. 41, 49, 84

[76] Yubo Zhang, Jianwei Sun, John P Perdew, and Xifan Wu. Comparative first-principles studies of prototypical ferroelectric materials by LDA, GGA, and SCAN meta-GGA. *Physical Review B*, 96(3):035143, jul 2017. 41, 85, 94

[77] D. I. Bilc, R. Orlando, R. Shaltaf, G.-M. Rignanese, Jorge Íñiguez, and Ph. Ghosez. Hybrid exchange-correlation functional for accurate prediction of the electronic and structural properties of ferroelectric oxides. *Physical Review B*, 77(16):165107, apr 2008. 41

[78] M. Goffinet, P. Hermet, D. I. Bilc, and Ph. Ghosez. Hybrid functional study of prototypical multiferroic bismuth ferrite. *Physical Review B*, 79(1):014403, jan 2009.

[79] Alina Prikockytė, Daniel Bilc, Patrick Hermet, Catherine Dubourdieu, and Philippe Ghosez. First-principles calculations of the structural and dynamical properties of ferroelectric $YMnO_3$. *Physical Review B*, 84(21):214301, dec 2011. 41

[80] Vladimir I. Anisimov, Jan Zaanen, and Ole K. Andersen. Band theory and Mott insulators: Hubbard U instead of Stoner I. *Physical Review B*, 44(3):943–954, jul 1991. 41, 42

[81] Eva Pavarini, Erik Koch, Frithjof Anders, and Mark (Eds.) Jarrell. *Correlated electrons: from models to materials*, volume 2 of *Schriften des Forschungszentrums Jülich. Reihe Modeling and simulation*. Forschungszentrum Jülich GmbH, Jülich, 2012. 41, 48

[82] J. Hubbard. Electron Correlations in Narrow Energy Bands. *Proceedings of the Royal Society A: Mathematical, Physical and Engineering Sciences*, 276(1365):238–257, nov 1963. 41

[83] J. Hubbard. Electron Correlations in Narrow Energy Bands. II. The Degenerate Band Case. *Proceedings of the Royal Society A: Mathematical, Physical and Engineering Sciences*, 277(1369):237–259, jan 1964.

[84] J. Hubbard. Electron Correlations in Narrow Energy Bands. III. An Improved Solution. *Proceedings of the Royal Society A: Mathematical, Physical and Engineering Sciences*, 281(1386):401–419, sep 1964.

[85] J. Hubbard. Electron Correlations in Narrow Energy Bands. IV. The Atomic Representation. *Proceedings of the Royal Society A: Mathematical, Physical and Engineering Sciences*, 285(1403):542–560, may 1965.

[86] J. Hubbard. Electron Correlations in Narrow Energy Bands. V. A Perturbation Expansion About the Atomic Limit. *Proceedings of the Royal Society A: Mathematical, Physical and Engineering Sciences*, 296(1444):82–99, jan 1967.

[87] J. Hubbard. Electron Correlations in Narrow Energy Bands. VI. The Connexion with Many-Body Perturbation Theory. *Proceedings of the Royal Society A: Mathematical, Physical and Engineering Sciences*, 296(1444):100–112, jan 1967. 41

[88] V. I. Anisimov, I. V. Solovyev, M. A. Korotin, M. T. Czyżyk, and G. A. Sawatzky. Density-functional theory and NiO photoemission spectra. *Physical Review B*, 48(23):16929–16934, dec 1993. 42

[89] I. V. Solovyev, P H Dederichs, and V I Anisimov. Corrected atomic limit in the local-density approximation and the electronic structure of d impurities in Rb. *Physical Review B*, 50(23):16861–16871, dec 1994.

[90] A I Liechtenstein, V I Anisimov, and J Zaanen. Density-functional theory and strong interactions: Orbital ordering in Mott-Hubbard insulators. *Physical Review B*, 52(8):R5467–R5470, aug 1995. 42

[91] S. L. Dudarev, S. Y. Savrasov, C. J. Humphreys, A. P. Sutton, G. A. Botton, S. Y. Savrasov, C. J. Humphreys, and A. P. Sutton. Electron-energy-loss spectra and the structural stability of nickel oxide: An LSDA+U study. *Physical Review B*, 57(3):1505–1509, jan 1998. 42, 48, 49, 65

[92] D R Bowler and T Miyazaki. O(N) methods in electronic structure calculations. *Reports on Progress in Physics*, 75(3):036503, mar 2012. 43

[93] David Vanderbilt. Soft self-consistent pseudopotentials in a generalized eigenvalue formalism. *Physical Review B*, 41(11):7892, 1990. 44

[94] Peter E. Blöchl. Generalized separable potentials for electronic-structure calculations. *Physical Review B*, 41(8):5414–5416, mar 1990. 44

[95] P. E. Blöchl. Projector augmented-wave method. *Physical Review B*, 50(24):17953–17979, dec 1994. 45, 49, 65, 85

[96] Ji Hye Lee, Ignasi Fina, Xavi Marti, Young Heon Kim, Dietrich Hesse, and Marin Alexe. Spintronic functionality of $BiFeO_3$ domain walls. *Advanced Materials*, 26(41):7078–7082, nov 2014. 47, 48

[97] Wei Ji, Kui Yao, and Yung C. Liang. Bulk photovoltaic effect at visible wavelength in epitaxial ferroelectric $BiFeO_3$ thin films. *Advanced Materials*, 22(15):1763–1766, apr 2010. 47, 75

[98] Charles Paillard, Xiaofei Bai, Ingrid C. Infante, Maël Guennou, Grégory Geneste, Marin Alexe, Jens Kreisel, and Brahim Dkhil. Photovoltaics with Ferroelectrics: Current Status and Beyond. *Advanced Materials*, 28(26):5153–5168, jul 2016. 47, 75

[99] V. V. Shvartsman, W. Kleemann, R. Haumont, and J. Kreisel. Large bulk polarization and regular domain structure in ceramic $BiFeO_3$. *Applied Physics Letters*, 90(17):172115, 2007. 47, 63

[100] D. Lebeugle, D. Colson, A. Forget, and M. Viret. Very large spontaneous electric polarization in $BiFeO_3$ single crystals at room temperature and its evolution under cycling fields. *Applied Physics Letters*, 91(2):022907, jul 2007. 47, 63, 66

[101] Wei Ji, Kui Yao, and Yung C. Liang. Evidence of bulk photovoltaic effect and large tensor coefficient in ferroelectric $BiFeO_3$ thin films. *Physical Review B*, 84(9):094115, sep 2011. 47

[102] D Sando, A Barthélémy, and M Bibes. $BiFeO_3$ epitaxial thin films and devices: past, present and future. *Journal of Physics: Condensed Matter*, 26(47):473201, nov 2014. 48, 64, 69, 81

[103] Akash Bhatnagar, Ayan Roy Chaudhuri, Young Heon Kim, Dietrich Hesse, and Marin Alexe. Role of domain walls in the abnormal photovoltaic effect in $BiFeO_3$. *Nature Communications*, 4(May):2835, nov 2013. 48

[104] Qing-Yan Rong, Ling-Ling Wang, Wen-Zhi Xiao, and Liang Xu. First-principles study of magnetic properties in Co-doped $BiFeO_3$. *Physica B: Condensed Matter*, 457(34):1–4, jan 2015. 48, 54, 75

[105] Q.J. Wang, Q.H. Tan, and Y.K. Liu. First-principles study on ferromagnetism in Mn-doped tetragonal $BiFeO_3$. *Computational Materials Science*, 105:1–5, jul 2015. 48, 54, 75

[106] James M. Rondinelli, Steven J. May, and John W. Freeland. Control of octahedral connectivity in perovskite oxide heterostructures: An emerging route to multifunctional materials discovery. *MRS Bulletin*, 37(03):261–270, mar 2012. 48, 75

[107] A. Y. Borisevich, H. J. Chang, M. Huijben, M. P. Oxley, S. Okamoto, M. K. Niranjan, J. D. Burton, E. Y. Tsymbal, Y. H. Chu, P. Yu, R. Ramesh, S. V. Kalinin, and S. J. Pennycook. Suppression of Octahedral Tilts and Associated Changes in Electronic Properties at Epitaxial Oxide Heterostructure Interfaces. *Physical Review Letters*, 105(8):087204, aug 2010. 53, 75, 79

[108] Chao-Chao Zhou, Ke-xin Jin, Bing-Cheng Luo, Xian-sheng Cao, and Chang-Le Chen. Photoconductivity in $BiFeO_3/La_{0.7}Sr_{0.3}MnO_3$ heterostructure. *Materials Letters*, 64(15):1713–1716, aug 2010.

[109] P Yu, W Luo, D Yi, J X Zhang, M D Rossell, C-H Yang, L You, G Singh-Bhalla, S Y Yang, Q He, Q M Ramasse, R Erni, L W Martin, Y H Chu, S T Pantelides, S J Pennycook, and R Ramesh. Interface control of bulk ferroelectric polarization. *Proceedings of the National Academy of Sciences of the United States of America*, 109(25):9710–5, jun 2012. 64

[110] Young-Min Kim, Amit Kumar, Alison Hatt, Anna N. Morozovska, Alexander Tselev, Michael D. Biegalski, Ilya Ivanov, Eugene A. Eliseev, Stephen J. Pennycook, James M. Rondinelli, Sergei V. Kalinin, and Albina Y. Borisevich. Interplay of Octahedral Tilts and Polar Order in $BiFeO_3$ Films. *Advanced Materials*, 25(17):2497–2504, may 2013. 48, 53, 64, 75, 79

[111] Lei Wang, Thomas Maxisch, and Gerbrand Ceder. Oxidation energies of transition metal oxides within the GGA+U framework. *Physical Review B*, 73(19):195107, may 2006. 48

[112] Matteo Cococcioni and Stefano de Gironcoli. Linear response approach to the calculation of the effective interaction parameters in the LDA+U method. *Physical Review B*, 71(3):035105, jan 2005. 49

[113] Igor A. Kornev, S. Lisenkov, R. Haumont, B. Dkhil, and L. Bellaiche. Finite-Temperature Properties of Multiferroic $BiFeO_3$. *Physical Review Letters*, 99(22):227602, nov 2007. 49, 54

[114] Steve M. Young, Fan Zheng, and Andrew M. Rappe. First-Principles Calculation of the Bulk Photovoltaic Effect in Bismuth Ferrite. *Physical Review Letters*, 109(23):236601, dec 2012. 49, 54, 60, 64

[115] G. Kresse and J. Hafner. Ab initio molecular dynamics for liquid metals. *Physical Review B*, 47(1):558–561, jan 1993. 49, 65, 84

[116] G. Kresse and J. Hafner. Ab initio molecular-dynamics simulation of the liquid-metal–amorphous-semiconductor transition in germanium. *Physical Review B*, 49(20):14251–14269, may 1994.

[117] G. Kresse and J. Furthmüller. Efficiency of ab-initio total energy calculations for metals and semiconductors using a plane-wave basis set. *Computational Materials Science*, 6(1):15–50, jul 1996.

[118] G. Kresse and J. Furthmüller. Efficient iterative schemes for ab initio total-energy calculations using a plane-wave basis set. *Physical Review B*, 54(16):11169–11186, oct 1996. 49, 65, 84

[119] G. Kresse and D. Joubert. From ultrasoft pseudopotentials to the projector augmented-wave method. *Physical Review B*, 59(3):1758–1775, jan 1999. 49, 65, 85

[120] Hendrik J Monkhorst and James D Pack. Special points for Brillouin-zone integrations. *Physical Review B*, 13(12):5188–5192, jun 1976. 49, 65

[121] A Palewicz, R Przeniosło, I Sosnowska, and A W Hewat. Atomic displacements in $BiFeO_3$ as a function of temperature: neutron diffraction study. *Acta Crystallographica Section B Structural Science*, 63(4):537–544, aug 2007. 49, 52, 53, 54, 100

[122] I Sosnowska, T P Neumaier, and E Steichele. Spiral magnetic ordering in bismuth ferrite. *Journal of Physics C: Solid State Physics*, 15(23):4835–4846, aug 1982. 49, 65

[123] David Vanderbilt and R. D. King-Smith. Electric polarization as a bulk quantity and its relation to surface charge. *Physical Review B*, 48(7):4442–4455, aug 1993. 50

[124] Raffaele Resta. Modern theory of polarization in ferroelectrics. *Ferroelectrics*, 151(1):49–58, 1994. 50, 65

[125] Alexandr Fonari and Christopher Sutton. Effective Mass Calculator (v1.50), 2012. 50

[126] J. Kane Shenton, Wei Li Cheah, and David R. Bowler. Supplementary information for a study of DFT+U in the context of $BiFeO_3$; DOI: 10.5281/zenodo.597611, 2017. 51, 56, 58, 59, 60

[127] A. Palewicz, T. Szumiata, R. Przeniosło, I. Sosnowska, and I. Margiolaki. Search for new modulations in the $BiFeO_3$ structure: SR diffraction and Mössbauer studies. *Solid State Communications*, 140(7-8):359–363, nov 2006. 52

[128] A. M. Glazer. The classification of tilted octahedra in perovskites. *Acta Crystallographica Section B: Structural Crystallography and Crystal Chemistry*, 28(11):3384–3392, nov 1972. 53, 67, 84

[129] J.M. Moreau, C. Michel, R. Gerson, and W.J. James. Ferroelectric $BiFeO_3$ X-ray and neutron diffraction study. *Journal of Physics and Chemistry of Solids*, 32(6):1315–1320, jan 1971. 54

[130] F. Kubel and H. Schmid. Structure of a ferroelectric and ferroelastic monodomain crystal of the perovskite $BiFeO_3$. *Acta Crystallographica Section B*, 46(6):698–702, dec 1990.

[131] H. D. Megaw and C. N W Darlington. Geometrical and structural relations in the rhombohedral perovskites. *Acta Crystallographica Section A*, 31(2):161–173, mar 1975. 54

[132] Zuhuang Chen, S. Prosandeev, Z. L. Luo, Wei Ren, Yajun Qi, C. W. Huang, Lu You, C. Gao, I. A. Kornev, Tom Wu, Junling Wang, P. Yang, T. Sritharan, L. Bellaiche, and Lang Chen. Coexistence of ferroelectric triclinic phases in highly strained $BiFeO_3$ films. *Physical Review B*, 84(9):094116, sep 2011. 54

[133] S.H. Chu, D.J. Singh, J. Wang, E.-P. Li, and K.P. Ong. High optical performance and practicality of active plasmonic devices based on rhombohedral $BiFeO_3$. *Laser & Photonics Reviews*, 6(5):684–689, sep 2012.

[134] H. M. Tütüncü and G. P. Srivastava. Electronic structure and lattice dynamical properties of different tetragonal phases of $BiFeO_3$. *Physical Review B*, 78(23):235209, dec 2008.

[135] Yaming Jin, Xiaomei Lu, Junting Zhang, Yi Kan, Huifeng Bo, Fengzhen Huang, Tingting Xu, Yingchao Du, Shuyu Xiao, and Jinsong Zhu. Studying the Polarization Switching in Polycrystalline $BiFeO_3$ Films by 2D Piezoresponse Force Microscopy. *Scientific Reports*, 5:12237, jul 2015. 54

[136] Shunyi Li, Jan Morasch, Andreas Klein, Christina Chirila, Lucian Pintilie, Lichao Jia, Klaus Ellmer, Michael Naderer, Klaus Reichmann, Melanie Gröting, and Karsten Albe. Influence of orbital contributions to the valence band alignment of Bi_2O_3, Fe_2O_3, $BiFeO_3$, and $Bi0.5Na0.5TiO_3$. *Physical Review B*, 88(4):045428, jul 2013. 58

[137] A Scaramucci, J Ammann, N A Spaldin, and C Ederer. Separating different contributions to the crystal-field parameters using Wannier functions. *Journal of Physics: Condensed Matter*, 27(17):175503, may 2015. 58

[138] F. Gao, Y. Yuan, K. F. Wang, X. Y. Chen, F. Chen, J.-M. Liu, and Z. F. Ren. Preparation and photoabsorption characterization of $BiFeO_3$ nanowires. *Applied Physics Letters*, 89(10):102506, sep 2006. 60

[139] Amit Kumar, Ram C. Rai, Nikolas J. Podraza, Sava Denev, Mariola Ramirez, Ying-Hao Chu, Lane W. Martin, Jon Ihlefeld, T. Heeg, J. Schubert, Darrell G. Schlom, J. Orenstein, R. Ramesh, Robert W. Collins, Janice L. Musfeldt, and Venkatraman Gopalan. Linear and nonlinear optical properties of $BiFeO_3$. *Applied Physics Letters*, 92(12):121915, 2008.

[140] Reda Moubah, Guy Schmerber, Olivier Rousseau, Dorothée Colson, and Michel Viret. Photoluminescence Investigation of Defects and Optical Band Gap in Multiferroic $BiFeO_3$ Single Crystals. *Applied Physics Express*, 5(3):035802, feb 2012. 60

[141] John P Perdew. Density functional theory and the band gap problem. *International Journal of Quantum Chemistry*, 30(3):451–451, sep 1986. 60

[142] Yongbo Yuan, Zhengguo Xiao, Bin Yang, and Jinsong Huang. Arising applications of ferroelectric materials in photovoltaic devices. *Journal of Materials Chemistry A*, 2(17):6027–6041, 2014. 64

[143] Keith T Butler, Jarvist M Frost, and Aron Walsh. Ferroelectric materials for solar energy conversion: photoferroics revisited. *Energy & Environmental Science*, 8(3):838–848, dec 2015.

[144] Haitao Huang. Solar energy: Ferroelectric photovoltaics. *Nature Photonics*, 4(3):134–135, mar 2010. 64

[145] Y. Sun, S. E. Thompson, and T. Nishida. Physics of strain effects in semiconductors and metal-oxide-semiconductor field-effect transistors. *Journal of Applied Physics*, 101(10):104503, may 2007. 64

[146] J. Kane Shenton, David R Bowler, and Wei Li Cheah. Supplementary information for a study of the influence of structure on effective mass in $BiFeO_3$; DOI: 10.5281/zenodo.1198207, mar 2018. 65, 66, 69, 73, 76

[147] Oswaldo Diéguez, O. E. González-Vázquez, Jacek C. Wojdeł, and Jorge Íñiguez. First-principles predictions of low-energy phases of multiferroic $BiFeO_3$. *Physical Review B*, 83(9):94105, mar 2011. 66

[148] Alison J. Hatt, Nicola A. Spaldin, and Claude Ederer. Strain-induced isosymmetric phase transition in $BiFeO_3$. *Physical Review B*, 81(5):054109, feb 2010. 66

[149] Claude Ederer and Nicola A Spaldin. Influence of strain and oxygen vacancies on the magnetoelectric properties of multiferroic bismuth ferrite. *Physical Review B*, 71(22):224103, jun 2005. 66, 69

[150] P. Ravindran, R. Vidya, A. Kjekshus, H. Fjellvåg, and O. Eriksson. Theoretical investigation of magnetoelectric behavior in $BiFeO_3$. *Physical Review B*, 74(22):224412, dec 2006. 66

[151] Claude Ederer and Nicola A. Spaldin. Effect of Epitaxial Strain on the Spontaneous Polarization of Thin Film Ferroelectrics. *Physical Review Letters*, 95(25):257601, dec 2005. 66, 69

[152] J. X. Zhang, Q. He, M. Trassin, W. Luo, D. Yi, M. D. Rossell, P. Yu, L. You, C. H. Wang, C. Y. Kuo, J. T. Heron, Z. Hu, R. J. Zeches, H. J. Lin, A. Tanaka, C. T. Chen, L. H. Tjeng, Y. H. Chu, and R. Ramesh. Microscopic origin of the giant ferroelectric polarization in tetragonal-like $BiFeO_3$. *Physical Review Letters*, 107(14):147602, sep 2011. 66

[153] D. S. Rana, K. Takahashi, K. R. Mavani, I. Kawayama, H. Murakami, M. Tonouchi, T. Yanagida, H. Tanaka, and T. Kawai. Thickness dependence of the structure and magnetization of $BiFeO_3$ thin films on $(LaAlO_3)_{0.3}(Sr_2AlTaO_6)_{0.7}$ (001) substrate. *Physical Review B*, 75(6):060405, feb 2007. 69

[154] I. C. Infante, S. Lisenkov, B. Dupé, M. Bibes, S. Fusil, E. Jacquet, G. Geneste, S. Petit, A. Courtial, J. Juraszek, L. Bellaiche, A. Barthélémy, and B. Dkhil. Bridging multiferroic phase transitions by epitaxial strain in $BiFeO_3$. *Physical Review Letters*, 105(5):057601, jul 2010.

[155] D. Sando, A. Agbelele, D. Rahmedov, J. Liu, P. Rovillain, C. Toulouse, I. C. Infante, A. P. Pyatakov, S. Fusil, E. Jacquet, C. Carrétéro, C. Deranlot, S. Lisenkov, D. Wang, J-M. Le Breton, M. Cazayous, A. Sacuto, J. Juraszek, A. K. Zvezdin, L. Bellaiche, B. Dkhil, A. Barthélémy, and M. Bibes. Crafting the magnonic and spintronic response of $BiFeO_3$ films by epitaxial strain. *Nature Materials*, 12(7):641–646, apr 2013. 69

[156] Thomas A. Mellan, Furio Corà, Ricardo Grau-Crespo, and Sohrab Ismail-Beigi. Importance of anisotropic Coulomb interaction in $LaMnO_3$. *Physical Review B*, 92(8):085151, aug 2015. 73

[157] S. Y. Yang, L. W. Martin, S. J. Byrnes, T. E. Conry, S. R. Basu, D. Paran, L. Reichertz, J. Ihlefeld, C. Adamo, A. Melville, Y.-H. Chu, C.-H. Yang, J. L. Musfeldt, D. G. Schlom, J. W. Ager, and R. Ramesh. Photovoltaic effects in $BiFeO_3$. *Applied Physics Letters*, 95(6):062909, aug 2009. 75

[158] Fen Wu, Yiping Guo, Yangyang Zhang, Huanan Duan, Hua Li, and Hezhou Liu. Enhanced Photovoltaic Performance in Polycrystalline $BiFeO_3$ Thin Film/ZnO Nanorod Heterojunctions. *The Journal of Physical Chemistry C*, 118(28):15200–15206, jul 2014. 75

[159] Jun He, Albina Borisevich, Sergei V. Kalinin, Stephen J. Pennycook, and Sokrates T. Pantelides. Control of octahedral tilts and magnetic properties of perovskite oxide heterostructures by substrate symmetry. *Physical Review Letters*, 105(22):227203, nov 2010. 75

[160] Daisuke Kan, Ryotaro Aso, Riko Sato, Mitsutaka Haruta, Hiroki Kurata, and Yuichi Shimakawa. Tuning magnetic anisotropy by interfacially engineering the oxygen coordination environment in a transition metal oxide. *Nature Materials*, 15(April):432, mar 2016. 75, 79

[161] P. Chen, N. J. Podraza, X. S. Xu, A. Melville, E. Vlahos, V. Gopalan, R. Ramesh, D. G. Schlom, and J. L. Musfeldt. Optical properties of quasi-tetragonal $BiFeO_3$ thin films. *Applied Physics Letters*, 96(13):131907, mar 2010. 75

[162] Georg K.H. Madsen and David J. Singh. BoltzTraP. A code for calculating band-structure dependent quantities. *Computer Physics Communications*, 175(1):67–71, jul 2006. 76

[163] Z. Yang, C. Ke, L.L. Sun, W. Zhu, L. Wang, X.F. Chen, and O.K. Tan. Growth and structure investigation of multiferroic superlattices: $[(La_{0.8}Sr_{0.2}MnO_3)_{4n}/(BaTiO_3)_{3n}]_m$. *Solid State Communications*, 150(31-32):1432–1435, aug 2010. 79

[164] Ryotaro Aso, Daisuke Kan, Yoshifumi Fujiyoshi, Yuichi Shimakawa, and Hiroki Kurata. Strong dependence of oxygen octahedral distortions in $SrRuO_3$ films on types of substrate-induced epitaxial strain. *Crystal Growth and Design*, 14(12):6478–6485, dec 2014. 79

[165] Ryotaro Aso, Daisuke Kan, Yuichi Shimakawa, and Hiroki Kurata. Octahedral tilt propagation controlled by A-site cation size at perovskite oxide heterointerfaces. *Crystal Growth and Design*, 14(5):2128–2132, may 2014. 79

[166] MB Shalom, M Sachs, D Rakhmilevitch, A Palevski, and Y Dagan. Tuning Spin-Orbit Coupling and Superconductivity at the $SrTiO_3/LaAlO_3$ Interface: A Magnetotransport Study. *Physical Review Letters*, 104(12), 2010. 80

[167] Julie A. Bert, Beena Kalisky, Christopher Bell, Minu Kim, Yasuyuki Hikita, Harold Y. Hwang, and Kathryn A. Moler. Direct imaging of the coexistence of ferromagnetism and superconductivity at the $LaAlO_3/SrTiO_3$ interface. *Nature Physics*, 7(10):767–771, oct 2011. 80

[168] N C Bristowe, P B Littlewood, and Emilio Artacho. The net charge at interfaces between insulators. *Journal of Physics: Condensed Matter*, 23(8):081001, mar 2011. 80

[169] N C Bristowe, Philippe Ghosez, P B Littlewood, and Emilio Artacho. The origin of two-dimensional electron gases at oxide interfaces: insights from theory. *Journal of Physics: Condensed Matter*, 26(14):143201, apr 2014. 80

[170] M. L. Reinle-Schmitt, C. Cancellieri, D. Li, D. Fontaine, M. Medarde, E. Pomjakushina, C. W. Schneider, S. Gariglio, Ph. Ghosez, J. M. Triscone, and P. R. Willmott. Tunable conductivity threshold at polar oxide interfaces. *Nature Communications*, 3(1):932, jan 2012. 80

[171] A. Annadi, Q. Zhang, X. Renshaw Wang, N. Tuzla, K. Gopinadhan, W. M. Lü, A. Roy Barman, Z. Q. Liu, A. Srivastava, S. Saha, Y. L. Zhao, S. W. Zeng, S. Dhar, E. Olsson, B. Gu, S. Yunoki, S. Maekawa, H. Hilgenkamp, T. Venkatesan, and A. Ariando. Anisotropic two-dimensional electron gas at the $LaAlO_3/SrTiO_3$ (110) interface. *Nature Communications*, 4(1):1838, dec 2013. 80

[172] C. Cen, S. Thiel, G. Hammerl, C. W. Schneider, K. E. Andersen, C. S. Hellberg, J. Mannhart, and J. Levy. Nanoscale control of an interfacial metal-insulator transition at room temperature. *Nature Materials*, 7(4):298–302, apr 2008. 80

[173] B. Förg, C. Richter, and J. Mannhart. Field-effect devices utilizing $LaAlO_3$-$SrTiO_3$ interfaces. *Applied Physics Letters*, 100(5):053506, jan 2012.

[174] Masayuki Hosoda, Yasuyuki Hikita, Harold Y. Hwang, and Christopher Bell. Transistor operation and mobility enhancement in top-gated $LaAlO_3/SrTiO_3$ heterostructures. *Applied Physics Letters*, 103(10):103507, sep 2013. 80

[175] Christian Mix, Simone Finizio, Mathias Kläui, and Gerhard Jakob. Conductance control at the $LaAlO_3/SrTiO_3$-interface by a multiferroic $BiFeO_3$ ad-layer. *Applied Physics Letters*, 104(26):262903, jun 2014. 80

[176] P. Aguado-Puente, N. C. Bristowe, B. Yin, R. Shirasawa, Philippe Ghosez, P. B. Littlewood, and Emilio Artacho. Model of two-dimensional electron gas formation at ferroelectric interfaces. *Physical Review B*, 92(3):035438, jul 2015. 80

[177] Binglun Yin, Pablo Aguado-Puente, Shaoxing Qu, and Emilio Artacho. Two-dimensional electron gas at the $PbTiO_3/SrTiO_3$ interface: An ab initio study. *Physical Review B*, 92(11):115406, sep 2015. 80, 92

[178] Zhen Zhang, Ping Wu, Lang Chen, and Junling Wang. First-principles prediction of a two dimensional electron gas at the $BiFeO_3/SrTiO_3$ interface. *Applied Physics Letters*, 99(6):062902, aug 2011. 81

[179] Chunlin Chen, Shuhui Lv, Junjie Li, Zhongchang Wang, Xiaobin Liang, Yanxi Li, Dwight Viehland, Ken Nakajima, and Yuichi Ikuhara. Two-dimensional electron gas at the Ti-diffused $BiFeO_3$ /$SrTiO_3$ interface. *Applied Physics Letters*, 107(3):031601, jul 2015. 81

[180] Y. Y. Mi, Z. Yu, S. J. Wang, P. C. Lim, Y. L. Foo, A. C. H. Huan, and C. K. Ong. Epitaxial $LaAlO_3$ thin film on silicon: Structure and electronic properties. *Applied Physics Letters*, 90(18):181925, apr 2007. 81

[181] Seung Gu Lim, Stas Kriventsov, Thomas N. Jackson, J. H. Haeni, D. G. Schlom, A. M. Balbashov, R. Uecker, P. Reiche, J. L. Freeouf, and G. Lucovsky. Dielectric functions and

optical bandgaps of high- K dielectrics for metal-oxide-semiconductor field-effect transistors by far ultraviolet spectroscopic ellipsometry. *Journal of Applied Physics*, 91(7):4500–4505, apr 2002.

[182] Z.Q. Liu, W.K. Chim, S.Y. Chiam, J.S. Pan, and C.M. Ng. Band gap, band offsets and dielectric constant improvement by addition of yttrium into lanthanum aluminate. *Thin Solid Films*, 534:177–182, may 2013.

[183] Xu-bing Lu, Zhi-guo Liu, Yi-ping Wang, Ying Yang, Xiao-ping Wang, Hong-wei Zhou, and Bich-yen Nguyen. Structure and dielectric properties of amorphous $LaAlO_3$ and $LaAlO_xN_y$ films as alternative gate dielectric materials. *Journal of Applied Physics*, 94(2):1229–1234, jul 2003.

[184] E. Cicerrella, J. L. Freeouf, L. F. Edge, D. G. Schlom, T. Heeg, J. Schubert, and S. A. Chambers. Optical properties of La-based high-K dielectric films. *Journal of Vacuum Science & Technology A: Vacuum, Surfaces, and Films*, 23(6):1676–1680, nov 2005. 81

[185] H Béa, B Dupé, S Fusil, R Mattana, E Jacquet, B Warot-Fonrose, F Wilhelm, A Rogalev, S Petit, V Cros, A Anane, F Petroff, K Bouzehouane, G Geneste, B Dkhil, S Lisenkov, I Ponomareva, L Bellaiche, M Bibes, and A Barthélémy. Evidence for Room-Temperature Multiferroicity in a Compound with a Giant Axial Ratio. *Physical Review Letters*, 102(21):217603, may 2009. 81

[186] Weigang Chen, Wei Ren, Lu You, Yurong Yang, Zuhuang Chen, Yajun Qi, Xi Zou, Junling Wang, Thirumany Sritharan, Ping Yang, L. Bellaiche, and Lang Chen. Domain structure and in-plane switching in a highly strained $Bi_{0.9}Sm_{0.1}FeO_3$ film. *Applied Physics Letters*, 99(22):222904, nov 2011.

[187] Zuhuang Chen, Zhenlin Luo, Chuanwei Huang, Yajun Qi, Ping Yang, Lu You, Chuansheng Hu, Tom Wu, Junling Wang, Chen Gao, Thirumany Sritharan, and Lang Chen. Low-Symmetry Monoclinic Phases and Polarization Rotation Path Mediated by Epitaxial Strain in Multiferroic $BiFeO_3$ Thin Films. *Advanced Functional Materials*, 21(1):133–138, jan 2011.

[188] H M Christen, J H Nam, H S Kim, A J Hatt, and N A Spaldin. Stress-induced R-MA-MC-T symmetry changes in $BiFeO_3$ films. *Physical Review B*, 83(14):144107, apr 2011.

[189] Q. He, Y. H. Chu, J. T. Heron, S. Y. Yang, W. I. Liang, C.Y. Kuo, H. J. Lin, P. Yu, C. W. Liang, R. J. Zeches, W. C. Kuo, J. Y. Juang, C. T. Chen, E. Arenholz, A. Scholl, and R. Ramesh. Electrically controllable spontaneous magnetism in nanoscale mixed phase multiferroics. *Nature Communications*, 2(1):225, sep 2011.

[190] M N Iliev, M V Abrashev, D Mazumdar, V Shelke, and A Gupta. Polarized Raman spectroscopy of nearly tetragonal $BiFeO_3$ thin films. *Physical Review B*, 82(1):014107, jul 2010.

[191] Yoshitaka Nakamura, Masanori Kawai, Masaki Azuma, Makoto Kubota, Mikio Shimada, Toshiaki Aiba, and Yuichi Shimakawa. Enhanced Piezoelectric Constant of (1- x)$BiFeO_3$x$BiCoO_3$ Thin Films Grown on $LaAlO_3$ Substrate. *Japanese Journal of Applied Physics*, 50(3R):031505, mar 2011.

[192] R J Zeches, M D Rossell, J X Zhang, A J Hatt, Q He, C.-H. Yang, A Kumar, C H Wang, A Melville, C Adamo, G Sheng, Y.-H. Chu, J F Ihlefeld, R Erni, C Ederer, V Gopalan,

L Q Chen, D. G. Schlom, N A Spaldin, L W Martin, and R Ramesh. A Strain-Driven Morphotropic Phase Boundary in $BiFeO_3$. *Science*, 326(5955):977–980, nov 2009. 81

[193] Akash Bhatnagar, Young Heon Kim, Dietrich Hesse, and Marin Alexe. Persistent Photoconductivity in Strained Epitaxial $BiFeO_3$ Thin Films. *Nano Letters*, 14(9):5224–5228, sep 2014. 81

[194] Anoop R. Damodaran, Chen-Wei Liang, Qing He, Chun-Yen Peng, Li Chang, Ying-Hao Chu, and Lane W. Martin. Nanoscale Structure and Mechanism for Enhanced Electromechanical Response of Highly Strained $BiFeO_3$ Thin Films. *Advanced Materials*, 23(28):3170–3175, jul 2011. 81

[195] Daniel Sando, Thomas Young, Ralph Bulanadi, Xuan Cheng, Yanyu Zhou, Matthew Weyland, Paul Munroe, and Valanoor Nagarajan. Designer defect stabilization of the super tetragonal phase in >70-nm-thick $BiFeO_3$ films on $LaAlO_3$ substrates. *Japanese Journal of Applied Physics*, 57(9):0902B2, sep 2018. 81

[196] M Dawber, K M Rabe, and J F Scott. Physics of thin-film ferroelectric oxides. *Reviews of Modern Physics*, 77(4):1083–1130, oct 2005. 82

[197] I Sosnowska, T P Neumaier, and E Steichele. Spiral magnetic ordering in bismuth ferrite. *Journal of Physics C: Solid State Physics*, 15(23):4835–4846, aug 1982. 83

[198] Jimmy Xuan Shen, André Schleife, Anderson Janotti, and Chris G. Van De Walle. Effects of la 5d and 4f states on the electronic and optical properties of $LaAlO_3$. *Physical Review B*, 94(20):205203, nov 2016. 85, 99, 101

[199] Peter E. Blöchl, O. Jepsen, and O. K. Andersen. Improved tetrahedron method for Brillouin-zone integrations. *Physical Review B*, 49(23):16223–16233, jun 1994. 85

[200] A. T. Zayak, X. Huang, J. B. Neaton, and Karin M. Rabe. Structural, electronic, and magnetic properties of $SrRuO_3$ under epitaxial strain. *Physical Review B*, 74(9):094104, sep 2006. 86, 87

[201] N C Bristowe, Emilio Artacho, and P B Littlewood. Oxide superlattices with alternating p and n interfaces. *Physical Review B*, 80(4):045425, jul 2009. 88, 92

[202] Yoyo Hinuma, Giovanni Pizzi, Yu Kumagai, Fumiyasu Oba, and Isao Tanaka. Band structure diagram paths based on crystallography. *Computational Materials Science*, 128:140–184, feb 2017. 89

[203] Yi Zhang, Lin Xie, Jeongwoo Kim, Alex Stern, Hui Wang, Kui Zhang, Xingxu Yan, Linze Li, Henry Liu, Gejian Zhao, Hang Chi, Chaitanya Gadre, Qiyin Lin, Yichun Zhou, Ctirad Uher, Tingyong Chen, Ying Hao Chu, Jing Xia, Ruqian Wu, and Xiaoqing Pan. Discovery of a magnetic conductive interface in $PbZr_{0.2}Ti_{0.8}O_3/SrTiO_3$ heterostructures. *Nature Communications*, 9(1):685, dec 2018. 92

[204] Massimiliano Stengel, Pablo Aguado-Puente, Nicola A Spaldin, and Javier Junquera. Band alignment at metal/ferroelectric interfaces: Insights and artifacts from first principles. *Physical Review B*, 83(23):235112, jun 2011. 93

[205] Charles Kittel. Theory of the structure of ferromagnetic domains in films and small particles. *Physical Review*, 70(11-12):965–971, dec 1946. 94

[206] S Prosandeev, S Lisenkov, and L Bellaiche. Kittel law in $BiFeO_3$ ultrathin films: A first-principles-based study. *Physical Review Letters*, 105(14):147603, sep 2010. 94, 95

[207] Francis Birch. Finite elastic strain of cubic crystals. *Physical Review*, 71(11):809–824, jun 1947. 99

[208] Xin Luo and Biao Wang. First-principles study of the electronic and optical properties in rhombohedral $LaAlO_3$. *Journal of Applied Physics*, 104(5):053503, sep 2008. 101

[209] Fedwa El-Mellouhi, Edward N. Brothers, Melissa J. Lucero, Ireneusz W. Bulik, and Gustavo E. Scuseria. Structural phase transitions of the metal oxide perovskites $SrTiO_3$, $LaAlO_3$, and $LaTiO_3$ studied with a screened hybrid functional. *Physical Review B*, 87(3):035107, jan 2013. 101

[210] S. A. Hayward, F. D. Morrison, S. A.T. Redfern, E. K.H. Salje, J. F. Scott, K. S. Knight, S. Tarantino, A. M. Glazer, V. Shuvaeva, P. Daniel, M. Zhang, and M. A. Carpenter. Transformation processes in $LaAlO_3$: Neutron diffraction, dielectric, thermal, optical, and Raman studies. *Physical Review B*, 72(5):054110, aug 2005. 101

[211] Shyue Ping Ong, William Davidson Richards, Anubhav Jain, Geoffroy Hautier, Michael Kocher, Shreyas Cholia, Dan Gunter, Vincent L. Chevrier, Kristin A. Persson, and Gerbrand Ceder. Python Materials Genomics (pymatgen): A robust, open-source python library for materials analysis. *Computational Materials Science*, 68:314–319, feb 2013. 101